

An Improved Particle Method For Simulations of Slamming With Fluid-structure Interaction

by

© *Ruosi Zha*

A thesis submitted to the
School of Graduate Studies
in partial fulfilment of the
requirements for the degree of
Doctor of Philosophy

Faculty of Engineering and Applied Science
Memorial University of Newfoundland

January 2021

St. John's

Newfoundland

Abstract

It is important to study the wave impact and slamming problems, involving breaking free surface, which can cause high impact pressure and therefore structural damage on ship hulls and offshore platforms.

An improved higher-order moving particle semi-implicit (MPS) method was developed to solve 2-D water entry problems. To overcome the inconsistency in the original MPS methods, a pressure gradient model was modified to guarantee the first-order consistency and to satisfy the conservation of momentum simultaneously. A particle shifting technique was also applied to improve the numerical stability. Validation studies were carried out for water entry of a rigid wedge with a deadrise angle of 30° and the tilt angles of 0° , 10° and 20° and two rigid ship sections. Convergence studies were conducted on domain size, particle spacing and time step. A Particle Convergence Index (PCI) method was proposed to evaluate numerical uncertainties in solutions by the Lagrangian particle-based methods. Uncertainties of the numerical solutions due to spatial discretization were calculated. The predicted impact pressures and forces by the present method are in good agreement with experimental data and other published numerical results.

The improved higher-order MPS method has also been applied to study fluid-structure interactions (FSI) for an elastic wedge entering calm water. The structural responses of the wedge with a reinforce tip were computed during the water entry. In the present method, different particle spacings and time steps were used for the fluid and the structure. Convergence of solutions on the particle spacings for the fluid and the structure and time step were investigated. Uncertainties of the numerical solutions

due to spatial discretization of both the fluid and the structure were evaluated based on the proposed PCI method. Validation studies were carried out to two wedges with deadrise angles of 20° and 30° entering water at various velocities. Numerical solutions were compared with the results based on the original higher-order MPS model and the experimental data. The present improved higher-order MPS method led to better agreement with experimental data than the original one, and significantly reduced the oscillations in numerical solutions.

General Summary

The present research is motivated by solving the wave impact and slamming problems that are closely relevant to ocean and naval architectural engineering. Structures can be deformed and even damaged due to the high impulsive pressures. The structural safety matters for the design and construction of both ship and offshore platforms.

Despite the experimental and theoretical studies, computational fluid dynamics (CFD) have been developed over years, among which particle-based methods have advantages for solving the highly non-linear problems including highly deformed interfaces. In the present work, the predictions of slamming loads with fluid-structure interactions were numerically studied with the development of an improved higher-order moving particle semi-implicit (MPS) method. The developed model demonstrated high stability and improved accuracy in predicting reasonable solutions including pressures and forces, as well as the structural responses. The coupling of the fluid and the structure was proved to be effective. Verification and validation studies were carried out through 2-D numerical simulations. Uncertainty analysis was proposed for the solutions by particle-based methods. The best-practice settings could be useful for the application of the methodology in the hydroelastic analysis and further study of the wave impact and slamming problems.

Acknowledgements

Firstly, I would like to express my sincere gratitude to my supervisor, Dr. Wei Qiu, for his academic and financial support throughout my Ph.D. studies and research. I truly appreciate his patience and kindness. Not only has his guidance consistently helped me throughout conducting my research, but also his continuous encouragement has helped me overcome the challenges I have met.

Besides my supervisor, I would like to thank the rest of my supervisory committee members, Dr. Heather Peng and Dr. David Molyneux, for their supervision and insightful comments. They have helped me to better understand the field of marine hydrodynamics. Without their precious support, it would not have been possible to conduct this research. I would also like to show my gratitude to my colleagues, Shanqin Jin, Dr. Peng Wen, Dr. Md. Ashim Ali, Dr. Wei Meng, Meng Chen, Saeed Barzegar Valikchali, Dr. Dexin Zhan and other faculty members and laboratory technicians at Memorial University, for the helpful discussions and assistance in all the stages of my research.

I am very grateful to the support by NSERC through its CREATE program. Without this support, I would have not been able to complete this research.

Last but not the least, I would like to thank my family. I would like to owe my deepest gratitude to my parents, Z. Zha and J. Xu. I would also like to express special appreciation to W. Chen. During my years of pursuing a Ph.D., they consistently support me and believe in me. I appreciate their love all the time.

Contents

Abstract	ii
General Summary	iv
Acknowledgements	v
List of Tables	ix
List of Figures	xi
1 Introduction	2
1.1 Background	2
1.2 Literature Review	3
1.2.1 Experimental Studies	3
1.2.2 Analytical Solutions	9
1.2.3 Numerical Simulations	11
1.3 Present Work	18
1.4 Outline of the Thesis	20
1.5 List of Published Papers	22

2	Methodology	23
2.1	Governing Equations	23
2.2	Particle Interaction Model	24
2.3	Gradient Model	26
2.4	Laplacian Model	29
2.5	Poisson Equations for Pressure	29
2.6	Particle Shifting	30
2.7	Structural Analysis	31
2.8	Boundary Conditions	32
2.9	Particle Spacings for Fluid and Structure	35
2.10	Searching Neighbouring Particles	36
2.11	FSI Coupling	38
2.12	Parallel Computing Scheme and Domain Decomposition	41
2.13	Uncertainty Analysis	42
3	Solving 2-D Dam Breaking	44
3.1	Convergence Studies	45
3.2	Numerical Results of Impact Pressure	51
3.3	Free Surface Elevation	52
4	Solving 2-D Vibration of a Thin Plate	57
5	Solving 2-D Slamming of Wedges and Ship Sections	63
5.1	2-D Wedge with Different Tilt Angles	64
5.1.1	2-D Wedge with Tilt Angle of $\theta = 0^\circ$	66

5.1.2	2-D Wedge with Tilt Angle of $\theta = 10^\circ$	76
5.1.3	2-D Wedge with Tilt Angle of $\theta = 20^\circ$	84
5.2	2-D Ship Sections	92
5.2.1	2-D Ship Section (Model A)	92
5.2.2	2-D Ship Section (Model B)	105
6	Solving 2-D Slamming of a Deformable Wedge with FSI	114
6.1	2-D Deformable Wedge with Deadrise Angle of $\alpha = 30^\circ$	115
6.2	2-D Deformable Wedge with Deadrise Angle of $\alpha = 20^\circ$	126
7	Conclusions and Future Work	136
7.1	Conclusions	136
7.2	Recommendations for Future Work	138
	Bibliography	140

List of Tables

3.1	Case matrix of convergence studies for 2-D dam breaking	46
3.2	Uncertainties in predicted peak pressure due to spatial resolution l_0 for 2-D dam breaking	47
3.3	Results of peak impact pressure for 2-D dam breaking	52
4.1	Comparison of the non-dimensional period and amplitude for the dis- placement of the plate free end	59
5.1	Case matrix of convergence studies for the 2-D wedge	67
5.2	Uncertainties in predicted peak pressures and force for the wedge with $\theta = 0^\circ$	69
5.3	Results for the 2-D wedge with $\theta = 0^\circ$	74
5.4	Uncertainties in predicted peak pressures and force for the wedge with $\theta = 10^\circ$	77
5.5	Results for the 2-D wedge with $\theta = 10^\circ$	78
5.6	Uncertainties in predicted peak pressures and force for the wedge with $\theta = 20^\circ$	85
5.7	Results for the 2-D wedge with $\theta = 20^\circ$	86

5.8	Case matrix of convergence studies for the ship sections	95
5.9	Uncertainties in predicted peak pressures and forces for the ship section (Model A)	100
5.10	The predicted pressures for the ship section (Model A)	103
5.11	The predicted forces for the ship section (Model A)	103
5.12	Uncertainties in predicted peak pressures and forces for the ship section (Model B)	109
5.13	The predicted pressures for the ship section (Model B)	112
5.14	The predicted forces for the ship section (Model B)	112
6.1	Summary of cases for the hydroelastic impact	116
6.2	Convergence studies on particle spacing and time step for the fluid ($\alpha = 30^\circ$ and $H = 0.39$ m)	116
6.3	Convergence studies on the number of particle layers across the thick- ness of the plate ($\alpha = 30^\circ$ and $H = 0.39$ m)	117
6.4	Uncertainties in maximum strain magnitude due to spatial resolution in terms of l_{f0} and l_{s0} for the elastic wedge ($\alpha = 30^\circ$ and $H = 0.39$ m)	120
6.5	Convergence studies on particle spacing and time step for the fluid ($\alpha = 20^\circ$ and $H = 0.5$ m)	124
6.6	Convergence studies on the number of particle layers across the thick- ness of the plate ($\alpha = 20^\circ$ and $H = 0.5$ m)	125
6.7	Uncertainties in the maximum strain magnitude due to spatial resolu- tion in terms of l_{f0} and l_{s0} for the elastic wedge ($\alpha = 20^\circ$ and $H = 0.5$ m)	128

List of Figures

2.1	Interaction region in 2-D simulations	25
2.2	Free surface identification and boundary conditions	34
2.3	Different particle spacings for the fluid and the structure	35
2.4	Searching neighbouring particles	37
2.5	The CSS coupling scheme for FSI computation	38
2.6	The flow chart for the proposed algorithm of MPS method	40
2.7	Parallel computing scheme and domain decomposition	41
3.1	Computational domain for 2-D dam breaking	45
3.2	Spatial convergence of impact pressure for 2-D dam breaking	48
3.3	Temporal convergence of impact pressure for 2-D dam breaking	48
3.4	Spatial convergence of water level elevations for 2-D dam breaking	49
3.5	Temporal convergence of water level elevations for 2-D dam breaking	50
3.6	Comparison of impact pressure at the point P(1.61,0.003) for 2-D dam breaking	51
3.7	Comparison of water level elevations for 2-D dam breaking	54
3.8	Comparison of pressure fields and free surface for 2-D dam breaking	55

3.9	Pressure fields and free surface for 2-D dam breaking	56
4.1	Set-up of 2-D vibration of a thin plate	57
4.2	Spatial convergence of displacement at the plate's free end	60
4.3	Temporal convergence of displacement at the plate's free end	60
4.4	Comparison of the displacement at the plate's free end	61
4.5	Strain contours of the elastic plate at four time instants	62
5.1	Sensors on the wedge surface	64
5.2	Computational domain for water entry of the wedge	65
5.3	Drop velocities for the wedge with different tilt angles	65
5.4	Sensitivity of pressures and force to domain size for the wedge with $\theta = 0^\circ$	70
5.5	Spatial convergence of pressures and force for the wedge with $\theta = 0^\circ$.	71
5.6	Temporal convergence of pressures and force for the wedge with $\theta = 0^\circ$	72
5.7	Comparison of pressures and force for the wedge with $\theta = 0^\circ$	73
5.8	Comparison of pressure fields for the wedge with $\theta = 0^\circ$	75
5.9	Sensitivity of pressures and force to domain size for the wedge with $\theta = 10^\circ$	79
5.10	Spatial convergence of pressures and force for the wedge with $\theta = 10^\circ$	80
5.11	Temporal convergence of pressures and force for the wedge with $\theta = 10^\circ$	81
5.12	Comparison of pressures and force for the wedge with $\theta = 10^\circ$	82
5.13	Comparison of pressure fields for the wedge with $\theta = 10^\circ$	83
5.14	Sensitivity of pressures and force to domain size for the wedge with $\theta = 20^\circ$	87

5.15	Spatial convergence of pressures and force for the wedge with $\theta = 20^\circ$	88
5.16	Temporal convergence of pressures and force for the wedge with $\theta = 20^\circ$	89
5.17	Comparison of pressures and force for the wedge with $\theta = 20^\circ$	90
5.18	Comparison of pressure fields for the wedge with $\theta = 20^\circ$	91
5.19	Sensors on the ship sections	92
5.20	Computational domains for the water entry of the ship sections	93
5.21	Drop velocities for the water entry of the ship sections	94
5.22	Sensitivities of pressures to domain size for the ship section (Model A)	97
5.23	Sensitivities of forces to domain size for the ship section (Model A)	98
5.24	Spatial convergence of pressures and forces for the ship section (Model A)	99
5.25	Temporal convergence of pressures and forces for the ship section (Model A)	101
5.26	Comparison of pressures and forces for the ship section (Model A)	102
5.27	Comparison of pressure fields for the ship section (Model A)	104
5.28	Spatial convergence of pressures and forces for the ship section (Model B)	108
5.29	Temporal convergence of pressures and forces for the ship section (Model B)	110
5.30	Comparison of pressures and forces for the ship section (Model B)	111
5.31	Comparison of pressure fields for the ship section (Model B)	113
6.1	Computational domain for the hydroelastic impact	115

6.2	Convergence of local strains to particle spacing ($\alpha = 30^\circ$ and $H = 0.39$ m)	118
6.3	Convergence of local strains to time step ($\alpha = 30^\circ$ and $H = 0.39$ m)	119
6.4	Convergence of local strains to the number of particle layers across the thickness of the plate ($\alpha = 30^\circ$ and $H = 0.39$ m)	119
6.5	Contours by the original higher-order gradient model ($\alpha = 30^\circ$ and $H = 0.39$ m)	122
6.6	Contours by the present higher-order gradient model in symmetrical form ($\alpha = 30^\circ$ and $H = 0.39$ m)	123
6.7	Comparison of local strains ($\alpha = 30^\circ$ and $H = 0.39$ m)	123
6.8	Comparison of local strains ($\alpha = 30^\circ$ and $H = 0.5$ m)	124
6.9	Convergence of local strains to particle spacing ($\alpha = 20^\circ$ and $H = 0.5$ m)	125
6.10	Convergence of local strains to time step ($\alpha = 20^\circ$ and $H = 0.5$ m)	126
6.11	Convergence of local strains to the number of particle layers across the thickness of the plate ($\alpha = 20^\circ$ and $H = 0.5$ m)	126
6.12	Comparison of local strains ($\alpha = 20^\circ$ and $H = 0.5$ m)	129
6.13	Numerical results of local strains for different deadrise angles and drop heights	129
6.14	Contours of fluid pressure and strain of the elastic panel at $t = 0.1$ s ($\alpha = 30^\circ$ and $H = 0.39$ m)	130
6.15	Contours of fluid pressure and strain of the elastic panel at $t = 0.15$ s ($\alpha = 30^\circ$ and $H = 0.39$ m)	131

6.16	Contours of fluid pressure and strain of the elastic panel at $t = 0.2$ s ($\alpha = 30^\circ$ and $H = 0.39$ m)	132
6.17	Contours of fluid pressure and strain of the elastic panel at $t = 0.1$ s ($\alpha = 30^\circ$ and $H = 0.5$ m)	132
6.18	Contours of fluid pressure and strain of the elastic panel at $t = 0.15$ s ($\alpha = 30^\circ$ and $H = 0.5$ m)	133
6.19	Contours of fluid pressure and strain of the elastic panel at $t = 0.2$ s ($\alpha = 30^\circ$ and $H = 0.5$ m)	133
6.20	Contours of fluid pressure and strain of the elastic panel at $t = 0.1$ s ($\alpha = 20^\circ$ and $H = 0.5$ m)	134
6.21	Contours of fluid pressure and strain of the elastic panel at $t = 0.15$ s ($\alpha = 20^\circ$ and $H = 0.5$ m)	134
6.22	Contours of fluid pressure and strain of the elastic panel at $t = 0.2$ s ($\alpha = 20^\circ$ and $H = 0.5$ m)	135

Chapter 1

Introduction

1.1 Background

Slamming is a physical phenomenon characterized by high impulsive pressures/loads of relative short-time durations on a body. Complicated physical effects are involved. For example, the free surface could be highly deformed or breaking during the impact. Air entrapment, air cushion and cavitation bubbles can be formed between the water surface and the body. The compressibility of the water also influences the interactions of air and water flow [1].

Slamming problems for ships and ocean structures are introduced as follows. Slamming on ships can be categorized as bottom, bow-flare, bow-stem and wet-deck slamming [2]. For example, bottom slamming could happen for ships suddenly plunged into the water [3]. A ship sailing in rough seas can be subjected to bow slamming [4] due to large-amplitude ship motions and wave impact on ship hull, i.e., green water on deck [5]. Wet-deck slamming may occur at the underside of inter-hull struc-

tures of multi-hull ships in waves [6]. Wave impacts can lead to transient ship hull girder vibration called slamming-induced whipping [7]. Another example of slamming is launching lifeboats or torpedoes into water [8]. Offshore structures operating in harsh environments could also be exposed to plunging breaking waves with violent impact, which leads to slamming forces [9]. Accidents happened if slamming loads on structures were underestimated. As reported by Attfield (1975) [10], wave slamming caused the failure of structural members in the splash zone of the British Petroleum's West Sole offshore platform in the southern North Sea.

Slamming can cause local structural deformation and damages. It is important to solve the highly-nonlinear water entry problem involving free surface breaking and the problem of fluid-structure interactions (FSI) for ships under impulsive loads due to slamming. The hydroelastic effects under certain conditions must be examined to accurately predict the impact pressures/loads and the structural responses [1]. For example, when the angle between the water surface and body surface is small, significant local dynamic hydroelastic effects can be observed [11]. An overview of studies on impact pressures/loads and structural responses using experiments, analytical solutions, and numerical simulations is given in the next section.

1.2 Literature Review

1.2.1 Experimental Studies

Experimental studies on slamming-induced pressures/loads and physical mechanisms relevant to slamming have been conducted over years.

One of the typical slamming problems is the water entry of a flat plate. Chuang (1966) [3] performed several dropping tests with free-falling flat bottom panels impact the free surface of the water at the David Taylor Model Basin. A linear relationship between the maximum pressure and the impact speed was found. The effect of the trapped air between the falling body and the water was analyzed on the measured maximum impact pressure.

The phenomena occurring during the impact of a flat plate on a water surface were investigated by Verhagen (1967) [12] both theoretically and experimentally. The compression of the trapped air cushion was mathematically modelled. The results showed that the influence of the compressible air layer caught between the falling plate and the water surface should be properly considered.

In terms of the data acquisition system in experimental studies, which is important for the uncertainty analysis and the reliability of the experimental data, Lin and Shieh (1997) [13] utilized a high-speed charge coupled device (CCD) camera and a digital particle tracking velocimeter (DPTV) to simultaneously measure the pressure and flow field during the water entry of a flat-bottom body and a cylinder.

Okada and Sumi (2000) [14] carried out precise pressure and strain measurements by dropping a plate with the different deadrise angles from 0° to 4° . Different impact patterns were studied during the impact process. It was observed that the Wagner-type pressure pattern was initially occurred near the keel, followed by the trapped-air pressure pattern toward the edge of the plate. It was also indicated that the maximum strain measured in the plate was not sensitive to the impact angle in the range studied. The structural response can be estimated by using the average pressure at impact.

Experiments on sandwich panel structures subjected to water slamming have been

also carried out in the work of Battley et al. (2005) [15]. The impact pressure and panel displacement during the impact were measured and structural responses of the panel were predicted by using the modal transient finite element analysis.

Huarte et al. (2011) [16] carried out a series of experiments on flat panels at different entry velocities up to 5 m/s and for deadrise angles in the range from 0.3° to 25° . The trapped air between the plate and the free surface was observed at high impact speeds and small deadrise angles. It was concluded that the effects of trapped air and air cushions are significant for the flat plate impacts with angles less than 5 degrees.

To study the ship bow slamming, numerous drop tests have been performed on wedge sections and bow-flare sections entering the water. For example, Bisplinghoff and Doherty (1952) [17] carried out a series of experiments for free-fall V-shaped wedges with different deadrise angles. The shape of the free surface of piled-up water was recorded by means of a high-speed motion-picture camera. Accelerations during drop tests were measured by a strain-gage type accelerometer.

Greenhow and Lin (1983) [18] conducted water entry experiments of wedges with large deadrise angles, i.e., over 25 degrees. They also studied the high speed entry of a cylinder into calm water and then exiting the water. It was observed that the free surface was breaking and the vortices shed by the cylinder interacted with the free surface and likely caused a pressure inversion across the free surface.

Troesch and Kang (1986) [19] also studied experimentally the water entry of a sphere at both vertical and oblique impact angles and a cusped body with only vertical motion. The experimental data of impact loads was applied to a validation of the results by using the three-dimensional theoretical solutions.

Tveitnes et al. (2008) [20] firstly investigated the water entry of a wedge section at a constant velocity, with deadrise angles from 5° to 45° , at a constant entry speed. In these experiments, the hydrodynamic forces on the body during impacts can be directly measured at velocities of higher than 1 m/s, using the axial force load cells. The changes in added mass after chine wetting were quantified, which was important for planing craft predictions.

Maneuvering of vehicles or ship motions in waves can cause asymmetric water entry. Judge et al. (2004) [21] performed systematic experimental tests on the asymmetric-oblique water entry of a wedge. Both horizontal and vertical impact velocities were taken into account. The initial separation-ventilation of the flow from the apex due to asymmetric impact was visualized in their work.

Wedges with different tilt angles were also tested by Barjasteh et al. (2016) [22]. Parameters including initial deadrise angle, inclination angle and impact speed were investigated. The comparison of results by asymmetric and symmetric tests showed that even a small inclination angle can significantly increase the pressure at the side with a smaller deadrise angle.

Zhao et al. (1996) [23] carried out drop tests of a wedge section with 30° deadrise angle and a typical ship bow section at constant vertical velocity at Norwegian Marine Technology Research Institute (MARINTEK). The effects of flow separation and jet flows at the intersection between the body surface and the free surface were detailed. Comparison between the theoretical solutions and the experimental data was given.

Hermundstad and Moan (2005) [24] conducted model tests of a 120 m Ro-Ro vessel in regular head and oblique waves. Two slamming panels in the bow flare at station 9.5 on the port side were installed to obtain the average slamming pressure

on the panel. It was observed that slamming pressures in a flared area were sensitive to small variations in the roll angle. In their tests, the effect of the forward speed of the ship was also analyzed, which led to a pile-up of water around the bow. It was concluded that the pile-up of water significantly increased the impact pressure on the panels in the upper part of the flare, particularly for the lower waves. The slamming loads can induce a large sagging moment in the hull girder with subsequent vibrations.

A series of model tests, i.e., Wave Induced Loads on Ships Joint Industry Project (WILS JIP-I, II and III, 2006-2014), was conducted by Korea Research Institute of Ships & Ocean engineering (KRISO). An extensive experimental database on slamming, springing and whipping was provided. As a focused session of ISOPE-2016, Rhodes by the International Hydrodynamic Committee (IHC) of the International Society of Offshore and Polar Engineers (ISOPE), a comparative study [25] on water impact problem for ship sections and wedges entering the water was carried out. The experimental data can be found in the work of Hong et al. (2017) [26].

Kim et al. (2017) [27] investigated the characteristics of the pressure sensor for the measurement of the water impact load. The measured peak pressures, rise times, and pressure impulses were compared by couples of different pressure sensors, involving different types, sensing areas, and sensitivities.

In the project of WILS JIP-III, Hong et al. (2014) [28] studied the bow-flare slamming loads on a 10,000TEU containership. The containership model was made up of six segments connected by a U-shape steel backbone. The temporal and spatial distribution of slamming load during tests were recorded using a number of force and pressure sensors. The stern slamming loads on the same containership was also

studied by Kim et al. (2015) [29] by towing a ship model in regular and irregular waves. Head and following sea conditions with various ship speeds were involved. The characteristics of the bow-flare slamming and the stern slamming were presented in their work.

To further address the hydroelastic slamming problems, a series of experiments on deformable wedges freely falling into water considering different structural stiffness, deadrise angles, impact velocities and masses of wedges were conducted by Panciroli et al. (2012) [30]. High hydroelastic effects can be observed at high impact speed as the body was made by composite lightweight structures. The hydroelasticity was found to be critical if the ratio (R) between the wetting time and the natural period of the structure was small, e.g., lower than 1. Two novel fluid-structure interaction phenomena were found in the water entry tests of deformable wedges by Panciroli (2013) [31], including the repetition of impacts and separation between the fluid and the structure in the region of jet flow during slamming, and a tendency to cavitation in the underwater fluid-structure interface.

Luo et al. (2012) [32] performed an experimental study of slamming load and elastic response of a free-drop steel wedge made up of 9 longitudinal stiffeners and 5 transverse frames. The acceleration, slamming pressures, and stress responses were measured. Some high-frequency oscillations (around 100) of the stress responses on the longitudinal stiffeners due to the hydroelastic impact.

Stenius et al. (2013) [33] studied the significance of hydroelasticity for slamming loaded marine panels. The impact pressures for both rigid panels and the flexible panel were compared with varying impact velocities. Substantial kinematic hydroelastic effects were indicated for the strains in the upper panel edge.

Recently, the technique of particle image velocimetry (PIV) has been adopted in the tests of water entry. For example, Shams et al. (2015) [34] applied PIV to characterize the water entry of an asymmetric wedge with varying heel angles falling into a quiescent fluid. The pressure field in the fluid can be reconstructed from PIV data by integrating the Poisson equation. PIV was subsequently employed to measure the flow characteristics for the hydroelastic slamming of flexible wedges entering and exiting calm water by Shams et al. (2017) [35].

Russo et al. (2018) [36] also presented experimental dataset for the water entry of a wedge with 37° by using a PIV system and a complementary array of sensors including position sensors, accelerometers, and pressure sensors. Asymmetric and oblique impact were investigated for small deadrise angles. The results from PIV-based pressure reconstruction were validated by comparison to the traditional sensor-based data collected by pressure sensors.

Experiments continue to be important to predict the slamming loads, reveal the flow characteristics, and provide benchmark data for the validation of analytical solutions and numerical simulations. However, experimental studies are costly and limited to model scale.

1.2.2 Analytical Solutions

Analytical solutions for water entry problem were pioneered by von Kármán (1929) [37]. The motivation was to analyze the maximum impact pressures acting on sea-plane floats during landing, which can be treated approximately as a wedge-shaped body striking a horizontal surface of the water. An asymptotic theory was first de-

veloped to solve the flat impact problems with the linearized free surface and wall boundary conditions. The calculated force acting between the body and water was validated by experimental data.

The von Kármán's solution was improved by considering the effect of water splash on the body by Wagner (1932) [38]. Dobrovol'skaya (1969) [39] derived an analytic solution for the case of uniform symmetrical entry of a wedge into a half-plane of fluid at a constant velocity. As an extension of Wagner's theory, Oliver (2007) [40] developed the second-order Wagner's theory for solving water entry problems at small deadrise angles. The second-order corrections were made for the locations of the higher-pressure jet-root regions and the impact force on the body using a systematic matched-asymptotic analysis.

Howison et al. (1991) [41] also applied Wagner's theory and derived the analytic solution of water-entry problems for both two-dimensional and two-dimensional flows. The effects of jet separation and the air cushion between the body and the water were discussed.

Mei et al. (1999) [42] derived the analytic solution of the water impact problem based on Wagner's theory for general two-dimensional bodies entering initially calm water, including wedges of arbitrary deadrise angles, a circular cylinder and a bow-flare section. The results were not restricted to shallow body submergence or small body deadrise angles.

Despite the fact that three-dimensional slamming forces can be usually approximated using a series of 2-D sections, Scolan and Korobkin (2001) [43] presented the exact analytical solutions for three-dimensional water entry based on Wagner's theory by the inverse method.

Most of the analytical solutions were however limited to the assumption of shallow body submergence and simple geometries.

1.2.3 Numerical Simulations

In terms of numerical methods to solve water-entry problems, methods based on the potential-flow theory and the computational fluid dynamics (CFD) have been developed over years.

A numerical solution based on the boundary element method (BEM) was first proposed by Zhao and Faltinsen (1993) [44] for the water entry of a two-dimensional body of arbitrary cross-section. For wedges with deadrise angles varying from 4° to 81° , their numerical results of the slamming loads and pressure distributions on the body agreed with the similarity solution results. Issues existed when the deadrise angle was smaller than 4° . Zhao et al. (1996) [23] applied linearized free-surface boundary conditions and solved the problem numerically using a boundary integral equation method. The numerical results were in agreement with the experimental data. Recently, Wang and Faltinsen (2017) [45] further improved the BEM developed by Zhao and Faltinsen (1993) [44] and investigated the water entry of wedges with small deadrise angles. The results were obtained for deadrise angles down to 1° and compared to the asymptotic solutions.

Hermundstad and Moan (2005) [24] applied a nonlinear strip theory method with a generalized 2-D Wagner formulation solved by the BEM to obtain the slamming loads on a Ro-Ro vessel. The numerical results were validated by experimental results.

One of the difficulties in the BEM methods is due to the boundary conditions

on the intersection of the body surface and the free surface. To satisfy the two boundary conditions exactly and simultaneously, Chuang et al. (2006) [46] developed a boundary element method based on the desingularized Cauchy's formula to solve the two-dimensional water entry problems. The corner singularity at the intersection point of the body and the water surface was removed by a numerical approach. The results agreed well with the analytical solutions of Dobrovolskaya (1969) [39].

A simplified method based on the Wagner theory and the boundary element method was proposed by Tassin et al. (2012) [47] to predict impact loads acting on three-dimensional bodies during water entry. The hydrodynamic pressure acting on the body surface was calculated using the modified Logvinovich model (MLM). Experimental impact tests and CFD simulations were also carried out for validation. Three specimens involving an elliptic paraboloid, a wedge with conical ends and a square pyramid were studied. The proposed numerical method was found to be able to accurately predict slamming forces.

Since the potential-flow based methods have difficulties in dealing with highly deformed or breaking free surface, many CFD methods have been developed to address highly nonlinear problems, including mesh-based, particle-based and hybrid approaches. Among mesh-based CFD methods, the level-set (LS) method [48], the volume of fluid (VOF) [49] and the constrained interpolation profile (CIP) [50] methods have been employed to capture highly nonlinear free surfaces and to solve slamming problems.

In the work of Kleefsman et al. (2005) [51], dam breaking and water entry problems were studied by the numerical method based on the Navier-Stokes equations. The free surface was captured using the VOF method together with a local height function with

strict mass conservation. Schellin and El Moctar (2007) [52] studied the slamming loads with a Reynolds-averaged Navier Stokes (RANS) solver, in which the interfaces were captured by the VOF method.

Yang and Qiu (2012) [53] employed the CIP method to solve both 2-D and 3-D slamming problems. The free surface and the body boundaries were captured using density functions. For wedges with small deadrise angles, the compressibility of air was studied. Wen and Qiu (2016) [54] further developed the CIP method by implementing a parallel computing scheme to solve 2-D slamming problems. A high-order upwind scheme was employed to capture the advection of a profile. In the work of Wen and Qiu (2018) [55], the advection of the water phase was solved by applying the THINC/WLIC scheme, i.e., tangent of hyperbola for interface capturing with weighted line interface calculation. Typical slamming problems involving the water entry of a 3-D wedge with prescribed velocities, the free-fall water entry of a modified Wigley hull and an inclined circular cylinder were studied.

The dynamic overset grid technique [56] has been developed for efficiently simulating the large-amplitude body motions. For example, Shen et al. (2016) [57] applied a dynamic overset method to predict large-amplitude ship motions and slamming loads and used the VOF method to capture the free surface. The slamming loads on a 10K TEU container ship model at different speeds operating in wave conditions were numerically investigated and compared to the experimental data.

Considering the structural responses during the slamming, Piro and Maki (2013) [58] developed a coupled solver using the finite volume method (FVM) for the fluid analysis and the finite element method (FEM) for the structural analysis. The water entry and the water exit of both rigid and flexible wedges were investigated.

Despite the success with traditional mesh-based CFD methods, it is still challenging to simulate violent flow involving breaking free surfaces and moving boundaries due to the numerical diffusion and topological failures. The Lagrangian particle-based methods, which benefit from their mesh-free characteristics, have advantages in treating highly deformed interfaces and moving boundaries. Among the mesh-free methods, the smoothed particle hydrodynamics (SPH) method [59] and the moving particle semi-implicit (MPS) method [60] have been used to solve water entry problems. For example, Farsi and Ghadimi (2015) [61] studied both symmetric and asymmetric water entries of wedges with a wide range of deadrise angles using a weakly compressible SPH (WCSPH) method. To address the issue of high-frequency pressure oscillations in the conventional SPH methods, various improvements have been made. Lee et al. (2008) [62] developed the incompressible SPH (ISPH) method to improve the pressure calculation for incompressible flows. Yokoyama et al. (2014) [63] investigated the splash induced by a spherical object using the MPS method. The interface particles between the falling object and the fluid surface were examined. A two-phase incompressible-compressible SPH method (ICSPH) was developed by Lind et al. (2015) [64] to predict the pressure on a horizontal plate impacting waves. Sun et al. (2016) [65] developed a coupled MPS-modal superposition method to study water entry of a flexible wedge and fluid-structure interactions. Nair and Tomar (2017) [66] applied the ISPH method to simulate the evolution of cavity during the water entry of cylinders in various shapes. The transfer of kinetic energy in different phases of the cavity formation was examined. Rao and Wan (2018) [67] developed the MPS-FEM coupled method which was applied to study the solitary wave impacting onto a horizontal plate. Comparison between the cases with elastic and the rigid plate

interacting with the solitary wave was given.

In the weakly compressible SPH methods, pressure can be solved using the equation of state. Different from the explicit method in SPH, the pressure is computed by the projection method with a semi-implicit process in the MPS method. A system of Poisson equations for pressure is formulated and greater accuracy in pressure computation can be obtained by using a relatively large time step. Progress has been made to deal with numerical issues in the original MPS method, which is only in first-order accuracy, such as nonphysical high-frequency pressure oscillations and numerical instabilities. For example, Akimoto (2013) [68] studied a 2-D wedge and a 3-D cylinder with a modified MPS method, in which improvement was made to treat smooth body boundaries. The pressure oscillations can be generally suppressed by using an improved identification of the free surface and a mixed source term in the Poisson equations for pressure [69].

It should be noted that among the Eulerian methods, the immersed boundary (IB) method has been widely used to solve the FSI problems on Cartesian grids. Moving body boundaries are determined by cutting Cartesian grid cells. Grid generation is therefore straightforward even for complex geometry. Non-boundary conforming grids are needed and no re-meshing is required for moving boundaries. As a result, less computer memory and CPU resources [70] are needed. An IB method has been developed to improve the sharpness of the moving fluid-structure interface [71]. However, it is required to refine the grid resolution in the vicinity of the boundaries. In comparison with the IB method, one of the advantages of the MPS method is that the fluid-structure interfaces can be defined and resolved with greater accuracy. As another advantage of the MPS method, the governing equations in Lagrangian form

free of convective terms. Numerical errors caused by solving the convective transport in Eulerian methods can be avoided [72].

Another mesh-based method to solve FSI is the arbitrary LagrangianEulerian (ALE) method, which was reviewed by Barone and Payne (2005) [73]. In the ALE method, the mesh inside the computational domains can move arbitrarily and therefore the quality of elements can be improved in comparison with the mesh deformation technique. The ALE method also has advantages in treating complex boundaries and interfaces of multi-physics fields and multi-materials since meshes can be body-fitted and move along with the deformation of boundaries and interfaces [74, 75]. The governing equations in the moving domains need to be mapped to a fixed computational domain, and then the transformed equations are solved. The mapping leads to issues on solving problems with large deformation, and re-meshing might be required in case of mesh distortion, which could impair computational efficiency and effectiveness. Compared to the ALE method, the governing equations in Lagrangian form can be solved directly by the MPS method without involving any mapping and re-meshing for highly deformed boundaries and free surface [76]. Since fluid and structure are both discretized into particles, the interpolations on interfaces are straightforward.

MPS methods have been employed with various degrees of improvement to solve water entry problems. For example, Akimoto (2013) [68] studied a 2-D wedge and a 3-D cylinder with a modified MPS method, in which improvement was made to treat smooth body boundaries. Yokoyama et al. (2014) [63] investigated the splash induced by a spherical object using the MPS method. The interface particles between the falling object and the fluid surface were examined. Sun et al. (2016) [65] developed a coupled MPS-modal superposition method to study water entry of a flexible wedge

and fluid-structure interactions.

In spite of the progress, the accumulated error due to the discretization of derivatives both in space and in time remains an issue in the first-order models. For example, the calculation of the time variation of the particle number density in the source term of the Poisson equations for pressure was only in first-order accuracy for the traditional MPS methods, which led to pressure fluctuations and therefore large numerical errors. To address this problem, a higher-order source term, called the CMPS-HS method, was developed by Khayyer and Gotoh (2011) [77]. In their work, the Poisson equations for pressure were derived based on the direct calculation of the time differentiation from the kernel function. Compared with the results by using the first-order source term, a considerable improvement was indicated in their 2-D simulations of wave impact.

Another issue in the first-order MPS methods is the inconsistency in pressure gradient. For particles which are disorderly distributed or near the boundary, the first-order model for the gradient is not satisfactory. Based on the Taylor series expansion, a higher-order gradient model, called MPS-HS-HL-ECS-GC, was proposed by Khayyer and Gotoh (2011) [77]. The accuracy can be in second-order when particles are distributed regularly and in first-order when particles are distributed irregularly in the interaction region. A review of various improvements in pressure computations was given by Gotoh and Khayyer (2016) [78].

1.3 Present Work

The present research focuses on the development of an improved MPS method to solve water entry problems with fluid-structure interaction. The main objectives and contributions of this thesis are summarized as follows:

- Improvement of MPS method. There are numerical issues in the original MPS method, which is only in first-order accuracy, such as nonphysical high-frequency pressure oscillations and numerical instabilities. For the first-order gradient models, the first-order consistency cannot be satisfied. To address this problem, a corrected pressure gradient model based on the Taylor series expansion was proposed by Khayyer and Gotoh [77]. However, the model does not satisfy the conservation of momentum, which leads to pressure oscillations. In this thesis, the improved model for pressure gradient in symmetrical form was developed [79, 80, 81]. Consequently, the first-order consistency for pressure gradient can be guaranteed and the conservation of momentum is satisfied. A combined scheme for the identification of the free surface particles was developed [82], where the non-symmetry criteria [83] was used for the fluid particles and the density criteria [60] was used for the wall particles separately. A particle shifting technique [84] was also applied to improve the numerical stability. It was found that some particles could continue to clump together leading to the onset of instability. [84]. The issue of particles with highly anisotropic distributions in violent flows can be avoided with the application of particle shifting. For example, a slamming simulation could crash within 2 ms without using the particle shifting. For the present method, it can be run more than 30 ms without

numerical instabilities.

- Solving FSI problems. Challenges remain in the prediction of the impact pressures/loads during slamming with fluid-structure interaction. The improved MPS method has been employed to solve the two-dimensional water entry problems. Validation studies were carried out for the free-fall water entry of rigid bodies, including a 2-D wedge with various tilt angles and two different ship sections [80]. The convergence of numerical solution to the size of computational domain, the particle spacing and the time step was investigated. The predicted impact pressures/loads were compared with the experimental data, the numerical results by the first-order gradient model in symmetrical form and those by the original higher-order gradient model. Further studies were carried out to elastic bodies with different deadrise angles entering the water at a couple of drop velocities [81]. Numerical solutions were compared with the results based on the original higher-order gradient model and the experimental data.
- Uncertainty analysis. Uncertainties in CFD solutions with mesh-based methods have been extensively studied. However, uncertainties in solutions with particle-based methods are relatively rare. For mesh-based methods, the spatial discretization errors can be evaluated by using the Grid Convergence Index (GCI) method [85]. A similar approach, i.e., the Particle Convergence Index (PCI) method, is proposed in this work to evaluate uncertainties with respect to the particle resolution in solutions with Lagrangian particle-based methods [80, 81]. In this method, the particle spacing represents the spatial resolution. Uncertainty levels in the present simulations were examined using the proposed

PCI method.

1.4 Outline of the Thesis

This thesis is organized into six chapters as follows.

In Chapter 1, the research background on slamming problems in marine applications is briefly described. A literature review on solving slamming problems by using experimental studies, analytical solutions and numerical approaches is detailed. The improvements of MPS methods are reviewed. The objectives and the scope of this research are also presented.

Chapter 2 presents the details of the research methodologies. The numerical methods are introduced and mathematical formulations of the improved higher-order MPS method are derived. Firstly the governing equations for the incompressible viscous flow and the elastic structure are given. The particle interaction method in the present MPS method is introduced, which is followed by the gradient model and Laplacian model. The Poisson equations for pressure are then derived and the boundary conditions are given. The particle shifting technique is also presented. In addition, the particle models for structural analysis are introduced. Different particle spacings are used ensuring accurate prediction of fluid and structural responses. The coupling scheme for fluid-structure interaction used in the present work is explained. The parallel computing scheme and domain decomposition are further discussed. Subsequently, the uncertainty analysis regarding the numerical solutions by Lagrangian particle methods is proposed.

Chapter 3 focuses on solving the two-dimensional dam breaking problems to pre-

liminarily validate the present method. The water impact pressures and free surface simulated by the present method were studied and compared to the experimental data.

Chapter 4 shows the numerical simulations of the vibration of a two-dimensional thin plate to verify the present structural model. Convergence studies on the particle spacing and time steps are conducted. The results showed improvement in comparison to the analytical solutions and the results by using other numerical methods.

In Chapter 5, the numerical methods are validated by simulating two-dimensional water entry problems including wedges with various tilt angles and ship sections with different drop heights. Convergence studies on domain sizes, particle spacing and time steps are detailed. Discussions on the solutions on the impact pressures and forces are presented.

The present method is then extended to the free-fall water entry of a two-dimensional deformable wedge with different deadrise angles and two dropping heights as presented in Chapter 6. The structural responses due to wave-structure interactions were predicted and analyzed. The improved higher-order MPS methods led to better agreement with experimental data than the original one, and significantly reduced the oscillations in numerical solutions.

In Chapter 7, this thesis ends with conclusions and a summary of future perspectives. The extension of the present two-dimensional method to three-dimensional method is commented.

1.5 List of Published Papers

- Zha, R., Peng, H., and Qiu, W. (2021). An improved higher-order moving particle semi-implicit method for simulations of two-dimensional hydroelastic slamming. *Physics of Fluids*, 33(3):037104.
- Zha, R., Peng, H., and Qiu, W. (2020). Solving 2-D slamming problems by an improved higher-order moving particle semi-implicit method. *Journal of Ship Research*, p. 129.
- Zha, R., Peng, H., and Qiu, W. (2019). Solving 2-D slamming problems by the higher-order MPS method with an improved pressure gradient model. In *Proceedings of 38th International Conference on Ocean, Offshore and Arctic Engineering*, p. V009T12A007, Glasgow, UK, June.
- Zha, R., Peng, H., and Qiu, W. (2018). Solving 2-D slamming problems by the MPS method with source term correction. In *Proceedings of 37th International Conference on Ocean, Offshore and Arctic Engineering*, p. V009T13A035, Madrid, Spain, June.
- Zha, R., Qiu, W., and Peng, H. (2017). Solving 2-D fluid-structure interaction problem by a coupled particle method. In *Proceedings of 36th International Conference on Ocean, Offshore and Arctic Engineering*, p. V07AT06A046, Trondheim, Norway, June.
- Zha, R., Qiu, W., and Peng, H. (2017). Solving 2-D coupled water entry problem by an improved MPS method. In *Proceedings of 32nd International Workshop on Water Waves and Floating Bodies*, p. 23-26, Dalian, China, April.

Chapter 2

Methodology

2.1 Governing Equations

For hydrodynamic analysis, the incompressible viscous flow is governed by the continuity equation and the momentum equation:

$$\nabla \cdot \mathbf{U}_f = 0 \quad (2.1)$$

$$\frac{D\mathbf{U}_f}{Dt} = -\frac{1}{\rho_f} \nabla p + \nu_f \nabla \cdot \nabla \mathbf{U}_f + \mathbf{g} + \frac{1}{\rho_f} \mathbf{F}_{s-f} \quad (2.2)$$

where ρ_f , \mathbf{U}_f , p , ν_f , \mathbf{g} and \mathbf{F}_{s-f} represent the density of fluid, fluid velocity, fluid pressure, viscosity of fluid, the gravitational acceleration, and the force on fluid due to structure, respectively. The subscripts s and f stand for the structure and fluid, respectively. Note that turbulence models are not considered in this thesis.

Governing equations for the isotropic linear elastic structure are given as:

$$\frac{D\mathbf{U}_s}{Dt} = \frac{1}{\rho_s} \nabla \cdot (\lambda_s \text{tr}(\varepsilon_{mn}) \delta_{mn} + 2\mu_s \varepsilon_{mn}) + \mathbf{g} + \frac{1}{\rho_s} \mathbf{F}_{f-s} \quad (2.3)$$

$$\frac{D}{Dt} (I_s \boldsymbol{\omega}_s) = \frac{D}{Dt} [\mathbf{r}_s \times (m_s \mathbf{U}_s)] \quad (2.4)$$

where \mathbf{U}_s is the structural velocity, ρ_s is the density of structure, ε_{mn} is the strain tensor, $m = 1, 2$, $n = 1, 2$ for 2-dimensional problems, δ_{mn} is the Kronecker's delta and λ_s and μ_s are the Lamé constants. Note that \mathbf{F}_{f-s} is the fluid force on structure. I_s is the moment of inertia of structure, m_s is the mass of structure, $\boldsymbol{\omega}_s$ is the angular velocity, and \mathbf{r}_s is the position vector of structure.

2.2 Particle Interaction Model

In the present method, the fluid and structure are discretized by fluid particles and structural particles, respectively. For the particle interaction model, a widely used kernel function in many first-order MPS methods [86] was written as:

$$w_{ij} = \begin{cases} \frac{r_e}{r_{ij}} - 1, & 0 < r_{ij} < r_e \\ 0, & r_{ij} \geq r_e \end{cases} \quad (2.5)$$

where r_e and r_{ij} denote radii of the interaction region and the distance between particle i and particle j , respectively. The interaction region for particle i is defined as a space in which particles can interact with particle i , as shown in Fig 2.1.

In comparison with the Gaussian kernels, the Wendland kernel performs better in the simulation of free surface viscous flow based on the work of Macia et al. (2011) [87]. In addition, a clustering of neighboring particles due to the onset of the tensile instability can be generally avoided by using the Wendland kernel. The C^2 Wendland kernel function [88] as follows was adopted in the present higher-order MPS method:

$$w_{ij} = \begin{cases} \left(1 - \frac{r_{ij}}{r_e}\right)^4 \left(1 + \frac{4r_{ij}}{r_e}\right), & 0 \leq r_{ij} < r_e \\ 0, & r_{ij} \geq r_e \end{cases} \quad (2.6)$$

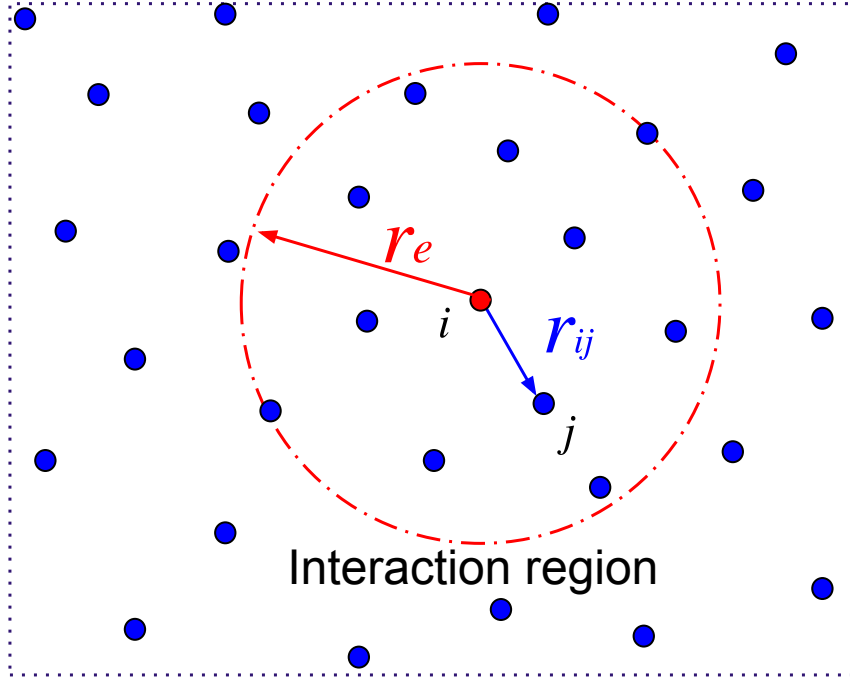


Figure 2.1: Interaction region in 2-D simulations

Class 2 (C^2) denotes the ratio of the radius of interaction region to particle spacing is 2, which is close to 2.1. Note that 2.1 is the value of the widely used kernel function in the original MPS method. Compared with the original kernel function in Eq. (2.5), smoother results without singularity can be obtained for the estimation of derivatives.

The first and second derivatives of the kernel function can be calculated by:

$$\frac{\partial w_{ij}}{\partial r} = \begin{cases} -\frac{20r_{ij}}{r_e^2} \left(1 - \frac{r_{ij}}{r_e}\right)^3, & 0 \leq r_{ij} < r_e \\ 0, & r_{ij} \geq r_e \end{cases} \quad (2.7)$$

$$\frac{\partial^2 w_{ij}}{\partial r^2} = \begin{cases} -\frac{20}{r_e^2} \left(1 - \frac{r_{ij}}{r_e}\right)^2 \left(1 - \frac{4r_{ij}}{r_e}\right), & 0 \leq r_{ij} < r_e \\ 0, & r_{ij} \geq r_e \end{cases} \quad (2.8)$$

It is assumed that all particles have the same mass. The density of fluid at the

location \mathbf{r}_i is proportional to the particle number density, n_i , which is defined as the sum of kernel functions of particles within the interaction region of a particle i :

$$n_i = \sum_{j \neq i} w_{ij} \quad (2.9)$$

2.3 Gradient Model

The gradient operator can be calculated as the weighted average gradient of all neighboring particles in the interaction region. Many studies have been carried out to improve the modelling of pressure gradient in the literature.

In the original MPS method [60], the pressure gradient was given by:

$$\langle \nabla p \rangle_i = \frac{d}{n^0} \sum_{j \neq i} \left[(p_j - p_i) \frac{\vec{r}_j - \vec{r}_i}{|\vec{r}_j - \vec{r}_i|^2} w_{ij} \right] \quad (2.10)$$

where $d = 2$ is the number of spatial dimensions, the normalization factor, n^0 , is the initial particle number density, p_i and p_j are pressures of particle i at \vec{r}_i and of the neighboring particle j at \vec{r}_j , respectively. n^0 is a simplified form of n_i^0 , which should be constant for uniformly distributed particles. Note that $\langle \rangle$ denotes the approximation of a variable in the interaction region of a particle. In this model, the conservation of momentum is not satisfied and pressure oscillations are therefore enlarged. This model also leads to numerical instabilities. Effort has been made to improve the pressure gradient model. One of improved models for the pressure gradient is the first-order gradient model in symmetrical form proposed by Lee et al. (2011) [89], which can be written as:

$$\langle \nabla p \rangle_i = \frac{d}{n^0} \sum_{j \neq i} \left[(p_j + p_i) \frac{\vec{r}_j - \vec{r}_i}{|\vec{r}_j - \vec{r}_i|^2} w_{ij} \right] \quad (2.11)$$

This method however does not satisfy the first-order consistency if particles are disorderly distributed or near the boundary [90]. To overcome this problem, a corrected pressure gradient model was proposed by Khayyer and Gotoh (2011) [77]. In their work, based on the Taylor series expansion, the pressure of a particle j can be written as:

$$p_j = p_i + \left(\frac{\partial p}{\partial x}\right)_i x_{ij} + \left(\frac{\partial p}{\partial y}\right)_i y_{ij} + O(r^2) \quad (2.12)$$

where x_{ij} and y_{ij} are the components of the position vector, \vec{r}_{ij} . Since the standard kernel function was used in the original higher-order MPS method, it was derived $\frac{-\partial w_{ij}}{\partial r_{ij}} = \frac{w_{ij}}{r_{ij}}$. The pressure gradient at particle i can be directly computed from:

$$\begin{aligned} \nabla p_i &= \int p_j \nabla w_{ij} d\vec{r} \\ &= \int p_j \left(\frac{w_{ij}}{r_{ij}} \frac{x_{ij}}{r_{ij}} dx + \frac{w_{ij}}{r_{ij}} \frac{y_{ij}}{r_{ij}} dy \right) \\ &= p_i \int \left(\frac{w_{ij}}{r_{ij}} \frac{x_{ij}}{r_{ij}} dx + \frac{w_{ij}}{r_{ij}} \frac{y_{ij}}{r_{ij}} dy \right) + \\ &\quad \left(\frac{\partial p}{\partial x}\right)_i \int \left(x_{ij} \frac{w_{ij}}{r_{ij}} \frac{x_{ij}}{r_{ij}} dx + x_{ij} \frac{w_{ij}}{r_{ij}} \frac{y_{ij}}{r_{ij}} dy \right) + \\ &\quad \left(\frac{\partial p}{\partial y}\right)_i \int \left(y_{ij} \frac{w_{ij}}{r_{ij}} \frac{x_{ij}}{r_{ij}} dx + y_{ij} \frac{w_{ij}}{r_{ij}} \frac{y_{ij}}{r_{ij}} dy \right) + O(r^2) \end{aligned} \quad (2.13)$$

where

$$\begin{aligned} \int x_{ij} \frac{w_{ij}}{r_{ij}} \frac{x_{ij}}{r_{ij}} dx &= 1 \\ \int x_{ij} \frac{w_{ij}}{r_{ij}} \frac{y_{ij}}{r_{ij}} dy &= 0 \\ \int y_{ij} \frac{w_{ij}}{r_{ij}} \frac{x_{ij}}{r_{ij}} dx &= 0 \\ \int y_{ij} \frac{w_{ij}}{r_{ij}} \frac{y_{ij}}{r_{ij}} dy &= 1 \end{aligned} \quad (2.14)$$

Conditions specified in Eq. (2.14) can be satisfied through the normalization procedure proposed by Oger et al. (2007) [91]. Therefore, the original model of the pressure gradient in the work Khayyer and Gotoh (2011) [77] can be modified as:

$$\langle \nabla p \rangle_i = \frac{d}{n^0} \sum_{j \neq i} \frac{(p_j - p_i)}{|\vec{r}_j - \vec{r}_i|^2} (\vec{r}_j - \vec{r}_i) C_{ij} w_{ij} \quad (2.15)$$

where the corrective matrix C_{ij} is calculated by:

$$C_{ij} = \begin{bmatrix} \sum V_{ij} \frac{w_{ij} x_{ij}^2}{r_{ij}^2} & \sum V_{ij} \frac{w_{ij} x_{ij} y_{ij}}{r_{ij}^2} \\ \sum V_{ij} \frac{w_{ij} x_{ij} y_{ij}}{r_{ij}^2} & \sum V_{ij} \frac{w_{ij} y_{ij}^2}{r_{ij}^2} \end{bmatrix}^{-1} \quad (2.16)$$

and

$$V_{ij} = \frac{d}{\sum w_{ij}} \quad (2.17)$$

This modified pressure gradient model ensures the first-order consistency for pressure gradient, but not satisfying the conservation of momentum.

In the present work, Eqs. (2.15) and (2.16) were further modified to satisfy the conservation of momentum. In the work of the original high-order MPS method [77], it was considered that $\frac{w_{ij}}{r_{ij}} = \frac{\partial w_{ij}}{\partial r}$ with using the standard kernel function. In the present work, the standard kernel function is replaced by the C^2 Wendland kernel function. By changing the term, $\frac{w_{ij}}{r_{ij}}$, to $\frac{\partial w_{ij}}{\partial r}$, Eq. (2.15) can be written as:

$$\langle \nabla p \rangle_i = \frac{d}{n^0} \sum_{j \neq i} \frac{(p_j - p_i)}{|\vec{r}_j - \vec{r}_i|} (\vec{r}_j - \vec{r}_i) C_{ij} \frac{\partial w_{ij}}{\partial r} \quad (2.18)$$

where the corresponding corrective matrix C_{ij} is given by:

$$C_{ij} = \begin{bmatrix} \sum V_{ij} \frac{\partial w_{ij}}{\partial r} \frac{x_{ij}}{r_{ij}} x_{ij} & \sum V_{ij} \frac{\partial w_{ij}}{\partial r} \frac{x_{ij}}{r_{ij}} y_{ij} \\ \sum V_{ij} \frac{\partial w_{ij}}{\partial r} \frac{y_{ij}}{r_{ij}} x_{ij} & \sum V_{ij} \frac{\partial w_{ij}}{\partial r} \frac{y_{ij}}{r_{ij}} y_{ij} \end{bmatrix}^{-1} \quad (2.19)$$

where $\frac{\partial w_{ij}}{\partial r}$ can be obtained using Eq. (2.7). The pressure gradient in Eq. (2.18) is further modified to obtain the higher-order gradient model in symmetrical form as follow:

$$\langle \nabla p \rangle_i = \frac{d}{n^0} \sum_{j \neq i} \frac{(p_j + p_i)}{|\vec{r}_j - \vec{r}_i|} (\vec{r}_j - \vec{r}_i) C_{ij} \frac{\partial w_{ij}}{\partial r} \quad (2.20)$$

By using the modified pressure gradient model with the corrective matrix, the first-order consistency for pressure gradient can be guaranteed and the conservation of momentum can be satisfied.

2.4 Laplacian Model

In the present work, the higher-order Laplacian model, proposed by Khayyer and Gotoh (2010) [92], was employed to compute the Laplacian of velocity and pressure:

$$\begin{aligned} \langle \nabla^2 \phi \rangle_i &= \frac{1}{n^0} \sum_{j \neq i} \nabla \cdot \langle \phi_{ij} \nabla w_{ij} \rangle_i \\ &= \frac{1}{n^0} \sum_{j \neq i} \nabla \phi_{ij} \cdot \nabla w_{ij} + \phi_{ij} \nabla^2 w_{ij} \\ &= \frac{1}{n^0} \sum_{j \neq i} \phi_{ij} \left(\frac{\partial^2 w_{ij}}{\partial r^2} - \frac{1}{r_{ij}} \frac{\partial w_{ij}}{\partial r} \right) \end{aligned} \quad (2.21)$$

where $\frac{\partial w_{ij}}{\partial r}$ and $\frac{\partial^2 w_{ij}}{\partial r^2}$ are obtained from Eqs. (2.7) and (2.8), respectively.

2.5 Poisson Equations for Pressure

The Poisson equations for pressure can be derived by implicitly correcting the intermediate particle number density n_f^* to the initial value n_f^0 . The continuity equation can thus be satisfied. The Poisson equations for pressure in higher-order MPS method

are written as:

$$\langle \nabla^2 p^{k+1} \rangle_i = \frac{\rho_f}{n_f^0 \Delta t} \left(\frac{Dn_f^*}{Dt} \right)_i + ECS \quad (2.22)$$

The term of $\left(\frac{Dn_f}{Dt} \right)_i^*$ is calculated by:

$$\left(\frac{Dn_f}{Dt} \right)_i^* = - \sum_{j \neq i} \frac{1}{r_{ij}} \frac{\partial w_{ij}}{\partial r} (x_{ij}^* u_{ij}^* + y_{ij}^* v_{ij}^*) \quad (2.23)$$

where x_{ij}^* and y_{ij}^* are the components of the intermediate position vector \mathbf{r}_{ij}^* , u_{ij}^* and v_{ij}^* are the components of the intermediate velocity vector \mathbf{U}_{ij}^* , ECS denotes the error-compensating part in the source term given by Khayyer and Gotoh (2011) [77].

2.6 Particle Shifting

A particle shifting technique was applied for particle regularization based on Fick's laws of diffusion, which describes the diffusive flux from a high concentration area to a low concentration area of molecules. It has been widely applied in the improved WCSPH [93] and ISPH [94] methods. In the present method, the shifting vector for the particle i is defined as:

$$\delta \vec{r}_i = -D' \nabla C_i \quad (2.24)$$

where D' is a diffusion coefficient and C_i is the particle concentration at the location of the particle i , which can be calculated by:

$$\left\{ \begin{array}{l} D' = C_{\text{shift}} h^2 \\ \nabla C_i = \sum_{j \neq i} \frac{2}{n_i + n_j} \nabla w_{ij} \end{array} \right. \quad (2.25)$$

where the smoothing length h is set as $1.05l_0$ and the shifting coefficient C_{shift} is set as 0.01. l_0 is the initial particle spacing between two adjacent particles. The position of the particle i can be updated by:

$$\vec{r}_i^{\text{new}} = \vec{r}_i + \delta\vec{r}_i \quad (2.26)$$

Note that the particles on the free surface have less neighboring particles. This leads to a truncated-kernel error when applying the particle shifting technique. A simple solution is to set zero shifting displacement in the normal direction of the free surface [84], i.e., the particle shifting technique was applied to the fluid particles other than the free surface particles.

2.7 Structural Analysis

The structural analysis is based on the work by Kondo et al. (2007) [95] and Hwang et al. (2014) [96]. The volumetric strain of the i^{th} structural particle $\langle \varepsilon_V \rangle_i^k$ in Eq. (2.4) at the k^{th} time step can be calculated using the following equation:

$$\langle \varepsilon_V \rangle_i^k = \frac{d}{n_i^0} \sum_{j \neq i} \left(\frac{|\mathbf{r}_{ij}^k| - |\mathbf{r}_{ij}^0|}{|\mathbf{r}_{ij}^0|} w_{ij} \right) \quad (2.27)$$

where n_i^0 represents the initial number density of the structural particle i , $|\mathbf{r}_{ij}^0|$ is the initial particle spacing between particles i and j , $|\mathbf{r}_{ij}^k|$ is the distance between particles i and j at the k^{th} time step.

The divergence term of the isotropic pressure and the stress tensor in Eq. (2.4)

can be discretized as follows:

$$\frac{1}{\rho_s} \langle \nabla \cdot (\lambda_s \text{tr}(\varepsilon_{mn}) \delta_{mn}) \rangle_i^k = \frac{\lambda_s}{\rho_s} \frac{d}{n_i^0} \sum_{j \neq i} \left(\frac{\langle \varepsilon_V \rangle_i^k + \langle \varepsilon_V \rangle_j^k}{|\mathbf{r}_{ij}^0|} \frac{\mathbf{r}_{ij}^k}{|\mathbf{r}_{ij}^k|} w_{ij} \right) \quad (2.28)$$

$$\frac{1}{\rho_s} \langle \nabla \cdot (2\mu_s \varepsilon_{mn}) \rangle_i^k = \frac{2\mu_s}{\rho_s} \frac{d}{n_i^0} \sum_{j \neq i} \left(\frac{2\mathbf{r}_{ij}^k - R_i \mathbf{r}_{ij}^0 - R_j \mathbf{r}_{ij}^0}{|\mathbf{r}_{ij}^0|^2} w_{ij} \right) \quad (2.29)$$

where R_i and R_j denote the rotational matrices of the particle i and the neighboring particle j , respectively, at the k^{th} time step, and R_i is defined as:

$$R_i = \begin{bmatrix} \cos \theta_i & -\sin \theta_i \\ \sin \theta_i & \cos \theta_i \end{bmatrix} \quad (2.30)$$

where θ_i is the rotational angle of the particle i . The discretization of equations for conservation of angular momentum can be obtained using Eq. (2.31).

$$I_s \langle \frac{D}{Dt} \boldsymbol{\omega}_s \rangle_i^k = -\frac{m_s}{2} \sum_{j \neq i} R_i \mathbf{r}_{ij}^0 \times \left(\frac{2\mu}{\rho_s} \frac{d}{n_i^0} \frac{2\mathbf{r}_{ij}^k - R_i \mathbf{r}_{ij}^0 - R_j \mathbf{r}_{ij}^0}{|\mathbf{r}_{ij}^0|^2} \right) \quad (2.31)$$

2.8 Boundary Conditions

Various types of particles, as shown in Fig. 2.2, are used in the computations, including the free surface particles, fluid particles, wall particles, and dummy particles. Note that there is no air phase in the present method. Dummy particles are used to make the neighboring particles of wall particles sufficient. To obtain an accurate solution of the pressure gradient, it is important to avoid the misidentification of the free surface particles. A combination of density and non-symmetry criteria were developed in the present high-order MPS method to identify the free surface particles. The density

criteria in the original MPS method [60] was employed for the wall particles, and the non-symmetry criteria, proposed by Khayyer et al. (2009) [97] and improved by Zhang et al. (2013) [83], was used for the fluid particles. The combined criteria led to improved numerical stability [82]. Details of these criteria are illustrated as follows.

As shown in Fig. 2.2, considering a fluid particle and the four neighboring particles inside its interaction circle, $q1$, $q2$, $q3$ and $q4$. At the initial condition and assuming uniform particle distribution, $q1$ and $q4$ as well as $q2$ and $q3$ are symmetric about the fluid particle. Introducing a vector \vec{F} as defined in Eq. (2.35) to describe the level of non-symmetry, a zero amplitude of \vec{F} means all the neighboring particles are symmetric about a fluid particle. A small amplitude of \vec{F} for a fluid particle indicates its neighboring particles are more symmetrically distributed. For a free surface particle, as an example, $q1$, $q2$, $q3$ and $q4$ are not symmetric and its amplitude of \vec{F} will be larger. For the free surface with an arbitrary shape, the value could be larger. Particles satisfying Eq. (2.34) are identified as the free surface particles. On the free surface, since the pressure of a free surface particle is equal to the atmospheric pressure, the zero-pressure boundary condition is imposed on free surface particles.

$$n_i^k < \beta n^0 \tag{2.32}$$

$$N_i < \beta N^0 \tag{2.33}$$

$$\langle |\vec{F}| \rangle_i > \alpha |\vec{F}|^0 \tag{2.34}$$

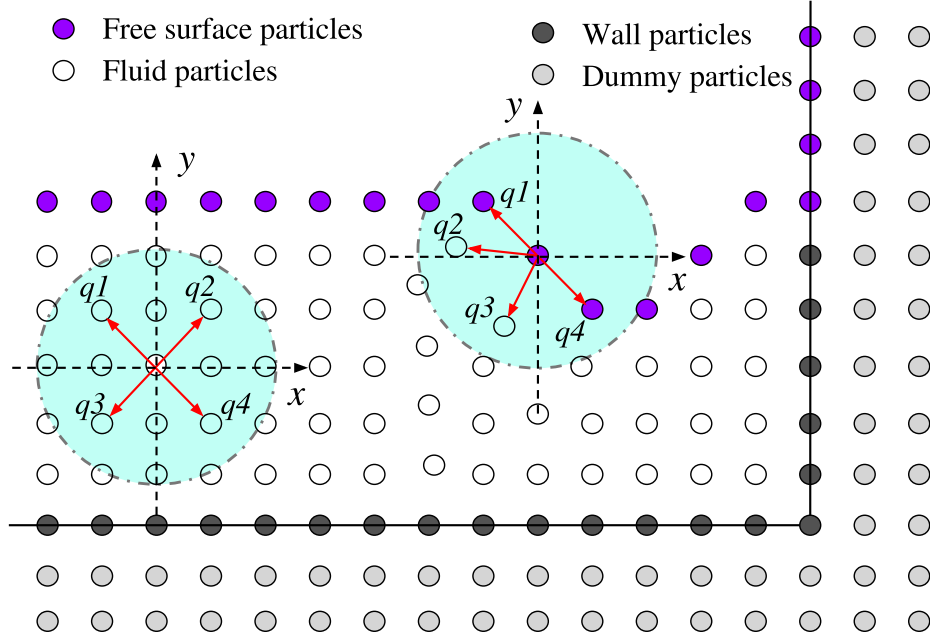


Figure 2.2: Free surface identification and boundary conditions

$$\langle \vec{F} \rangle_i = \frac{d}{n^0} \sum_{j \neq i} \frac{\vec{r}_i - \vec{r}_j}{|\vec{r}_i - \vec{r}_j|} w_{ij} \quad (2.35)$$

where $|\vec{F}|^0$ is the initial value of a free surface particle and α is typically set as 0.9, β is generally set as 0.97.

The improved scheme, however, often misidentifies the free surface particles for wall particles, which could lead to numerical divergence. In the present study, modifications were made to improve the numerical stability, where the non-symmetry criteria Eq. (2.34) was used for the fluid particles and the density criteria Eq. (2.32) was used for the wall particles separately. As it was tested and compared with other methods, the modified scheme was proved to be more efficient.

The wall boundary condition can be simulated by using three layers of particles, as

shown in Fig. 2.2. One layer of wall particles was distributed along the wall boundary, and the other two layers of dummy particles were placed outside the wall boundary along the normal directions of the wall particles. Pressures of all fluid particles and wall particles are solved from the Poisson equations, while pressures of the dummy particles are extrapolated using those of their neighboring particles. Zero-velocity conditions are imposed on no-slip fixed wall boundaries. For moving-wall boundaries, velocities must be prescribed or computed.

2.9 Particle Spacings for Fluid and Structure

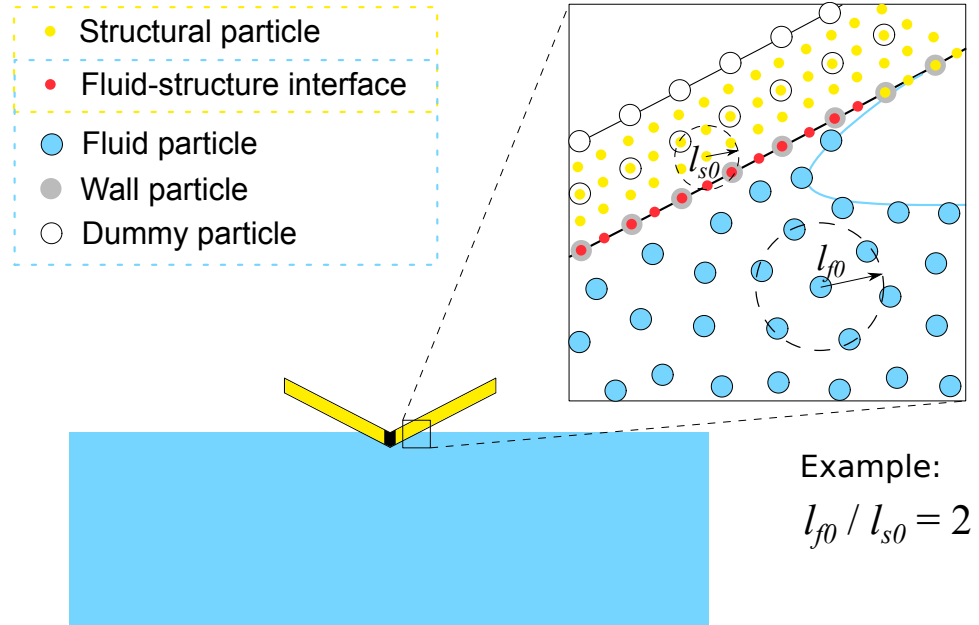


Figure 2.3: Different particle spacings for the fluid and the structure

Since the properties of fluid and structures are different, different particle spacings are used to ensure accurate predictions of fluid and structural responses. As

shown in Fig. 2.3, l_{f0} and l_{s0} represent the initial particle spacings for the fluid and the structure, respectively. A small circle represents a structural particle and larger circles denote fluid particles, wall particles and their dummy particles. Consequently, the pressures on the fluid-structure interface can be interpolated from pressures of their adjacent wall particles, which are obtained by solving the Poisson equations for pressure in the hydrodynamic analysis.

With applying the technique of varying particle spacings for the fluid and the structure, the structural particles can be extremely refined so that an accurate solution for the structural responses can be achieved.

2.10 Searching Neighbouring Particles

As shown in Fig. 2.4, background cells are used to search neighbouring particles. The cell size is constant, which equals the radius of interaction region of particles. After initialization, all particles are assigned to cells with indices. For example, the particle i is in the cell P . Generally, 9 cells including P itself and the neighbouring cells are used to search particles. The distance between the particle i and a particle j inside these cells are calculated. If the distance is less than the radius of interaction region, the particle j will be counted as a neighbouring particle of the particle i . This process is repeated for all the particles. Neighbouring particles are in pair. If a particle j has been identified as a neighbouring particle of a particle i , then the particle i can be skipped when searching the neighbouring particles of the particle j .

Practically, only 5 cells, i.e., P , E , NE , N and NW as shown in Fig. 2.4 are necessary for the searching. After searching the five cells, i.e., P , E , NE , N and

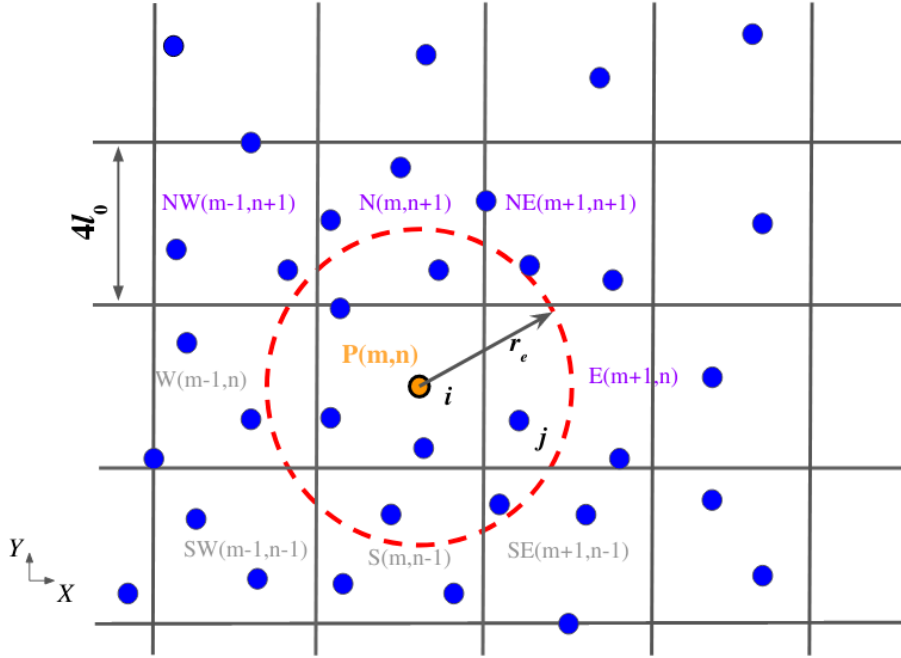


Figure 2.4: Searching neighbouring particles

NW, for the particle i , the neighbouring particles of i are obtained, e.g., j . A pair of i - j can be recorded since i is also one of the neighboring particle of j . Considering searching the cells for j . Now the E cell in the figure is called P cell for j , and the P cell in the figure is called W for j . In the figure, searching the cell E to P for particle i is the same as searching the cell W to P for particle j . Thus it is not necessary to repeat the searching W cell for j . Note that it is required to search cell by cell in order, e.g., towards the direction $X > 0$ and then the direction $Y > 0$ so that only five cells are sufficient for searching.

This searching approach has been proved to be very efficient in the present study.

2.11 FSI Coupling

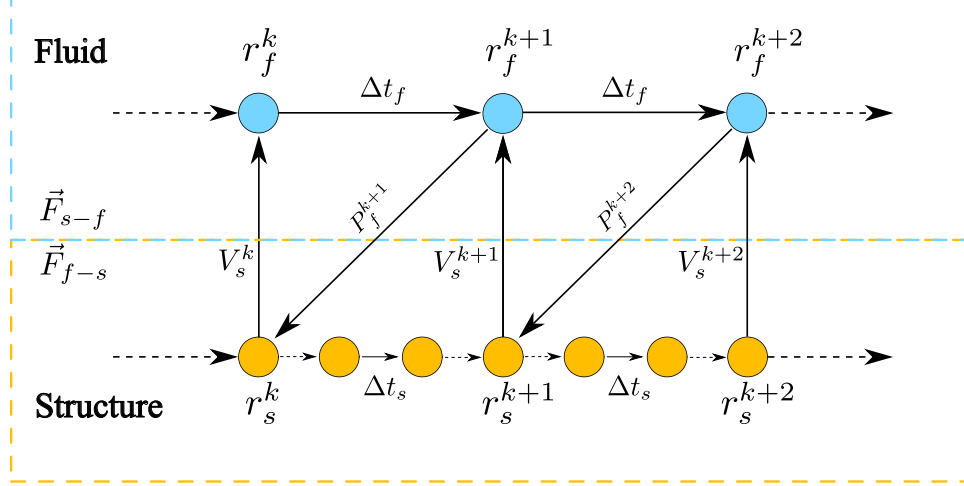


Figure 2.5: The CSS coupling scheme for FSI computation

In the present work, the conventional serial staggered (CSS) procedure, a weak two-way coupled scheme, was employed for the coupling of fluid and structure, as shown in Fig. 2.5. The horizontal arrows denote the time marching. Different time steps can be used for the fluid particles and the structural ones. For example, the time step for structural analysis is $\Delta t_s = \frac{1}{3}\Delta t_f$. In this case, three yellow points would interact with the blue points while the rest four yellow points are used only for structural analysis for time marching.

In the FSI computation, the hydrodynamic analysis was carried out first to obtain the forces on the fluid-structure interface. The interface information was then updated according to the structural analysis results. The the flow chart for the proposed algorithm of MPS method is given in Fig. 2.6. The FSI solution procedure at each step is summarized below:

1. Generating fluid and structure particles and setting initial conditions.
2. Calculating the intermediate velocity V_f^* of fluid particles.
3. Calculating the velocity divergence term $\nabla \cdot V_f^*$ of fluid particles.
4. Identifying particles on the free surface.
5. Solving the Poisson equations for pressure using the parallel bi-conjugate gradient stabilized method (BiCGSTAB) to obtain p_f^{k+1} .
6. Computing forces \vec{F}_{f-s} on the particles on the fluid-structure interface and starting the structural analysis.
7. Searching the neighboring particles of the structure particles.
8. Computing the strain ε^{k+1} , the stress σ^{k+1} , the translational and angular accelerations, the velocity V_s^{k+1} , and the angular velocity ω_s^{k+1} .
9. Updating the displacement r_s^{k+1} and the rotational angle θ_s^{k+1} . The interface particles are updated and used as new boundary conditions for the fluid analysis.
10. Computing pressure gradient ∇p_f^{k+1} for the fluid particles.
11. Updating the velocity V_f^{k+1} and displacement r_f^{k+1} of fluid particles.
12. Advancing to the next step by repeating Step 2.

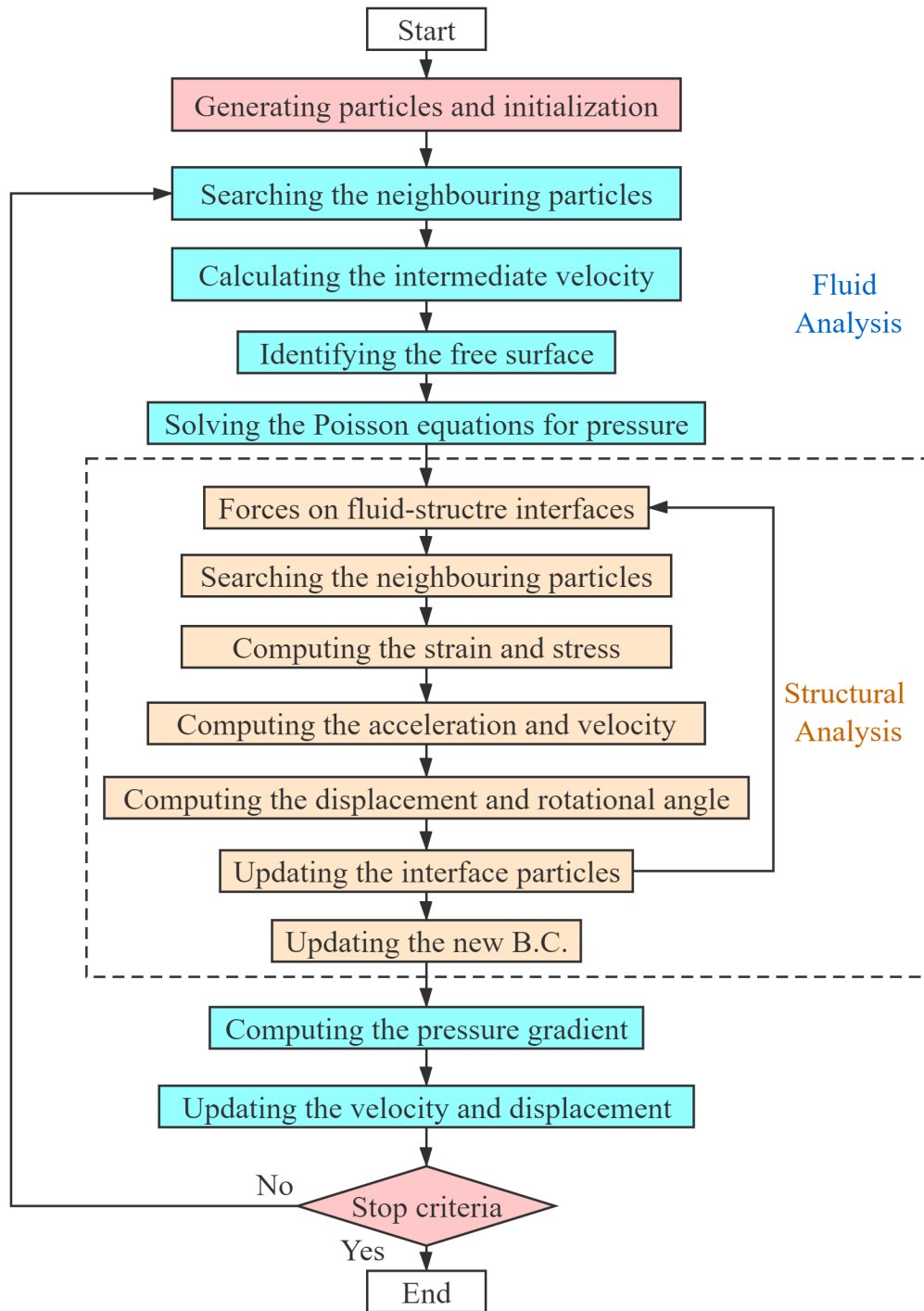


Figure 2.6: The flow chart for the proposed algorithm of MPS method

2.12 Parallel Computing Scheme and Domain Decomposition

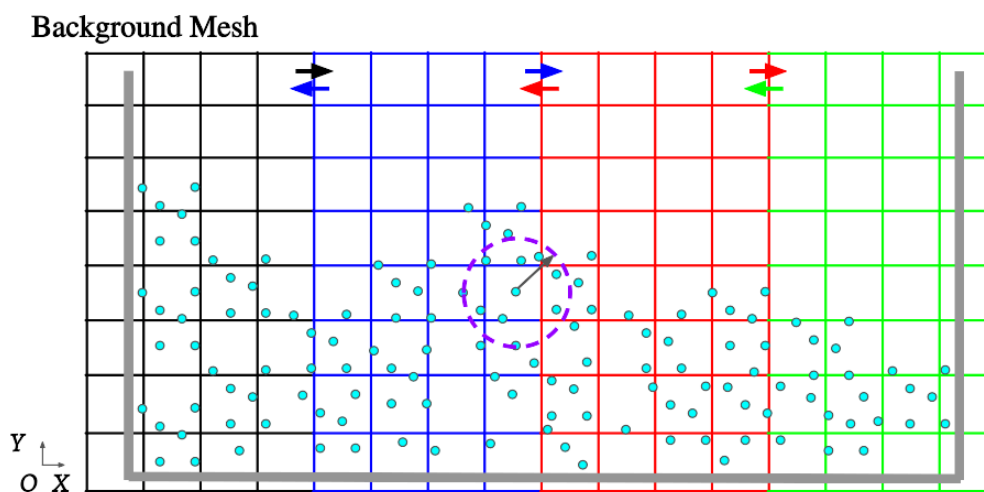


Figure 2.7: Parallel computing scheme and domain decomposition

A parallel scheme was developed based on the message passing interface (MPI) method. Particles were grouped by using virtual background cells, shown in Fig. 2.7. Every cell size is equal to the radius of interaction region of particles. Note that this background mesh is the same one used to search the neighbouring particles. As illustrated in the figure for an example, four decomposed domains were used to achieve balanced load for each processor and the information is exchanged on the domain interfaces. Since particles can move arbitrarily, the size of the decomposed domains will also change. After initialization, the main processor will collect all particles information and decompose domains for all particles. Computations are

independent in each domain and only the adjacent cells at the boundary of two decomposed domains are used for information exchange. Finally, results are sent back to the main processor and the simulation advances to the next time step.

With respect to the computing cost, for a typical case with 1 million particles, the required memory is about 4 GB per CPU core. Using Intel(R) Xeon(R) CPU E5-2683 v3 for the present simulations, the computing time was about 2.5 days for one FSI case using 40 cores. Note that the physical time for a typical slamming case with FSI is about 30 ms.

2.13 Uncertainty Analysis

Based on the Grid Convergence Index (GCI) method [85], a similar approach, i.e., the Particle Convergence Index method (PCI), is developed to evaluate uncertainties in solutions with Lagrangian particle-based methods. In this method, the initial particle spacing represents the spatial resolution. The procedure for calculating PCI based on Richardson extrapolation (RE) method is given below.

Considering three sets of particle resolutions with particle spacings, l_1, l_2 and l_3 , where l_1 is the smallest one, numerical solutions of an interested variable ϕ for the three cases are denoted as ϕ_1, ϕ_2 and ϕ_3 , respectively. In 2-D simulations, particle spacings, l_j ($j = 1, 2, 3$), are defined as:

$$l_j = \left[\frac{1}{N_j} \sum_{i=1}^{N_j} (\Delta V_i) \right]^{1/2} \quad (2.36)$$

where ΔV_i is the volume of particle i , and N_j is the total number of particles.

The refinement factors are defined as $r_{21} = l_2/l_1$ and $r_{32} = l_3/l_2$. The apparent

order, p , can be calculated by:

$$p = \frac{1}{\ln(r_{21})} \left| \ln |\varepsilon_{32}/\varepsilon_{21}| + \ln \left(\frac{r_{21}^p - s}{r_{32}^p - s} \right) \right| \quad (2.37)$$

where $\varepsilon_{32} = \phi_3 - \phi_2$, $\varepsilon_{21} = \phi_2 - \phi_1$, and $s = \text{sgn}(\varepsilon_{32}/\varepsilon_{21})$. Equation (2.37) can be solved by the fixed-point iteration method. After p is obtained, the extrapolated values are calculated by:

$$\phi_{\text{ext}}^{21} = \frac{r_{21}^p \phi_1 - \phi_2}{r_{21}^p - 1} \quad (2.38)$$

The approximate relative error and the extrapolated relative error can be determined by:

$$e_a^{21} = \left| \frac{\phi_1 - \phi_2}{\phi_1} \right| \quad (2.39)$$

$$e_{\text{ext}}^{21} = \left| \frac{\phi_{\text{ext}}^{21} - \phi_1}{\phi_{\text{ext}}^{21}} \right| \quad (2.40)$$

The uncertainty in the solutions with the smallest particle spacing due to spatial discretization is then estimated as:

$$\text{PCI}_{\text{fine}}^{21} = \frac{1.25 e_a^{21}}{r_{21}^p - 1} \quad (2.41)$$

Therefore, the interval that covers the exact solution with a high confidence level is given as:

$$\phi_1 - \text{PCI}_{\text{fine}}^{21} \phi_1 \leq \phi_{\text{exact}} \leq \phi_1 + \text{PCI}_{\text{fine}}^{21} \phi_1 \quad (2.42)$$

Chapter 3

Solving 2-D Dam Breaking

The present numerical method was first validated by its application to solve a 2-D dam breaking problem of a water column. The experiments on a dam breaking flow over a horizontal dry bed and impacting a vertical wall were investigated by Lobovsky et al. (2014) [98]. The computational domain, the boundary conditions and the coordinate system are presented in Fig. 3.1. The initial width and height of the water column were 0.6 m and 0.3 m, respectively. The length and the height of the tank is set as 1.61 m and 0.9 m, respectively. To study the wave impacting, a pressure sensor is set on the right wall at the point P, which is 3 mm above the bed. Water elevations were recorded at the locations of H1, H2 and H3.

For the boundary conditions in the present simulations, no-slip wall boundary conditions were applied on the bed and walls. The kinematic and dynamic boundary conditions were imposed on the free surface, as defined in Eqs. (3.1) and (3.2). The kinematic boundary condition means there is no flow through the free surface. For the dynamic boundary condition, since the pressure on the free surface equals to the

atmospheric pressure, it was set as zero in the present work since only the water phase is considered.

$$\mathbf{U}_f \cdot \mathbf{n} = 0 \quad (3.1)$$

$$p = 0 \quad (3.2)$$

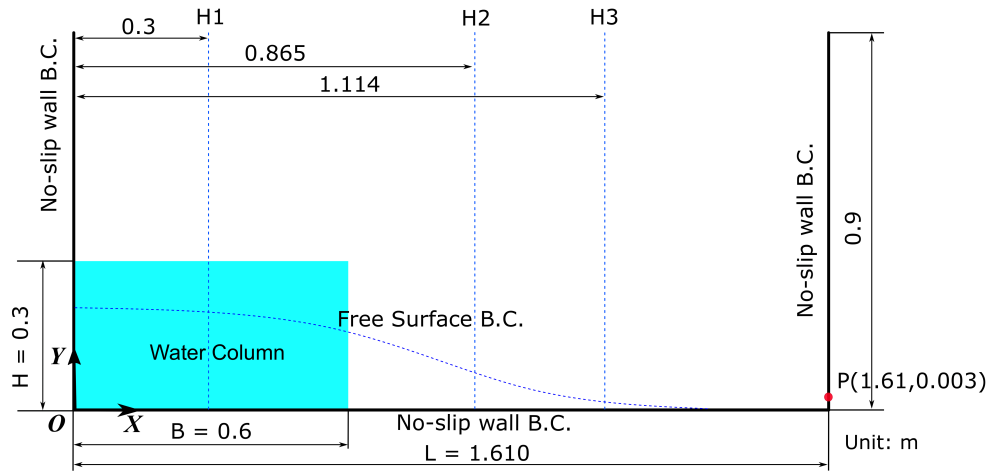


Figure 3.1: Computational domain for 2-D dam breaking

3.1 Convergence Studies

The sensitivity of numerical solutions to the particle spacing was first investigated by using three sets of particles as presented in Table 3.1. The time steps were chosen based on the Courant-Friedrichs-Lewy (CFL) condition. In all the three cases, the CFL number, defined as $CFL = V\Delta t/l_0$, was set as 0.2. Time histories for pressures

Table 3.1: Case matrix of convergence studies for 2-D dam breaking

Case No.	Total number of particles	Particle spacing, l_0 (m)	Time step, Δt (s)	CFL
1	7,324	6.0×10^{-3}	2.8×10^{-4}	0.2
2	13,036	4.2×10^{-3}	2.0×10^{-4}	0.2
3	24,600	3.0×10^{-3}	1.4×10^{-4}	0.2
4	45,616	2.1×10^{-3}	1.0×10^{-4}	0.2
5	45,616	2.1×10^{-3}	1.4×10^{-4}	0.28
6	45,616	2.1×10^{-3}	2.0×10^{-4}	0.4

at P(1.61,0.003) based on four particle spacings are presented in Fig. 3.2. The pressure fluctuations were reduced by using smaller particle spacing. It can be observed that the numerical solutions converged as the particle spacing was reduced. Furthermore, uncertainties in the peak pressures due to spatial resolution by the present method were evaluated. The PCI's and the intermediate details are presented in Table 3.2. It can be seen that uncertainties due to spatial resolution are small. Time histories for the water level elevations measured at H1, H2 and H3 are also shown in Fig. 3.4. It is indicated that the numerical results of the water level converged to the particle spacing. Therefore, the particle spacing of $l_0 = 2.1 \times 10^{-3}$ m was employed in the following studies.

The study of temporal convergence was then carried out, also listed in Table 3.1. The total number of particles was set as 45,616. The corresponding CFL numbers

Table 3.2: Uncertainties in predicted peak pressure due to spatial resolution l_0 for 2-D dam breaking

Item	Uncertainties due to l_0
h_1	2.1×10^{-3}
h_2	3.0×10^{-3}
h_3	4.2×10^{-3}
ϕ_1	2.810
ϕ_2	2.974
ϕ_3	3.792
p	4.84
ϕ_{ext}^{21}	2.774
e_a^{21}	5.85%
e_{ext}^{21}	1.28%
$\text{PCI}_{\text{fine}}^{21}$	1.59%

were 0.2, 0.28 and 0.4, respectively. The time histories for pressures at P(1.61,0.003) with different time steps are presented in Fig. 3.3 and for the water level elevations measured at H1, H2 and H3 are shown in Fig. 3.5. The pressure fluctuations were reduced by using smaller time steps. It can be observed that the numerical solutions converged as the time step was decreased. The time step, $\Delta t = 1.0 \times 10^{-4}$ s, was then adopted.

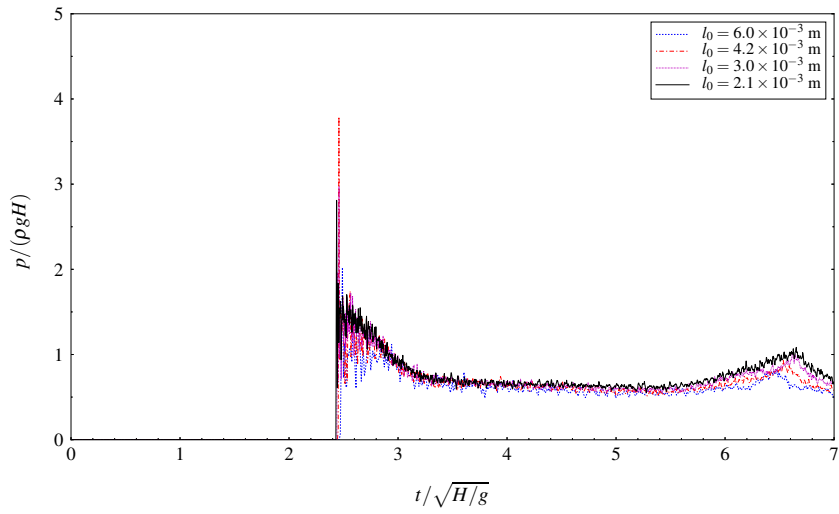


Figure 3.2: Spatial convergence of impact pressure for 2-D dam breaking

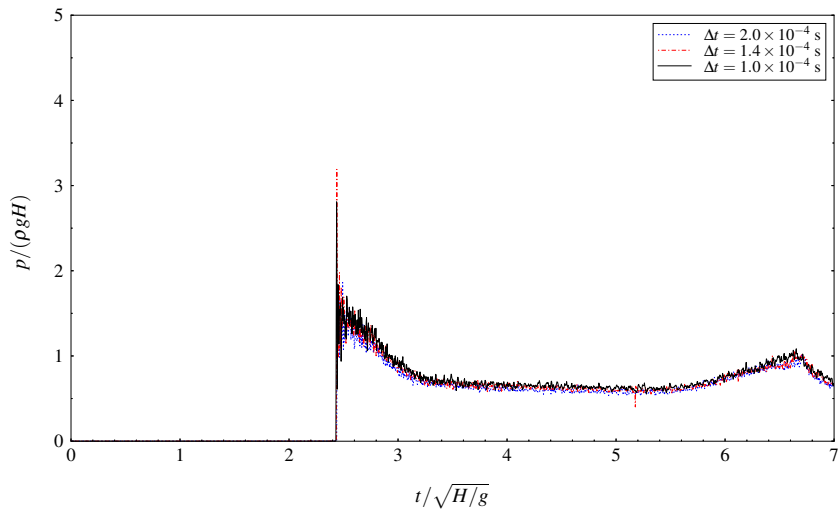
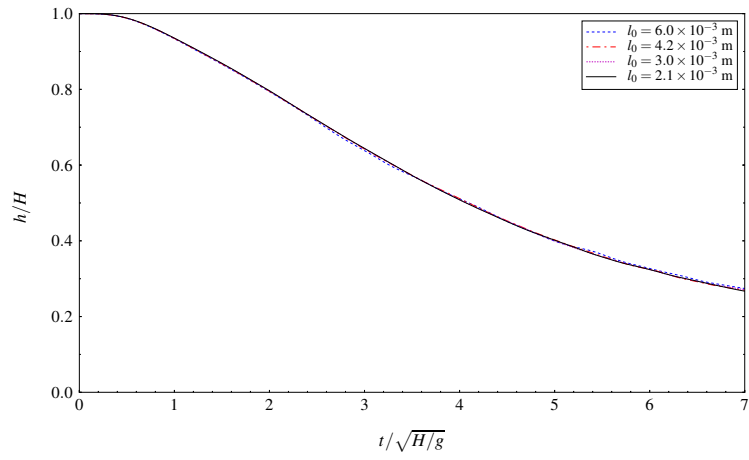
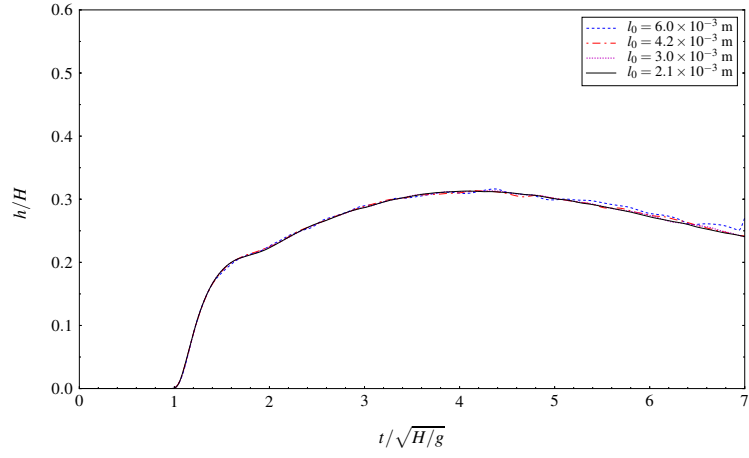


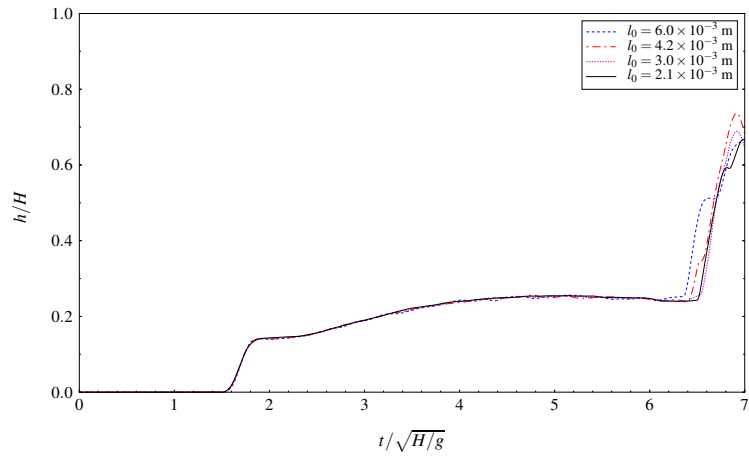
Figure 3.3: Temporal convergence of impact pressure for 2-D dam breaking



(a) Water level elevations at H1

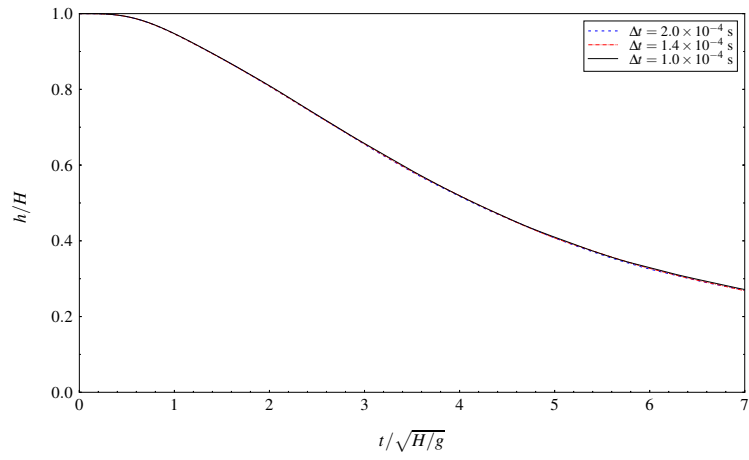


(b) Water level elevations at H2

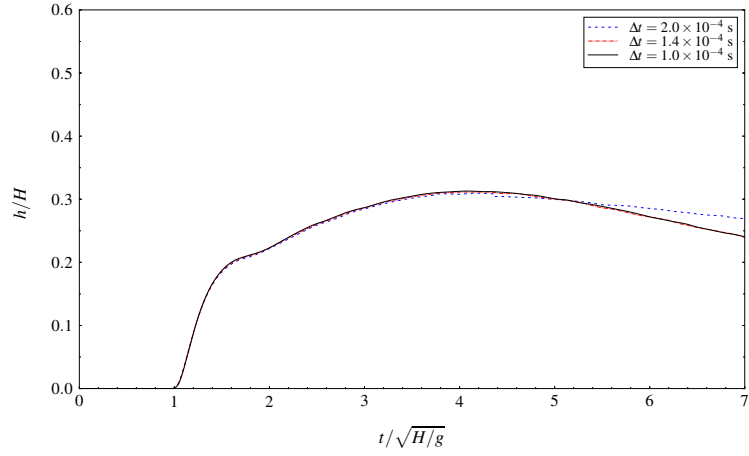


(c) Water level elevations at H3

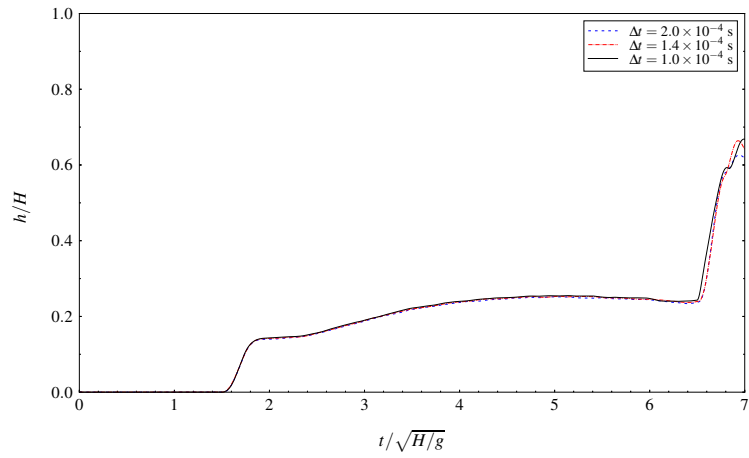
Figure 3.4: Spatial convergence of water level elevations for 2-D dam breaking



(a) Water level elevations at H1



(b) Water level elevations at H2



(c) Water level elevations at H3

Figure 3.5: Temporal convergence of water level elevations for 2-D dam breaking

3.2 Numerical Results of Impact Pressure

The results presented below were obtained using 45,616 particles with a particle spacing of $l_0 = 2.1 \times 10^{-3}$ m and a time step of $\Delta t = 1.0 \times 10^{-4}$ s. The predicted time history of the impact pressure at P(1.61,0.003) is given in Fig. 3.6. The result by the present method is also compared with the experimental data Lobovsky et al. (2014) [98], the numerical results obtained using the first-order gradient model in symmetrical form [89], and those by the original higher-order gradient model [77]. The pressure fluctuations were suppressed by the present model. The peak values are listed in Table 3.3 as well as their relative errors in comparison with the experimental data. It can be observed that the predicted value agrees well with the experimental data Lobovsky et al. (2014) [98].

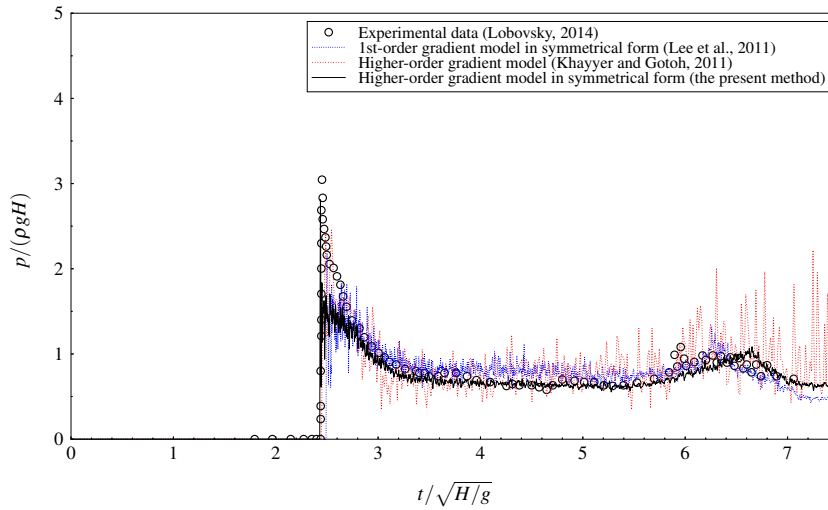


Figure 3.6: Comparison of impact pressure at the point P(1.61,0.003) for 2-D dam breaking

Table 3.3: Results of peak impact pressure for 2-D dam breaking

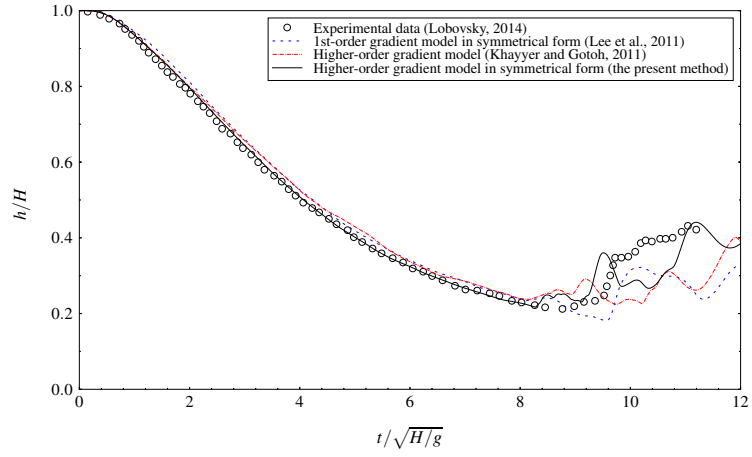
Methods	Peak pressure	
	$p/\rho gh$	Error
Experimental data [98]	3.046	-
First-order gradient model [89]	2.181	28.4%
Higher-order gradient model [77]	2.453	19.5%
The present method	2.810	7.7%

3.3 Free Surface Elevation

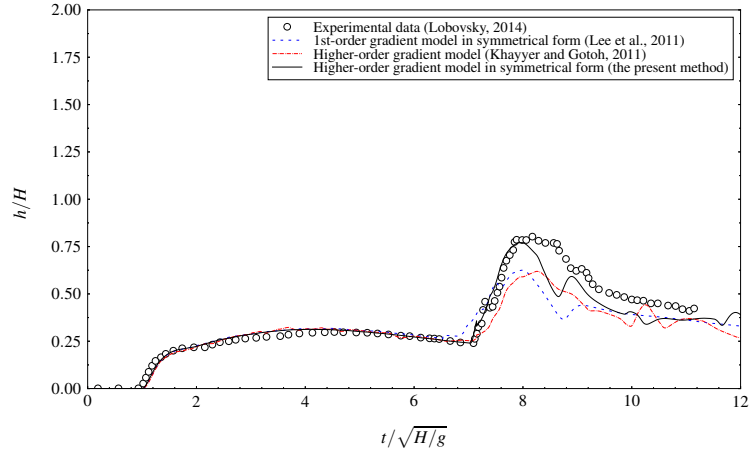
The predicted time histories of water level elevations are shown in Fig. 3.7. The results are also compared with the experimental data by Lobovsky et al. (2014) [98], the numerical results obtained using the first-order gradient model in symmetrical form [89], and those by the original higher-order gradient model [77]. The predicted water level elevations at the locations H1, H2, and H3 were improved by using the present higher-order gradient model. The numerical results agreed well with the experimental data [98].

The pressure fields and the free surface at $t = 1.17$ s are also compared in Fig. 3.8. The unphysical noises shown in the results of using the first-order gradient model and the original higher-order gradient model are reduced in those by applying the present higher-order method. The pressure fields and free surface at $t = 0.28$ s, 0.57 s, 0.86 s and 1.17 s are compared in Fig. 3.9. The results of the free surface are generally in good agreement with those by Lobovsky et al. (2014) [98].

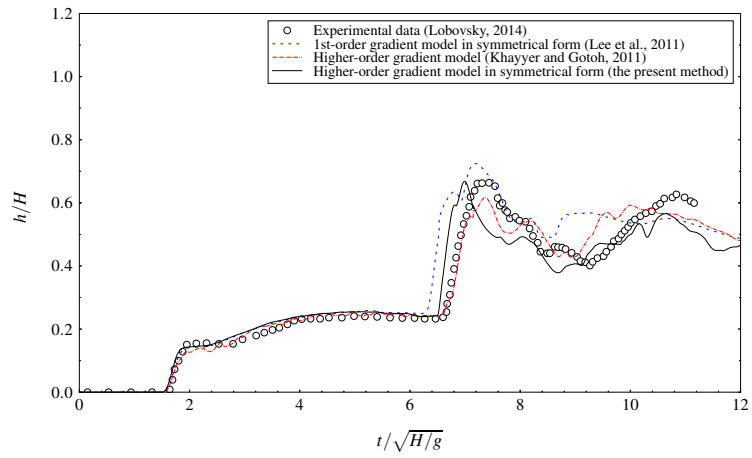
In summary, the present higher-order method with the improved gradient model led to improved predictions of the impact pressures and the free surface for simulations of the two-dimensional dam breaking flow.



(a) Water level elevations at H1

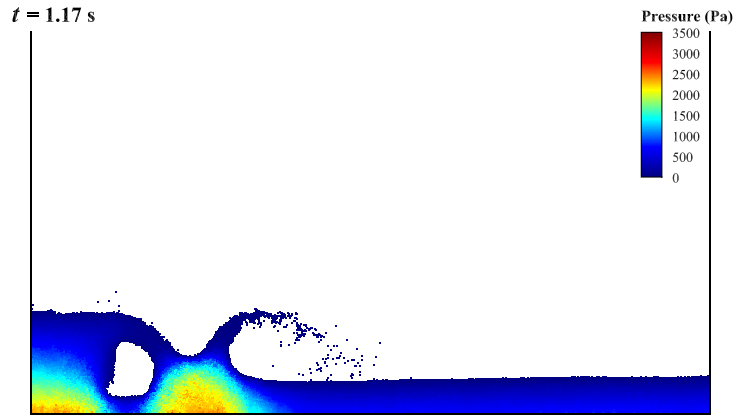


(b) Water level elevations at H2

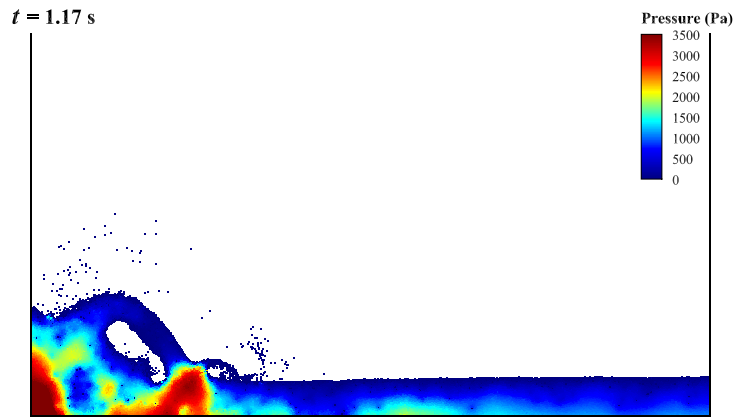


(c) Water level elevations at H3

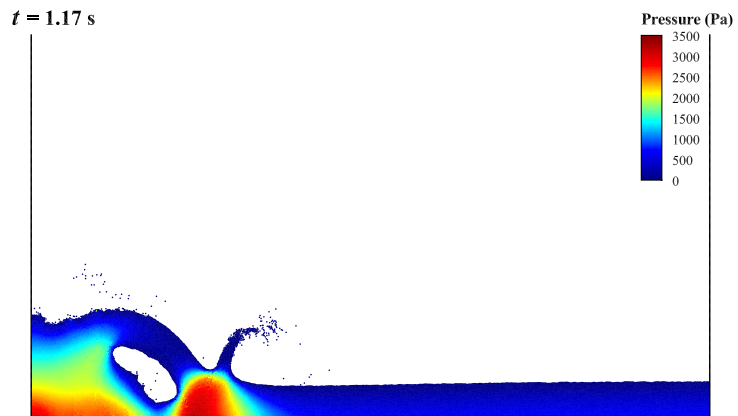
Figure 3.7: Comparison of water level elevations for 2-D dam breaking



(a) First-order gradient model [89]

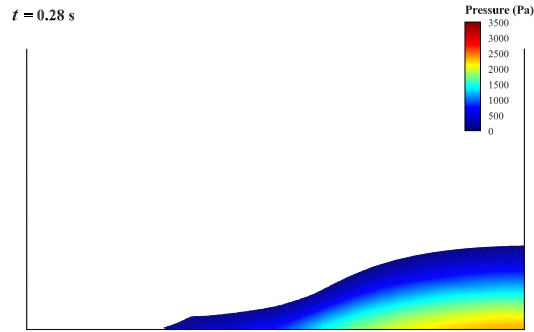


(b) Higher-order gradient model [77]

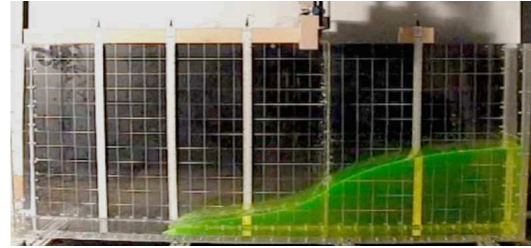


(c) The present method

Figure 3.8: Comparison of pressure fields and free surface for 2-D dam breaking



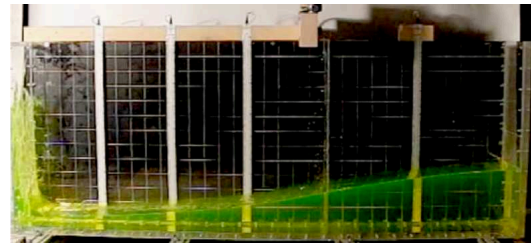
(a) The present method ($t = 0.28$ s)



(b) Experimental snapshot [98] ($t = 0.28$ s)



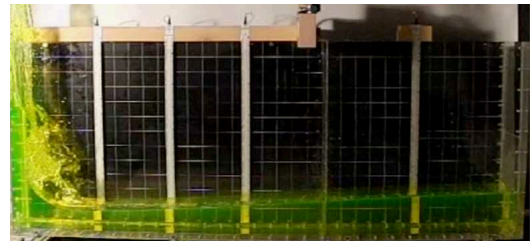
(c) The present method ($t = 0.57$ s)



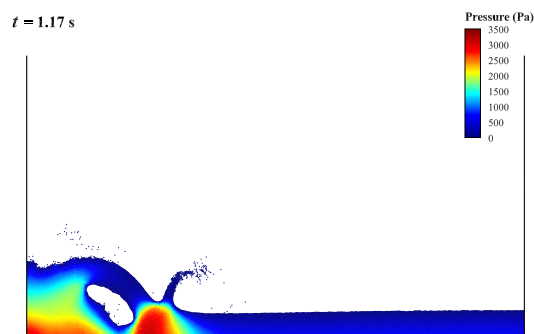
(d) Experimental snapshot [98] ($t = 0.57$ s)



(e) The present method ($t = 0.86$ s)



(f) Experimental snapshot [98] ($t = 0.86$ s)



(g) The present method ($t = 1.17$ s)



(h) Experimental snapshot [98] ($t = 1.17$ s)

Figure 3.9: Pressure fields and free surface for 2-D dam breaking

Chapter 4

Solving 2-D Vibration of a Thin Plate

The structure model was verified by applying it to the vibration of a two-dimensional thin plate clamped at the left end and free at the right end, as shown in Fig. 4.1.

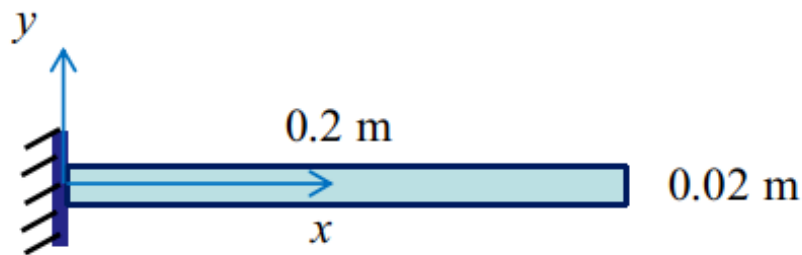


Figure 4.1: Set-up of 2-D vibration of a thin plate

Based on the work of Gray et al. (2001) [99], the length and thickness of the plate were set as $L = 0.2$ m and $H = 0.02$ m. The density, bulk modulus and the shear modulus of the plate were $\rho_s = 1.0 \times 10^3$ kg/m³, $K = 3.25 \times 10^6$ N/m³ and

$\mu = 7.15 \times 10^5 \text{ N/m}^3$, respectively. The corresponding Young's modulus and the Poisson ratio are $E = 2.0 \times 10^6 \text{ N/m}^2$ and $\nu_s = 0.3975$, respectively. The following initial velocities were imposed on the plate:

$$\begin{aligned} v_x &= 0 \\ v_y &= V_f c_0 \frac{[M(\cos(kx) - \cosh(kx)) - N(\sin(kx) - \sinh(kx))]}{Q} \end{aligned} \quad (4.1)$$

where

$$\begin{aligned} c_0 &= \sqrt{\frac{K}{\rho_s}} \\ M &= \sin(kL) + \sinh(kL) \\ N &= \cos(kL) + \cosh(kL) \\ Q &= 2(\cos(kL) \sinh(kL) - \sin(kL) \cosh(kL)) \end{aligned} \quad (4.2)$$

where the k is determined by the solutions of

$$\cos(kL) \cosh(kL) = -1 \quad (4.3)$$

The lowest natural vibration frequency at which the structural deformation occurs is the first mode or the fundamental mode. The first mode usually defines the highest loads in a structure. In the present study, the fundamental mode, i.e., $kL = 1.875$, was simulated. The corresponding initial velocity of the free end is $V_f c_0 = 0.57 \text{ m/s}$. The spatial convergence study involved five sets of particle spacings, $l_{s0} = 2.0 \times 10^{-3} \text{ m}$, $1.4 \times 10^{-3} \text{ m}$, $1.0 \times 10^{-3} \text{ m}$, $0.7 \times 10^{-3} \text{ m}$ and $0.5 \times 10^{-3} \text{ m}$. The number of particles were 1,050, 2,030, 4,100, 7,980 and 16,200, respectively. The time steps were chosen based on the CFL condition. The maximum CFL number, $V_{max} \cdot \Delta t / l_0$, was set as 4×10^{-3} for all the five cases. Time histories of the displacement of the free end are presented in Fig. 4.2. It can be seen that numerical results converged as the particle

spacing was decreased. The particle spacing $l_{s0} = 0.5 \times 10^{-3}$ m was therefore used in the following simulations.

Three cases with different time steps were employed to investigate the temporal convergence, i.e., $\Delta t_f = 5.0 \times 10^{-6}$ s, 3.5×10^{-6} s and 2.5×10^{-6} s. The particle spacing was fixed as $l_{s0} = 0.5 \times 10^{-3}$ s and the corresponding particle number was 16,200. The predicted displacements of the plate free end are presented in Fig. 4.3. It is indicated that the time step has little impact on the amplitude of displacement and the period of vibration in the range studied.

Table 4.1: Comparison of the non-dimensional period and amplitude for the displacement of the plate free end

Method	Non-dimensional period, $T_0 = T_{c0}/L$	Non-dimensional amplitude, $A_0 = A/L$
SPH (Gray et al. [99])	82.00	0.125
SPH (Sabahi and Nikseresht [100])	80.95	0.125
Analytical solution (Hwang et al. [96])	72.39	0.115
Present method	71.52	0.113

The final structural responses were obtained by using 16,200 structural particles with a particle spacing of $l_{s0} = 0.5 \times 10^{-3}$ m and the time step of $\Delta t = 2.5 \times 10^{-7}$ s. The strain contours of the elastic plate at various time instants are shown in Fig. 4.5. As presented in Fig. 4.4, the predicted time history of the deformation of the free end is in good agreement with the analytical solution by Hwang et al. (2014) [96]

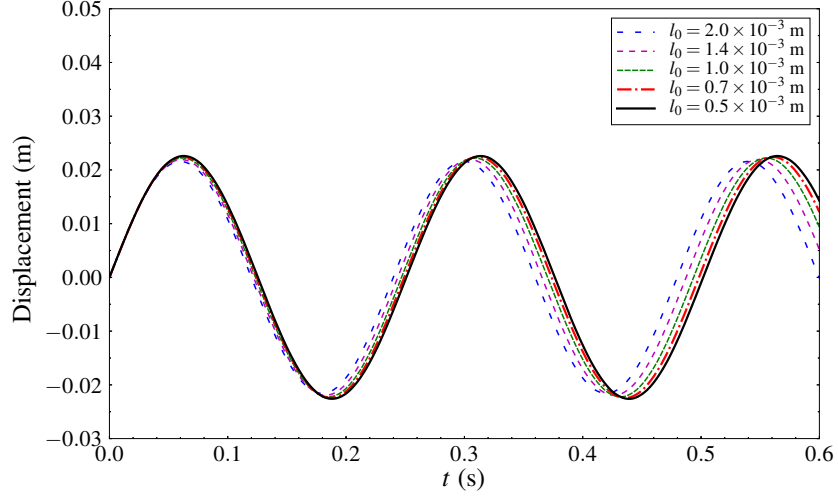


Figure 4.2: Spatial convergence of displacement at the plate's free end

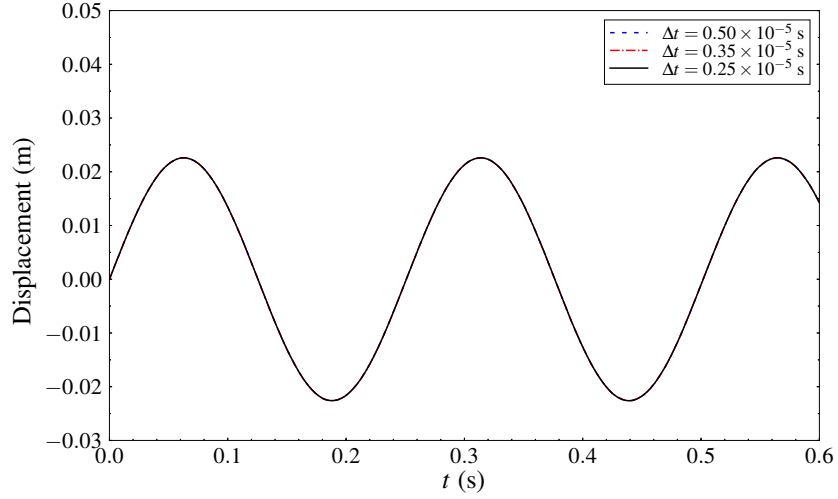


Figure 4.3: Temporal convergence of displacement at the plate's free end

Improved results were obtained by the present method in comparison with solutions by the WCSPH method [100]. The non-dimensional period and amplitude are also listed in Table 4.1. It can be seen that the present results are in good agreement

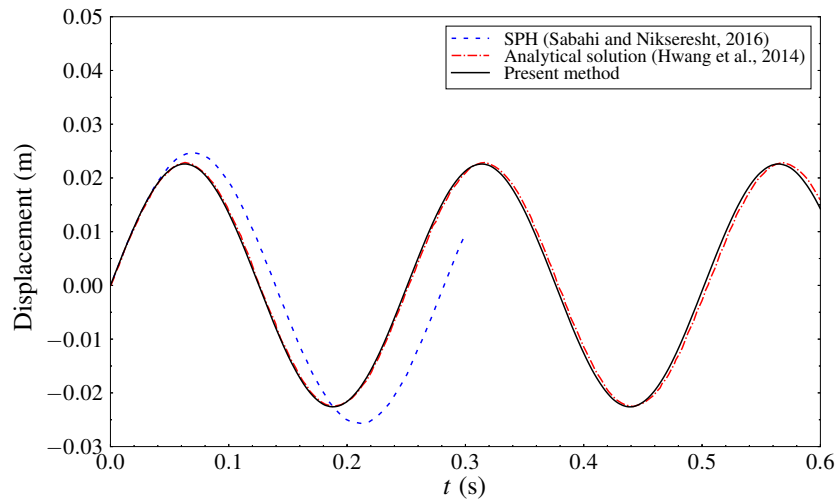
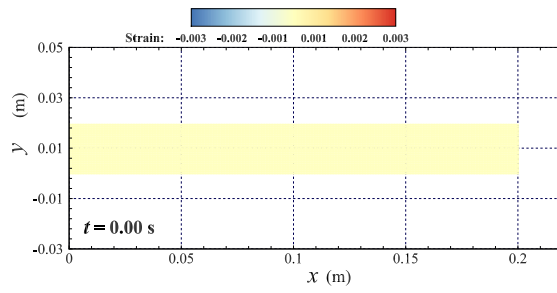
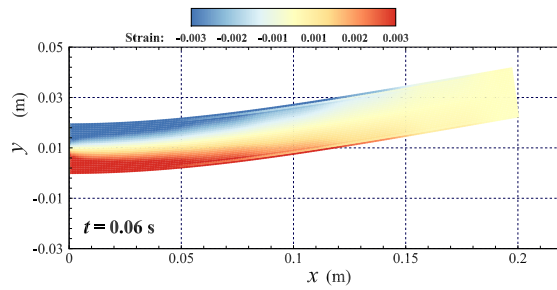


Figure 4.4: Comparison of the displacement at the plate's free end

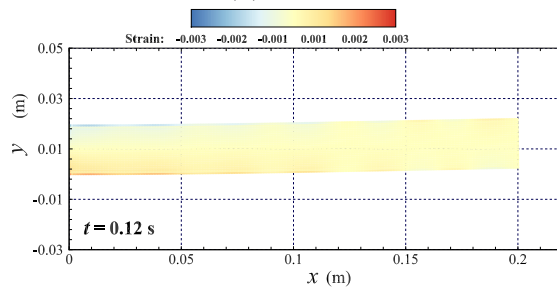
with the analytical solutions. The structural analysis was improved by the present method.



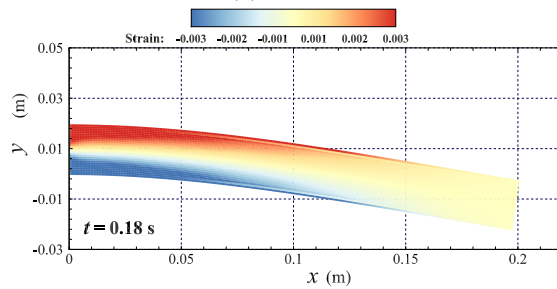
(a) $t = 0.00$ s



(b) $t = 0.06$ s



(c) $t = 0.12$ s



(d) $t = 0.18$ s

Figure 4.5: Strain contours of the elastic plate at four time instants

Chapter 5

Solving 2-D Slamming of Wedges and Ship Sections

Validation studies were carried out for the free-fall water entry of a 2-D wedge with three tilt angles (see θ in Fig. 5.2 for the definition of the tilt angle) and two different ship sections. Convergence of numerical solution to the size of computational domain, the particle spacing and the time step was investigated. Uncertainties in the numerical results with respect to the particle resolution were quantified. The predicted impact pressures and forces by the present method are in good agreement with experimental data. In comparison with results by the first-order gradient model in symmetrical form and those by the original higher-order gradient model, numerical solutions were improved by the present method.

5.1 2-D Wedge with Different Tilt Angles

In this section, water entry of a 2-D wedge with different tilt angles was first investigated using the improved higher-order MPS method. Experiments were conducted by the Korea Research Institute of Ships and Ocean Engineering (KRISO) and the experimental data were presented in the work of Hong et al. (2017) [26]. In the present simulations, the deadrise angle of the wedge was $\alpha = 30^\circ$ and its width was 0.6 m. The tilt angles θ were set as 0° , 10° and 20° . As shown in Fig. 5.1, two pressure sensors were installed at P1 and P2 in the experiments and a load cell was located at F for force measurement.

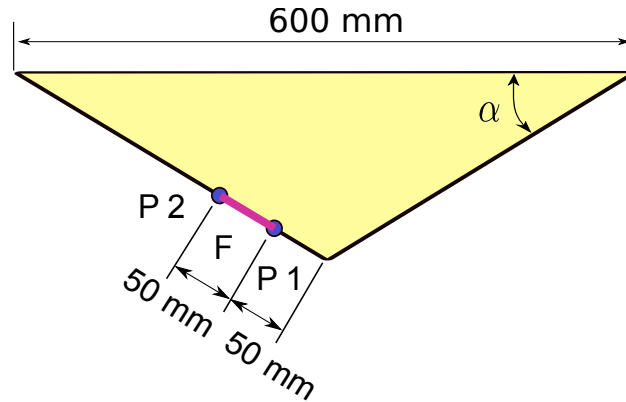


Figure 5.1: Sensors on the wedge surface

The computational domain with the width, L , and the depth, D , is illustrated in Fig. 5.2. The height of the side walls was set as $1.5D$. The drop velocities, i.e., the velocities of the body during its dropping, were prescribed according to the experimental ones as shown in Fig. 5.3.

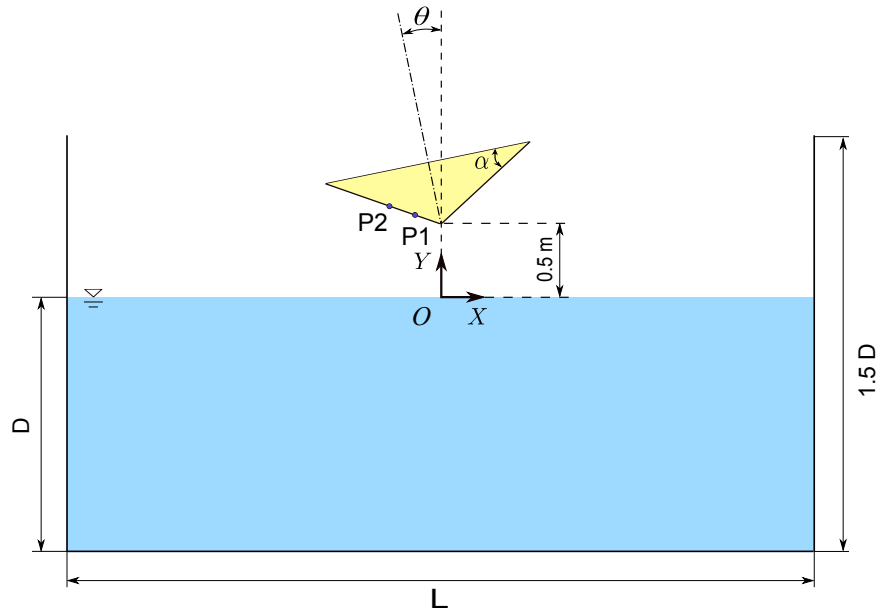


Figure 5.2: Computational domain for water entry of the wedge

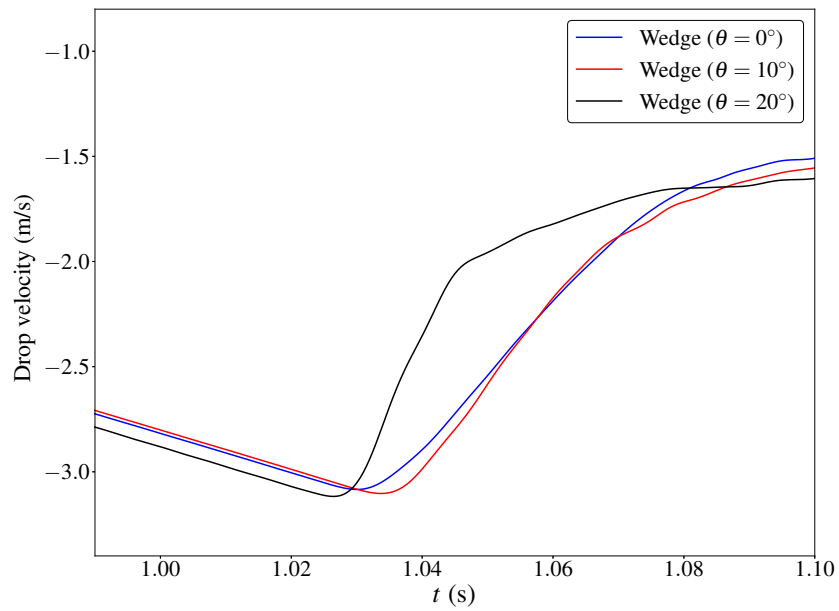


Figure 5.3: Drop velocities for the wedge with different tilt angles

Convergence studies in terms of domain size, total number of particles, particle spacing and time step were carried out for each water entry condition. A summary of convergence study cases is given in Table 5.1.

5.1.1 2-D Wedge with Tilt Angle of $\theta = 0^\circ$

As shown in Table 5.1, the sensitivity of numerical solution to the domain size was examined by using three domain widths and three domain depths. Time histories of the predicted pressures at P1 and P2 and the force at F are presented in Fig. 5.4. It can be seen that the numerical solutions converged as the domain size was increased. The domain width and depth, L and D , were subsequently set as 3.0 m and 1.0 m, respectively, in the following simulations.

For the sensitivity of numerical solution to particle spacing, four sets of particle spacing were investigated. The time step for these four cases was kept as $\Delta t = 1.5 \times 10^{-4}$ s. Figure 5.5 presents time histories of pressures at P1 and P2 and the force at F. It is shown that numerical solutions converged and the pressure fluctuations were suppressed as the particle spacing was reduced. Furthermore, uncertainties due to spatial resolution by the present MPS method were evaluated. The results of PCI and the intermediate details are presented in Table 5.2. It can be seen that uncertainties due to spatial resolution are small. Therefore, the particle spacing of $l_0 = 2.72 \times 10^{-3}$ m was employed in the following studies.

In terms of convergence to time step, three time steps were used (see cases in Table 5.1). The total number of particles for each case was kept as 414,108. Time histories of pressures at P1 and P2 and force at F are presented in Fig. 5.6. It can

Table 5.1: Case matrix of convergence studies for the 2-D wedge

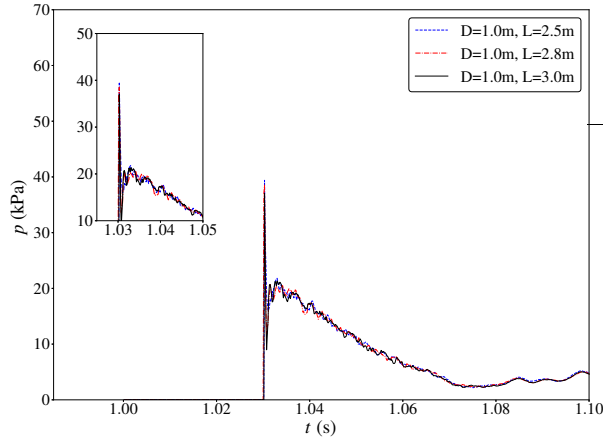
Tilt angle	Domain size		Total number	Particle spacing	Time step
θ	L (m)	D (m)	of particles	l_0 (m)	Δt (s)
0°	2.5	1.0	184,066	3.75×10^{-3}	1.5×10^{-4}
	2.8	1.0	205,746	3.75×10^{-3}	1.5×10^{-4}
	3.0	0.8	177,428	3.75×10^{-3}	1.5×10^{-4}
	3.0	0.9	199,308	3.75×10^{-3}	1.5×10^{-4}
	3.0	1.0	221,188	3.75×10^{-3}	1.5×10^{-4}
	3.0	1.0	57,534	7.48×10^{-3}	1.5×10^{-4}
	3.0	1.0	113,122	5.29×10^{-3}	1.5×10^{-4}
	3.0	1.0	414,108	2.72×10^{-3}	1.5×10^{-4}
	3.0	1.0	414,108	2.72×10^{-3}	2.0×10^{-4}
	3.0	1.0	414,108	2.72×10^{-3}	1.0×10^{-4}
10°	2.5	1.0	184,066	3.75×10^{-3}	1.5×10^{-4}
	2.8	1.0	205,746	3.75×10^{-3}	1.5×10^{-4}
	3.0	0.8	177,428	3.75×10^{-3}	1.5×10^{-4}
	3.0	0.9	199,308	3.75×10^{-3}	1.5×10^{-4}
	3.0	1.0	221,188	3.75×10^{-3}	1.5×10^{-4}
	3.0	1.0	57,534	7.48×10^{-3}	1.5×10^{-4}
	3.0	1.0	113,122	5.29×10^{-3}	1.5×10^{-4}
	3.0	1.0	437,460	2.65×10^{-3}	1.5×10^{-4}
	3.0	1.0	437,460	2.65×10^{-3}	2.0×10^{-4}
	3.0	1.0	437,460	2.65×10^{-3}	1.0×10^{-4}
20°	3.0	1.0	221,612	3.75×10^{-3}	1.5×10^{-4}
	4.0	1.0	292,890	3.75×10^{-3}	1.5×10^{-4}
	5.0	0.8	293,740	3.75×10^{-3}	1.5×10^{-4}
	5.0	0.9	328,684	3.75×10^{-3}	1.5×10^{-4}
	5.0	1.0	364,544	3.75×10^{-3}	1.5×10^{-4}
	5.0	1.0	92,224	7.56×10^{-3}	1.5×10^{-4}
	5.0	1.0	207,708	5.00×10^{-3}	1.5×10^{-4}
	5.0	1.0	687,156	2.72×10^{-3}	1.5×10^{-4}
	5.0	1.0	687,156	2.72×10^{-3}	2.1×10^{-4}
	5.0	1.0	687,156	2.72×10^{-3}	1.0×10^{-4}

be observed that the pressures/force converged as the time step was decreased. The time step, $\Delta t = 1.0 \times 10^{-4}$ s, was then adopted.

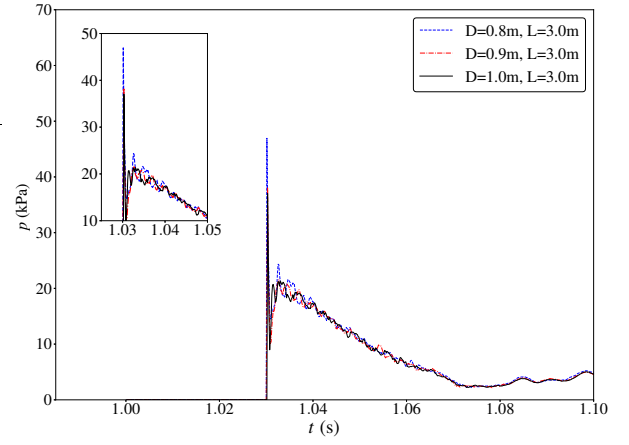
The results given below were obtained using a particle spacing of 2.72×10^{-3} m and a time step of $\Delta t = 1.0 \times 10^{-4}$ s. Time histories of pressures at P1 and P2 and force at F are presented in Fig. 5.7. They are also compared with the experimental data by KRISO [26]), the numerical results obtained using the first-order gradient model in symmetrical form proposed by Lee et. al [89], and those by the original higher-order gradient model by Khayyer and Gotoh [77]. For both pressures and force, oscillations are suppressed by the present model. The peak values are compared in Table 5.3 as well as their relative errors in comparison with the experimental data. The local pressure at P2 for $\theta = 0^\circ$ was over-predicted in comparison with the experimental data ([26]). The errors were reduced by applying the present method with the higher-order gradient model in symmetrical form. However, the predicted pressures and load after the peak were slightly higher than the experimental data, which is likely caused by the fact that the air phase and the surface roughness of the wedge were neglected in the present numerical model. The pressure fields are also compared in Fig. 5.8. The noise in the contour by using the first-order gradient model can be observed, and the higher-order model improved the solution. In summary, the present higher-order method with the improved gradient model led to improved predictions of pressures and force.

Table 5.2: Uncertainties in predicted peak pressures and force for the wedge with $\theta = 0^\circ$

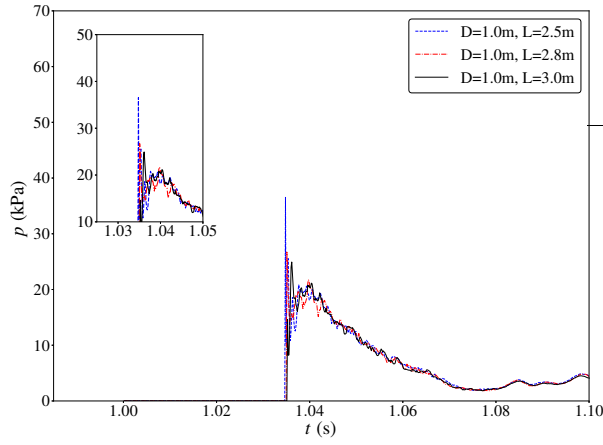
	Peak pressure at P1	Peak pressure at P2	Peak force at F
h_1	2.72×10^{-3}	2.72×10^{-3}	2.72×10^{-3}
h_2	3.75×10^{-3}	3.75×10^{-3}	3.75×10^{-3}
h_3	7.48×10^{-3}	7.48×10^{-3}	7.48×10^{-3}
ϕ_1	35.53	25.18	55.37
ϕ_2	37.04	24.93	50.32
ϕ_3	44.48	33.54	68.40
p	3.40	8.13	3.05
ϕ_{ext}^{21}	34.78	25.20	58.39
e_a^{21}	4.24%	0.98%	9.11%
e_{ext}^{21}	2.18%	0.08%	5.19%
PCI _{fine} ²¹	2.67%	0.10%	6.84%



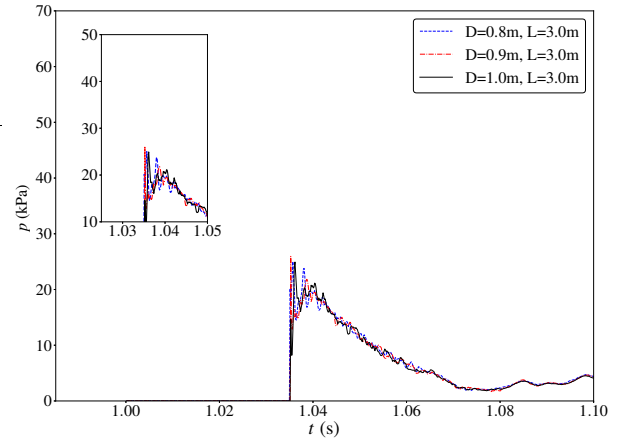
(a) Pressures at P1 with different domain widths



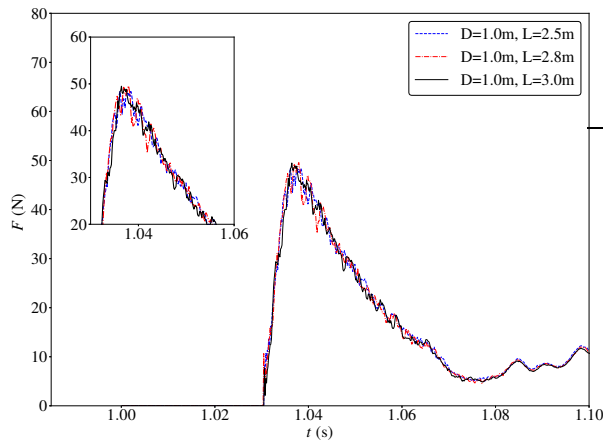
(b) Pressures at P1 with different domain depths



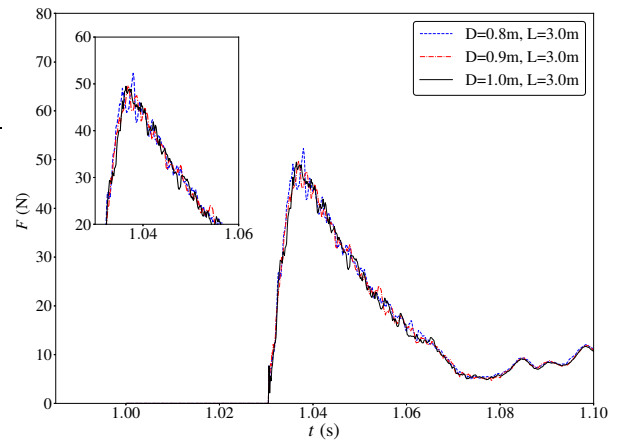
(c) Pressures at P2 with different domain widths



(d) Pressures at P2 with different domain depths

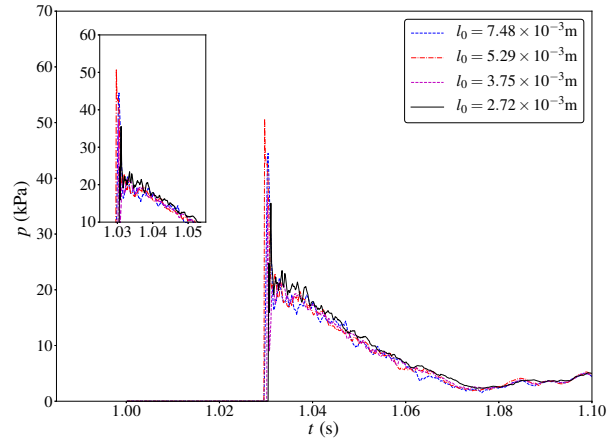


(e) Force at F with different domain widths

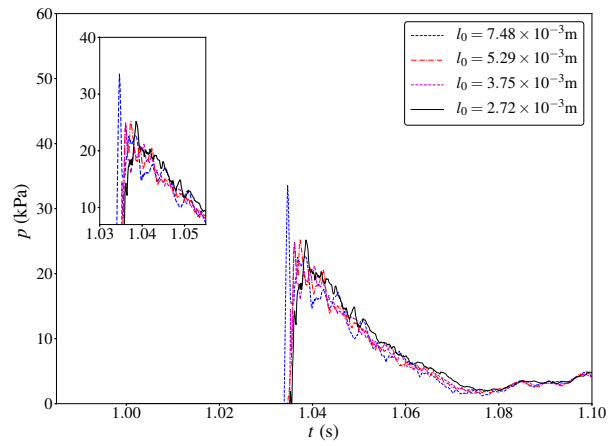


(f) Force at F with different domain depths

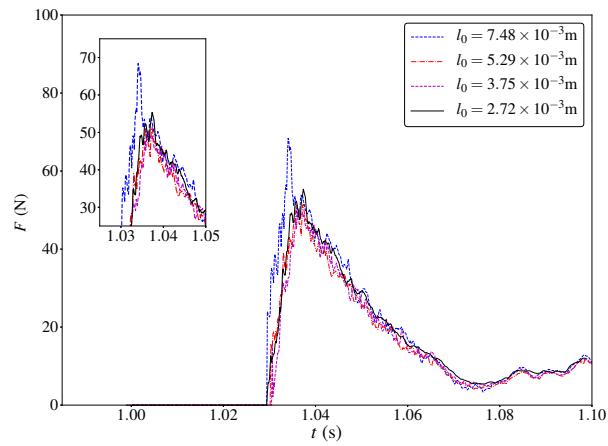
Figure 5.4: Sensitivity of pressures and force to domain size for the wedge with $\theta = 0^\circ$



(a) Spatial convergence of pressure at P1

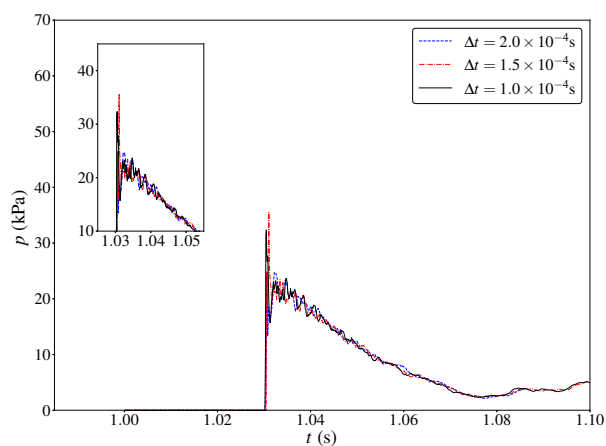


(b) Spatial convergence of pressure at P2

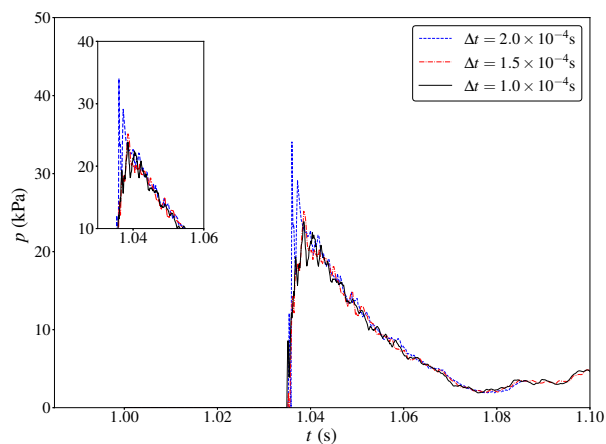


(c) Spatial convergence of force at F

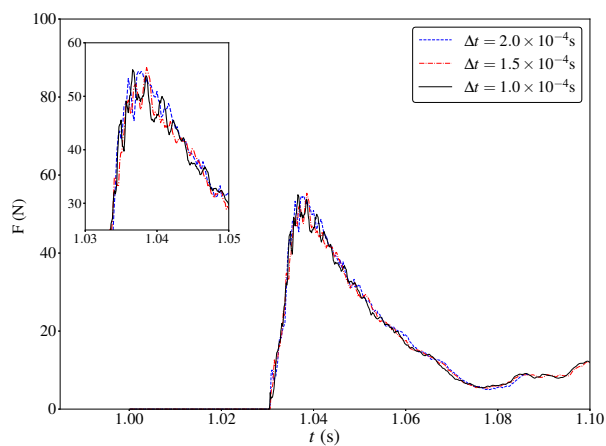
Figure 5.5: Spatial convergence of pressures and force for the wedge with $\theta = 0^\circ$



(a) Temporal convergence of pressure at P1

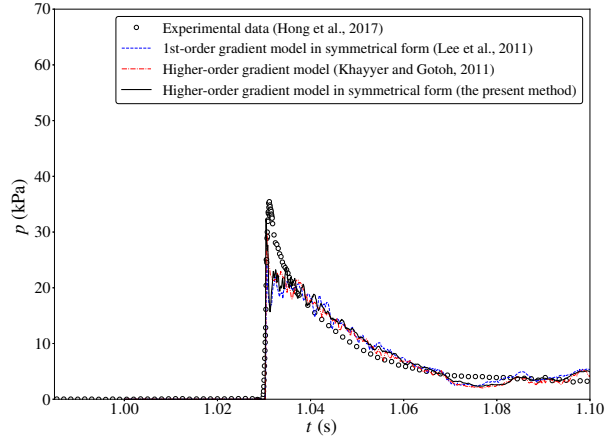


(b) Temporal convergence of pressure at P2

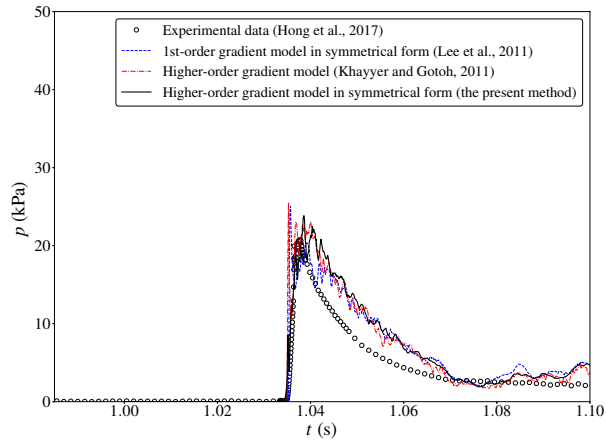


(c) Temporal convergence of force at F

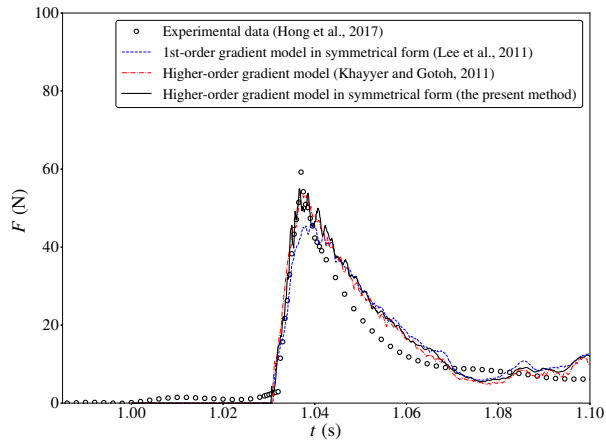
Figure 5.6: Temporal convergence of pressures and force for the wedge with $\theta = 0^\circ$



(a) Comparison of pressure at P1



(b) Comparison of pressure at P2

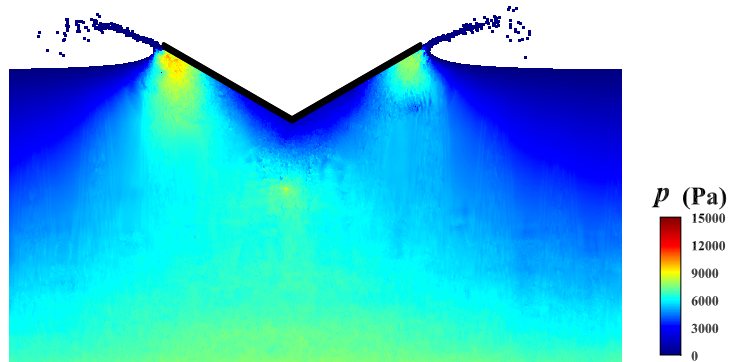


(c) Comparison of force at F

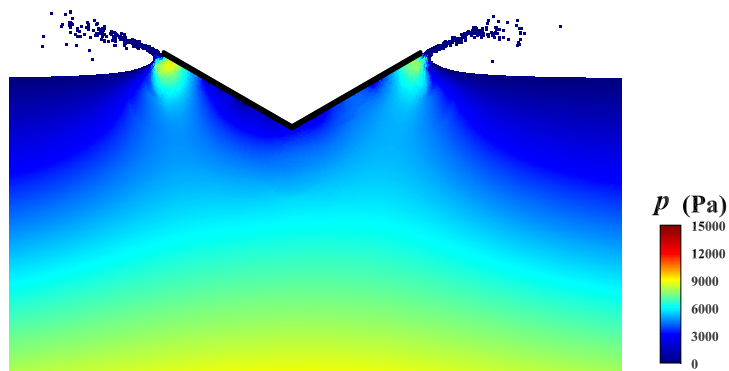
Figure 5.7: Comparison of pressures and force for the wedge with $\theta = 0^\circ$

Table 5.3: Results for the 2-D wedge with $\theta = 0^\circ$

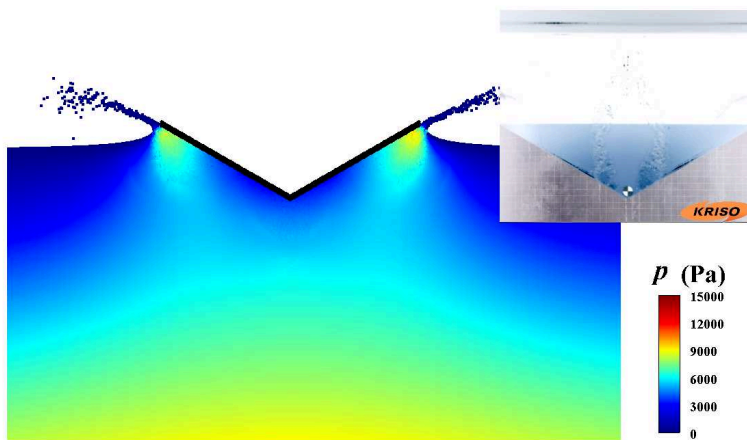
Methods	Peak pressure		Peak pressure		Peak force	
	P1 (kPa)	Error	P2 (kPa)	Error	F (N)	Error
Experimental data [26]	35.45	-	20.73	-	59.21	-
First-order gradient model [89]	24.12	31.97%	25.06	20.86%	46.17	22.04%
Higher-order gradient model [77]	29.85	15.80%	25.55	23.22%	54.01	8.80%
The present method	32.35	8.75%	23.84	15.01%	54.98	7.16%



(a) First-order gradient model [89]



(b) Higher-order gradient model [77]



(c) The present method and the comparison with experimental snapshot [26]

Figure 5.8: Comparison of pressure fields for the wedge with $\theta = 0^\circ$

5.1.2 2-D Wedge with Tilt Angle of $\theta = 10^\circ$

Time histories of pressures at P1 and P2 and force at F are presented in Fig. 5.9 for different domain sizes. Results were converged as the domain size was increased. The domain width and depth, $L = 3.0$ m and $D = 1.0$ m, which are the same as those for the wedge with the tilt angle of $\theta = 10^\circ$, were adopted in the following simulations.

Similarly, four sets of particles as shown in Table 5.1 were used in convergence studies with the time step of $\Delta t = 1.5 \times 10^{-4}$ s. As shown in Fig. 5.10, numerical solutions converged as the particle spacing was decreased. Uncertainties in predicted peak pressures and force with respect to particle spacing were presented in Table 5.4 and they are less than 5.0%. Therefore, the particle spacing of $l_0 = 2.65 \times 10^{-3}$ m was employed in the following studies.

Three time steps as listed in Table 5.1 were used to examine the sensitivity of solution to time step. The total number of particles for each case was kept as 437,460. Time histories of pressures at P1 and P2 and force at F are presented in Fig. 5.11. It can be observed that the numerical solutions converged as the time step was decreased. The smallest time step, $\Delta t = 1.0 \times 10^{-4}$ s, was therefore adopted.

The results given below were based on the particle spacing of 2.65×10^{-3} m and the time step of $\Delta t = 1.0 \times 10^{-4}$ s. Time histories of pressures at P1 and P2 and the impact force at F are presented in Fig. 5.12. For both pressures and force, oscillations were suppressed by using the present method with the higher-order pressure gradient model in symmetrical form. The peak values and their relative errors in comparison with the experimental data are compared in Table 5.5. Errors were reduced by the present higher-order model. The pressure fields are compared in Fig. 5.13. The noise

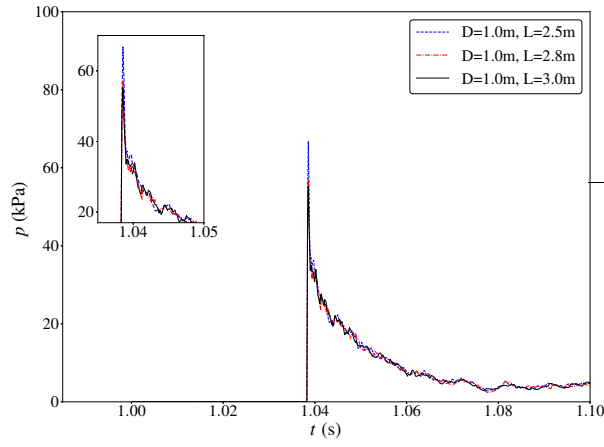
Table 5.4: Uncertainties in predicted peak pressures and force for the wedge with $\theta = 10^\circ$

	Peak pressure at P1	Peak pressure at P2	Peak force at F
h_1	2.65×10^{-3}	2.65×10^{-3}	2.65×10^{-3}
h_2	3.75×10^{-3}	3.75×10^{-3}	3.75×10^{-3}
h_3	7.48×10^{-3}	7.48×10^{-3}	7.48×10^{-3}
ϕ_1	48.90	40.07	77.14
ϕ_2	52.74	40.60	74.78
ϕ_3	75.47	55.27	101.25
p	3.63	7.04	5.28
ϕ_{ext}^{21}	47.38	40.02	77.59
e_a^{21}	7.86%	1.33%	3.05%
e_{ext}^{21}	3.22%	0.13%	0.58%
$\text{PCI}_{\text{fine}}^{21}$	3.90%	0.16%	0.73%

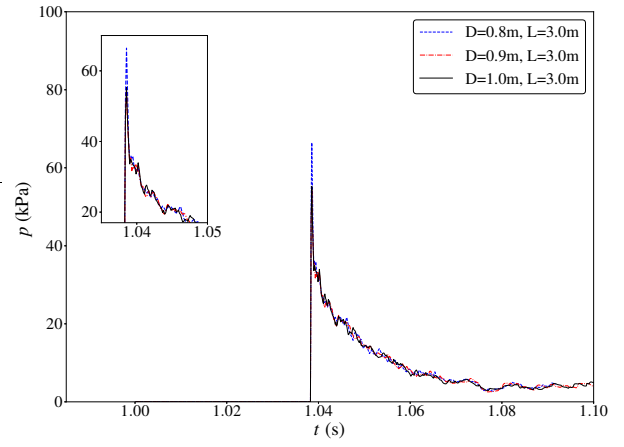
in the pressure field was suppressed by employing the higher-order gradient model. Therefore, the predictions of pressures and force for the asymmetric water entry of the wedge were generally improved.

Table 5.5: Results for the 2-D wedge with $\theta = 10^\circ$

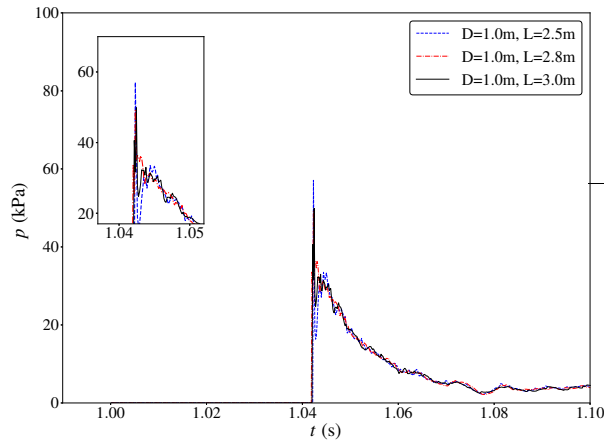
Methods	Peak pressure		Peak pressure		Peak force	
	P1 (kPa)	Error	P2 (kPa)	Error	F (N)	Error
Experimental data [26]	50.69	-	41.56	-	87.52	-
First-order gradient model [89]	56.30	11.06%	63.62	53.09%	69.39	20.72%
Higher-order gradient model [77]	58.76	15.92%	51.33	23.52%	84.39	3.58%
The present method	46.41	8.45%	42.15	1.43%	80.85	7.62%



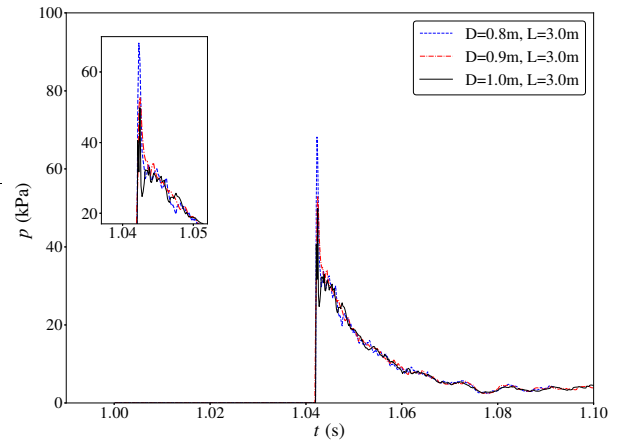
(a) Pressures at P1 with different domain widths



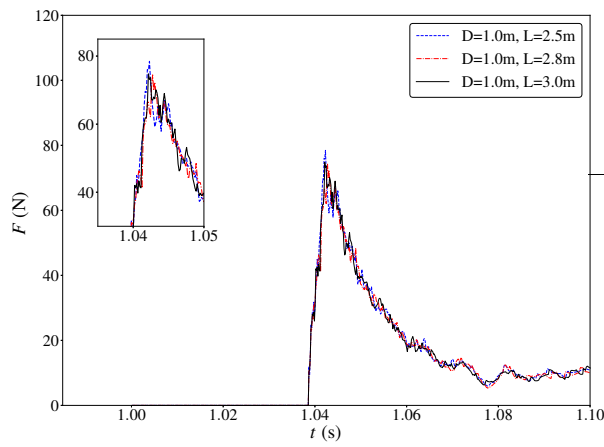
(b) Pressures at P1 with different domain depths



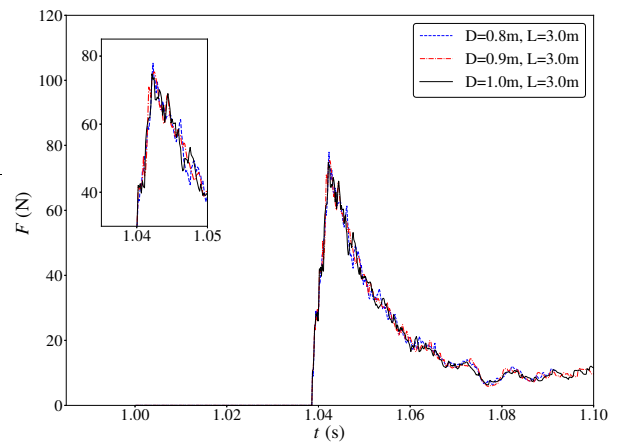
(c) Pressures at P2 with different domain widths



(d) Pressures at P2 with different domain depths

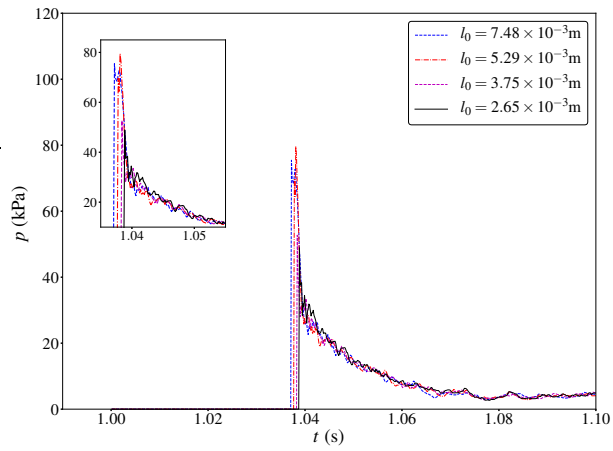


(e) Force at F with different domain widths

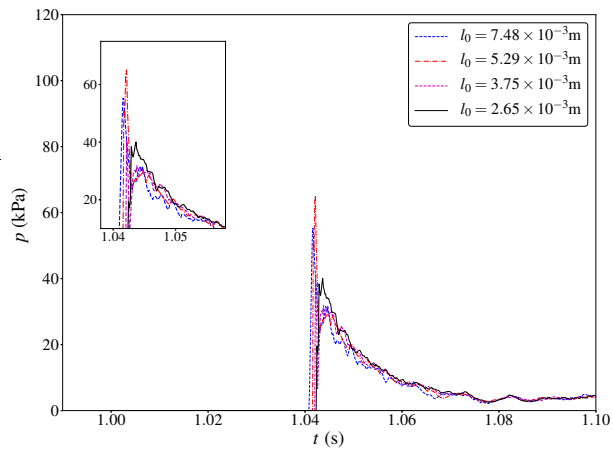


(f) Force at F with different domain depths

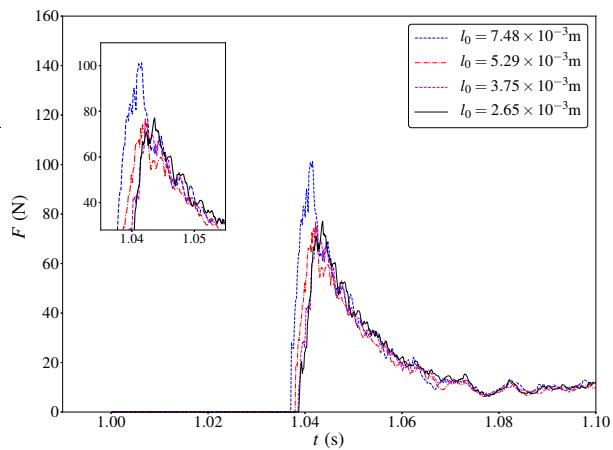
Figure 5.9: Sensitivity of pressures and force to domain size for the wedge with $\theta = 10^\circ$



(a) Spatial convergence of pressure at P1

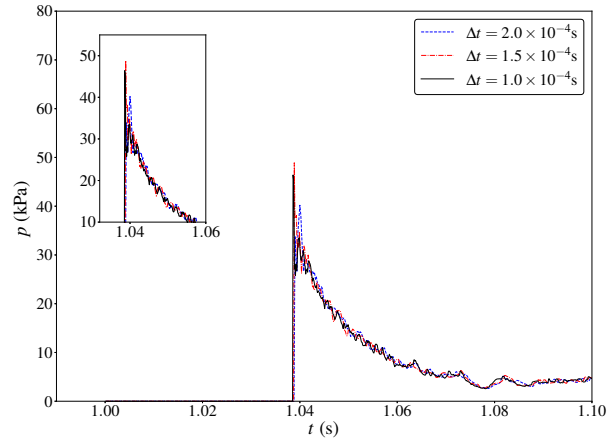


(b) Spatial convergence of pressure at P2

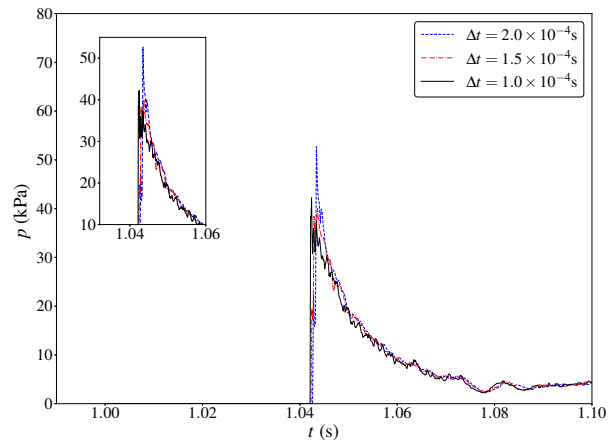


(c) Spatial convergence of force at F

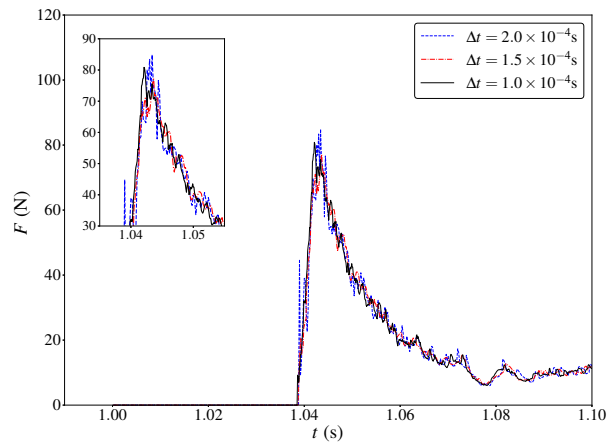
Figure 5.10: Spatial convergence of pressures and force for the wedge with $\theta = 10^\circ$



(a) Temporal convergence of pressure at P1

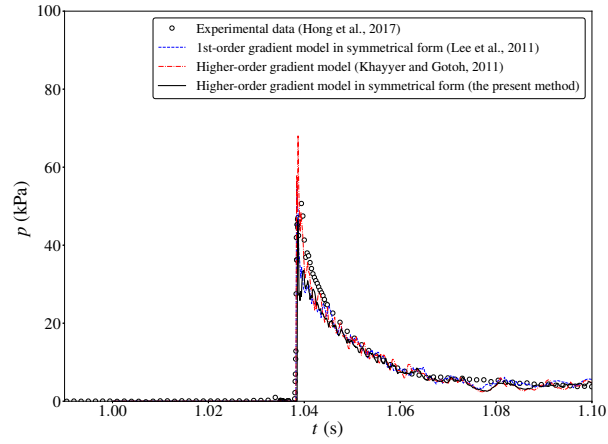


(b) Temporal convergence of pressure at P2

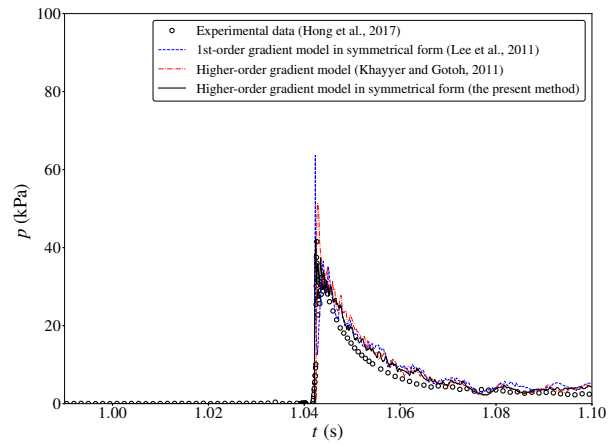


(c) Temporal convergence of force at F

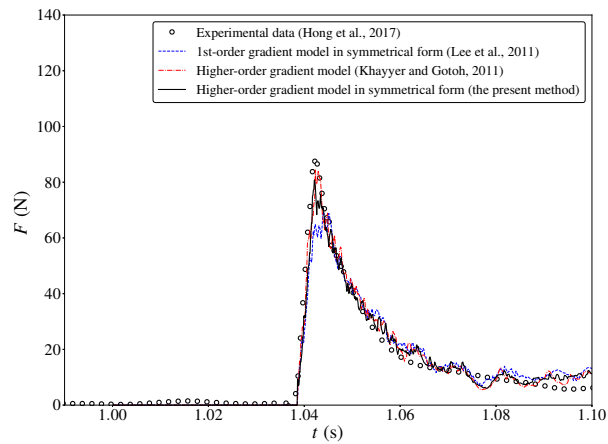
Figure 5.11: Temporal convergence of pressures and force for the wedge with $\theta = 10^\circ$



(a) Comparison of pressure at P1

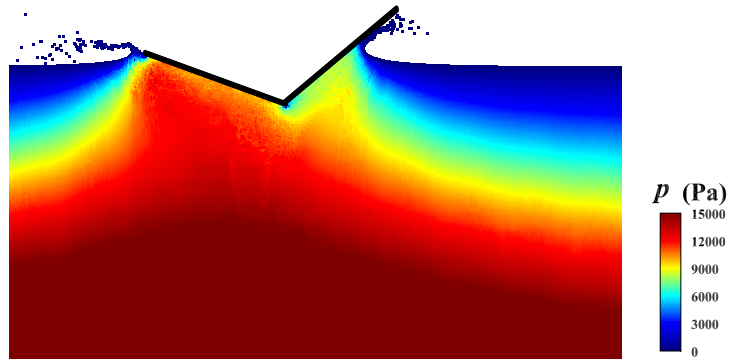


(b) Comparison of pressure at P2

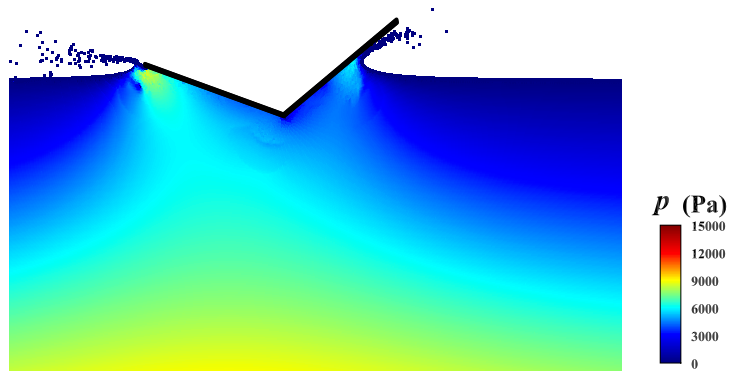


(c) Comparison of force at F

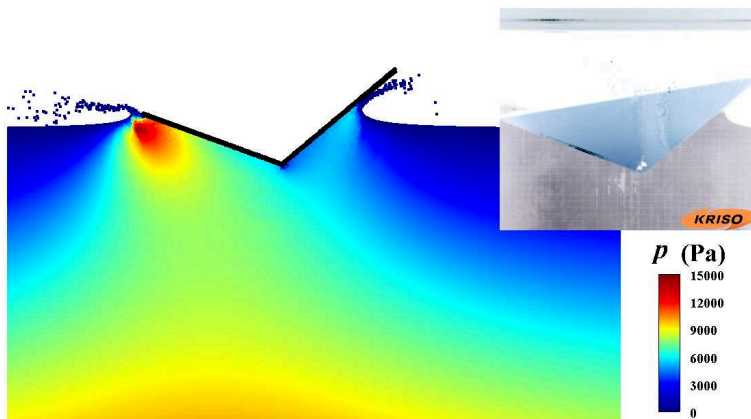
Figure 5.12: Comparison of pressures and force for the wedge with $\theta = 10^\circ$



(a) First-order gradient model [89]



(b) Higher-order gradient model [77]



(c) The present method and the comparison with experimental snapshot [26]

Figure 5.13: Comparison of pressure fields for the wedge with $\theta = 10^\circ$

5.1.3 2-D Wedge with Tilt Angle of $\theta = 20^\circ$

The water entry of the wedge with a larger tilt angle $\theta = 20^\circ$ was also studied. As presented in Table 5.1, domain investigation involved three widths and three depths. Time histories of pressures and force are presented in Fig. 5.14. As expected, results converged as the domain size was increased. For a larger tilt angle, L and D of the chosen domain were 5.0 m and 1.0 m, respectively. The domain width was larger than those for wedges with smaller tilt angles.

As for convergence studies on the particle spacing, Table 5.1 lists four sets of particle spacings with a constant time step of $\Delta t = 1.5 \times 10^{-4}$ s. Time histories of pressures and force are shown in Fig. 5.10. The convergence can be observed. The corresponding uncertainty levels with respect to particle spacing are summarized in Table 5.6 with values less than 5%. The smallest particle spacing of $l_0 = 2.72 \times 10^{-3}$ m was chosen in the following studies.

For the convergence studies on the time step, three time steps were used as presented in Table 5.1. The predicted time histories of pressures at P1 and P2 and force at F are presented in Fig. 5.16. It can be observed that the numerical solutions converged as the time step was decreased. The time step, $\Delta t = 1.0 \times 10^{-4}$ s, was therefore adopted.

The results given below were based on a particle spacing of 2.72×10^{-3} m and a time step of $\Delta t = 1.0 \times 10^{-4}$ s. The comparison of pressures at P1 and P2 and the impact load at F are presented in Fig. 5.12. Oscillations in time histories of predicted pressures and force were suppressed by the present method. The peak values and associated errors in comparison with experimental results were presented

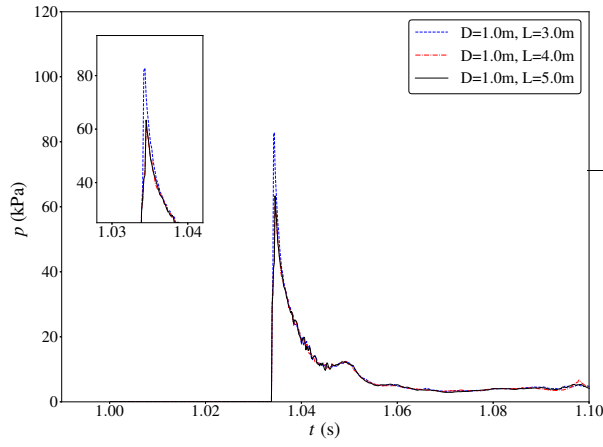
Table 5.6: Uncertainties in predicted peak pressures and force for the wedge with $\theta = 20^\circ$

	Peak pressure at P1	Peak pressure at P2	Peak force at F
h_1	2.72×10^{-3}	2.72×10^{-3}	2.72×10^{-3}
h_2	3.75×10^{-3}	3.75×10^{-3}	3.75×10^{-3}
h_3	7.56×10^{-3}	7.56×10^{-3}	7.56×10^{-3}
ϕ_1	68.82	71.00	147.91
ϕ_2	63.37	66.43	134.92
ϕ_3	88.18	108.37	220.59
p	3.56	5.11	4.38
ϕ_{ext}^{21}	71.36	72.10	152.12
e_a^{21}	7.92%	6.44%	8.78%
e_{ext}^{21}	3.57%	1.52%	2.77%
$\text{PCI}_{\text{fine}}^{21}$	4.62%	1.93%	3.56%

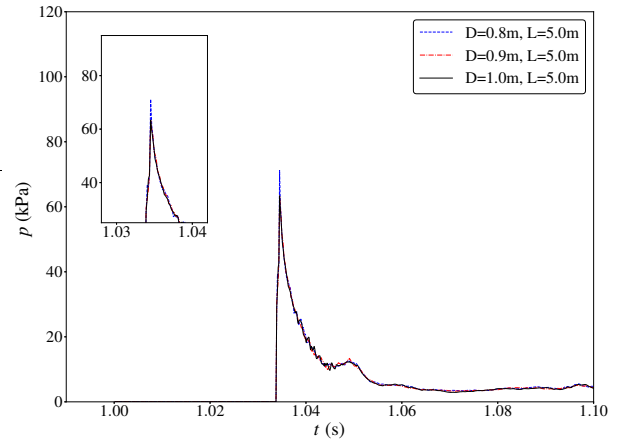
in Table 5.7. The pressure fields are further compared in Fig. 5.18. Comparing with other methods, the present higher-order model shows improvement.

Table 5.7: Results for the 2-D wedge with $\theta = 20^\circ$

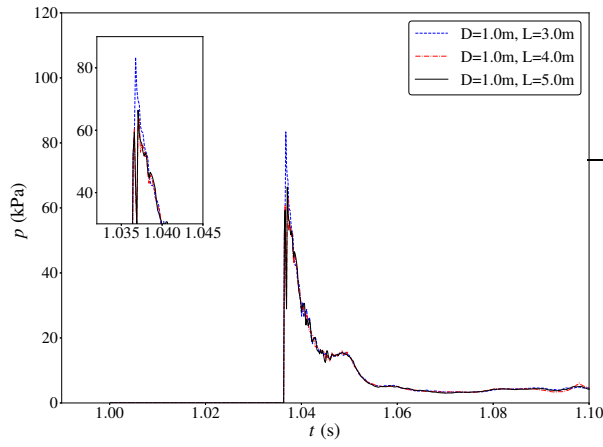
Methods	Peak pressure		Peak pressure		Peak force	
	P1 (kPa)	Error	P2 (kPa)	Error	F (N)	Error
Experimental data [26]	70.09	-	62.65	-	160.37	-
First-order gradient model [89]	56.30	19.67%	63.62	1.54%	132.82	17.18%
Higher-order gradient model [77]	58.76	16.16%	51.33	18.07%	138.27	13.78%
The present method	68.10	2.83%	66.49	6.12%	148.45	7.43%



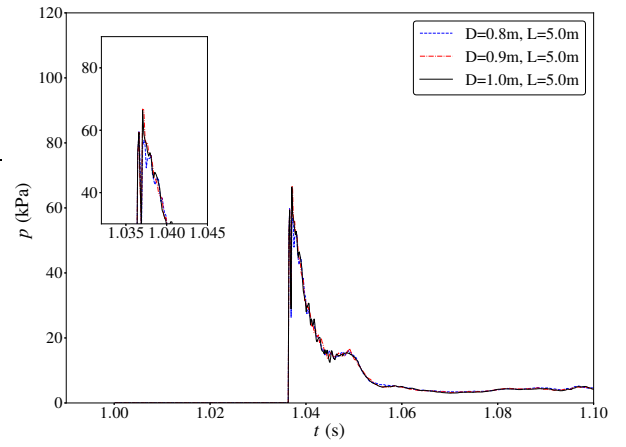
(a) Pressures at P1 with different domain widths



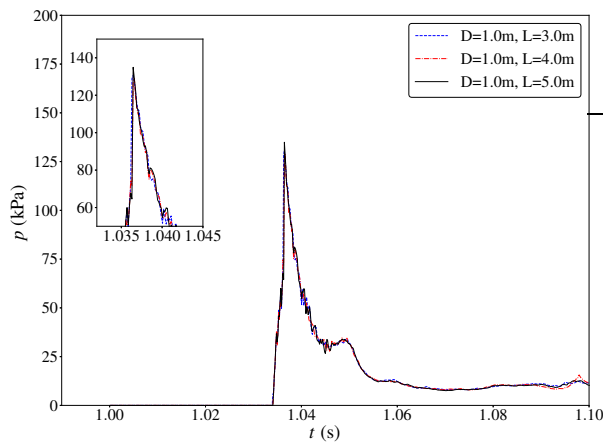
(b) Pressures at P1 with different domain depths



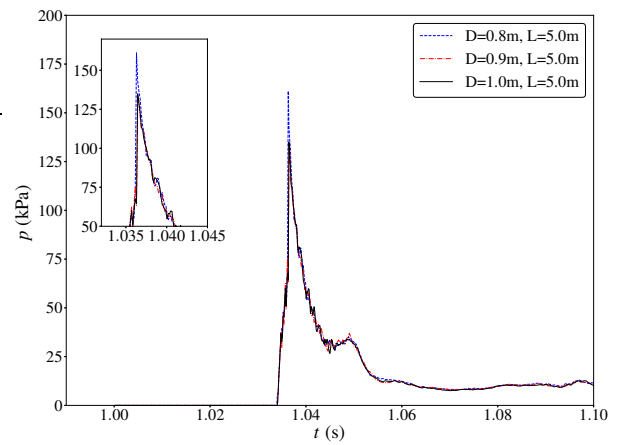
(c) Pressures at P2 with different domain widths



(d) Pressures at P2 with different domain depths



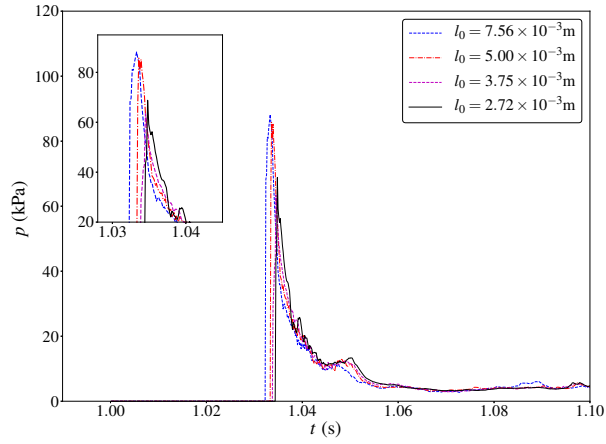
(e) Force at F with different domain widths



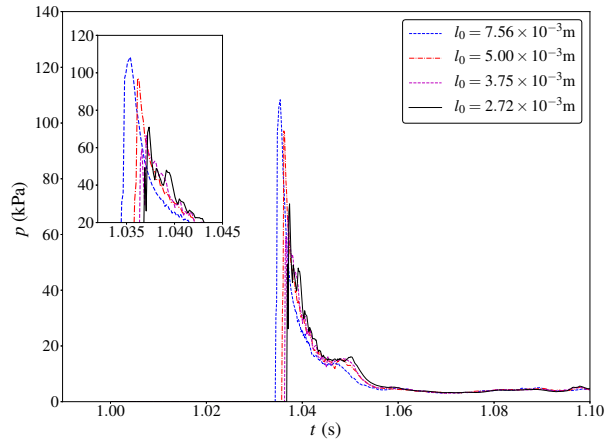
(f) Force at F with different domain depths

Figure 5.14: Sensitivity of pressures and force to domain size for the wedge with

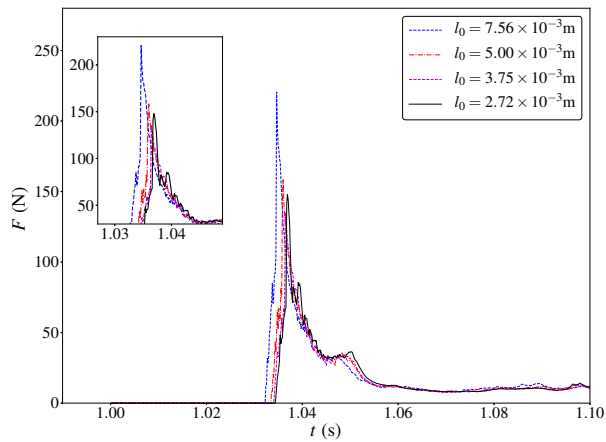
$\theta = 20^\circ$



(a) Spatial convergence of pressure at P1

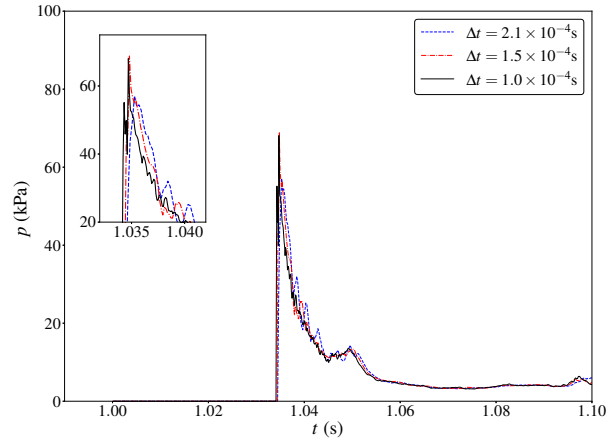


(b) Spatial convergence of pressure at P2

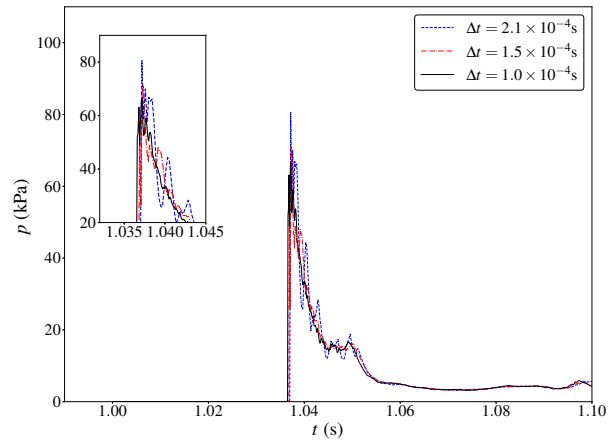


(c) Spatial convergence of force at F

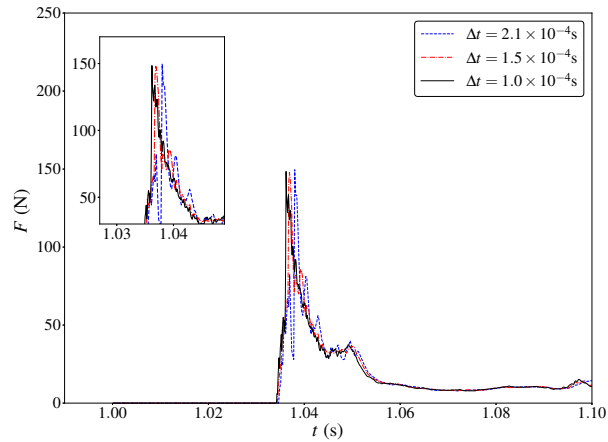
Figure 5.15: Spatial convergence of pressures and force for the wedge with $\theta = 20^\circ$



(a) Temporal convergence of pressure at P1

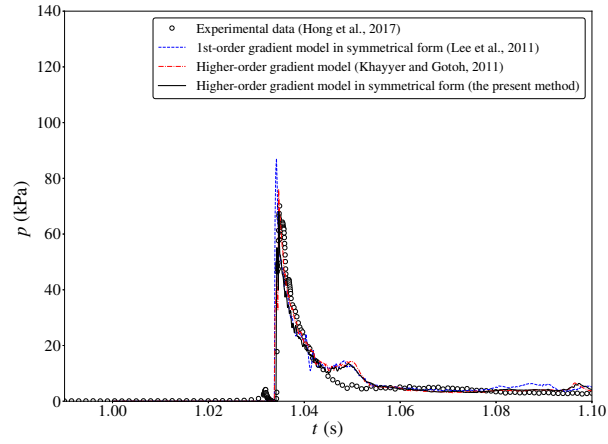


(b) Temporal convergence of pressure at P2

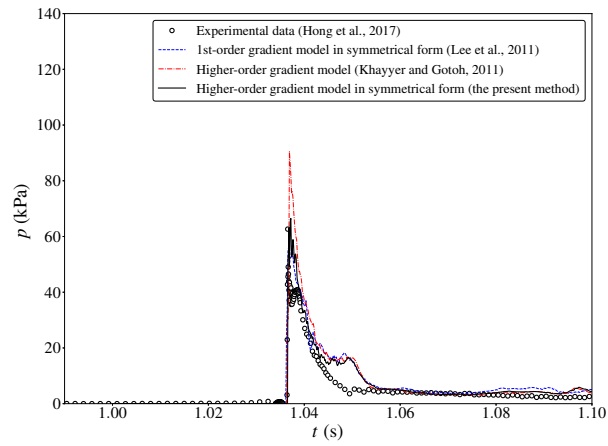


(c) Temporal convergence of force at F

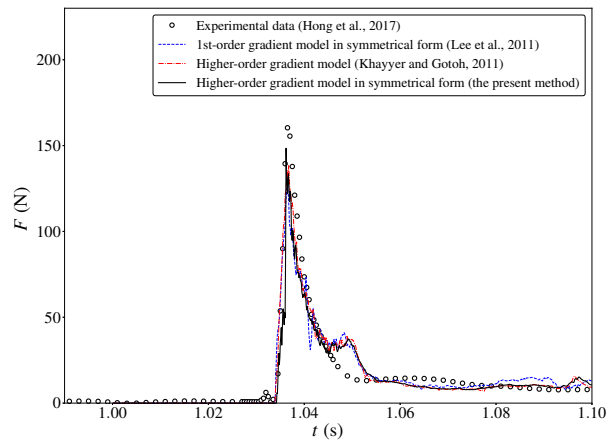
Figure 5.16: Temporal convergence of pressures and force for the wedge with $\theta = 20^\circ$



(a) Comparison of pressure at P1

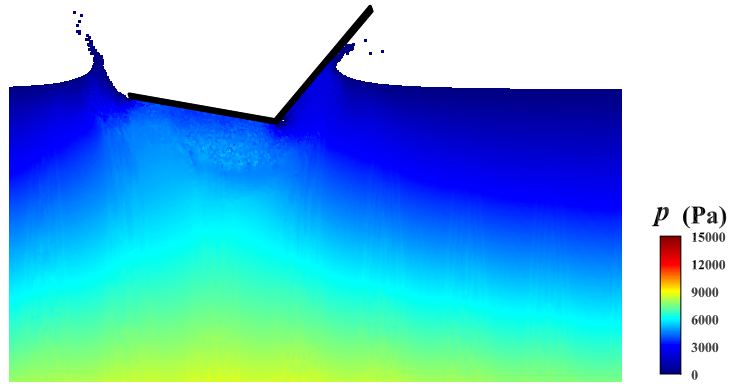


(b) Comparison of pressure at P2

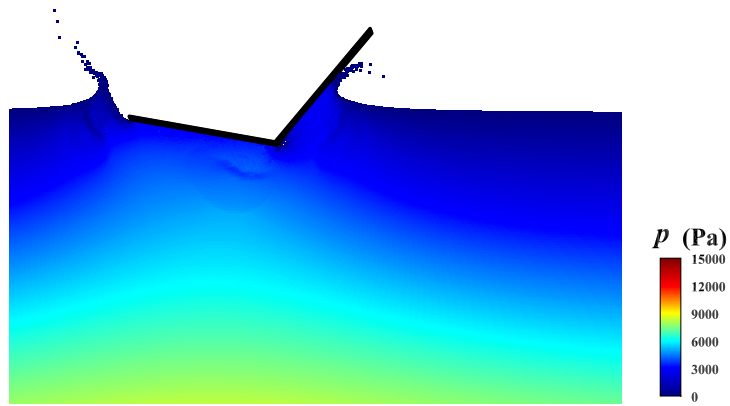


(c) Comparison of force at F

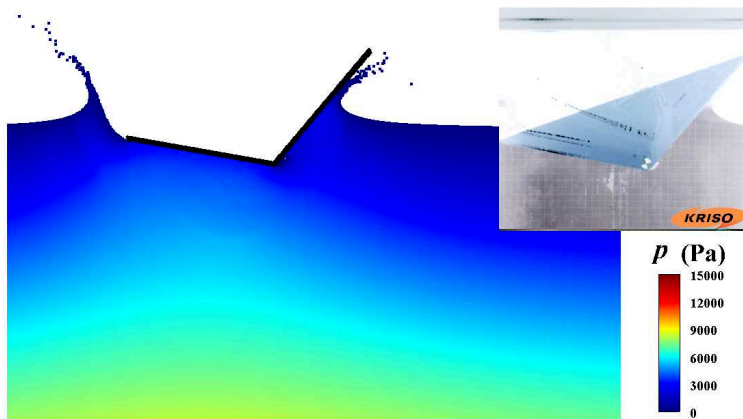
Figure 5.17: Comparison of pressures and force for the wedge with $\theta = 20^\circ$



(a) First-order gradient model [89]



(b) Higher-order gradient model [77]



(c) The present method and the comparison with experimental snapshot [26]

Figure 5.18: Comparison of pressure fields for the wedge with $\theta = 20^\circ$

5.2 2-D Ship Sections

Validation studies were further carried out for 2-D ship sections (Model A and Model B) tested by KRISO (Hong et al. (2017) [26]). The drop height was $h = 0.3$ m. Figure 5.19 shows the locations of three pressure sensors, P1, P2 and P3, and those of three load cells, F1, F2 and F3. The radius of each load cell was 50 mm. The computational domain and the initial settings of 2-D simulations are presented in Fig. 5.20. The prescribed drop velocities measured in the experiments are given in Fig. 5.21. Convergence studies on the domain size, the particle spacing, and the time step were carried out in a similar way to the wedge. Table 5.8 summarized the parameters in convergence studies for ship sections, Model A and Model B.

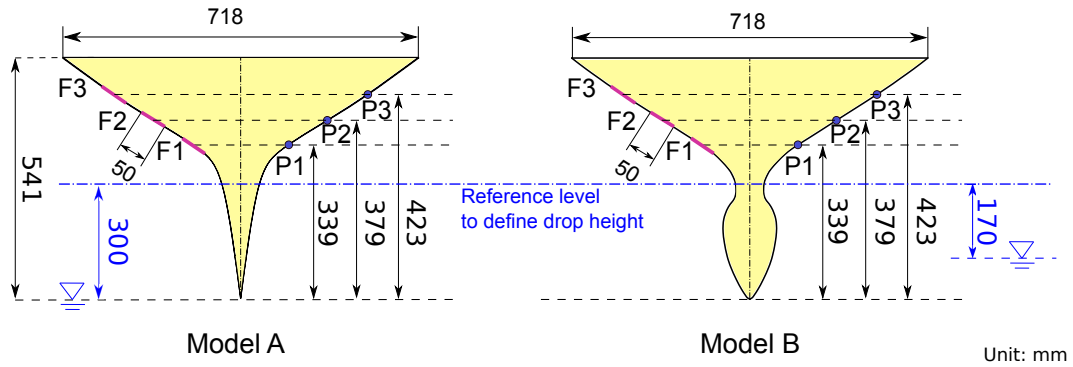
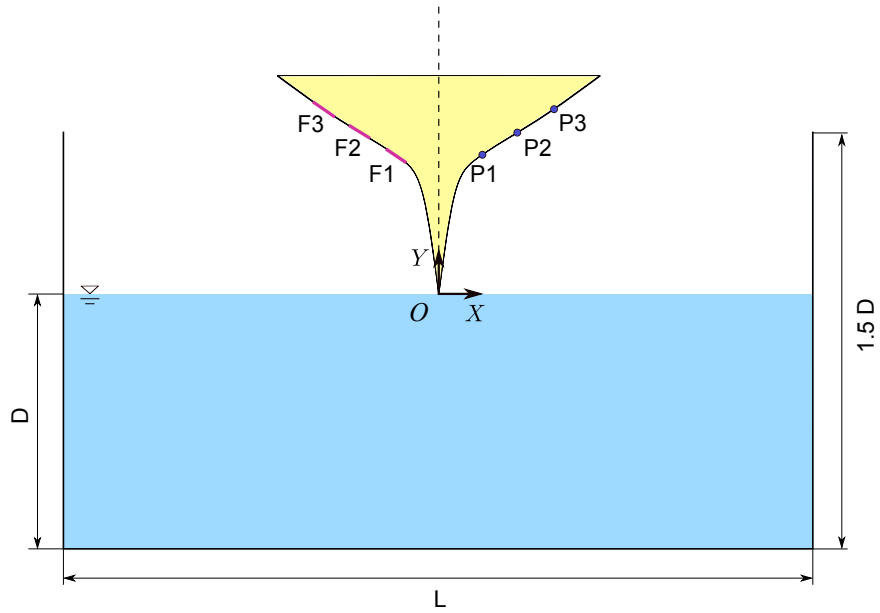


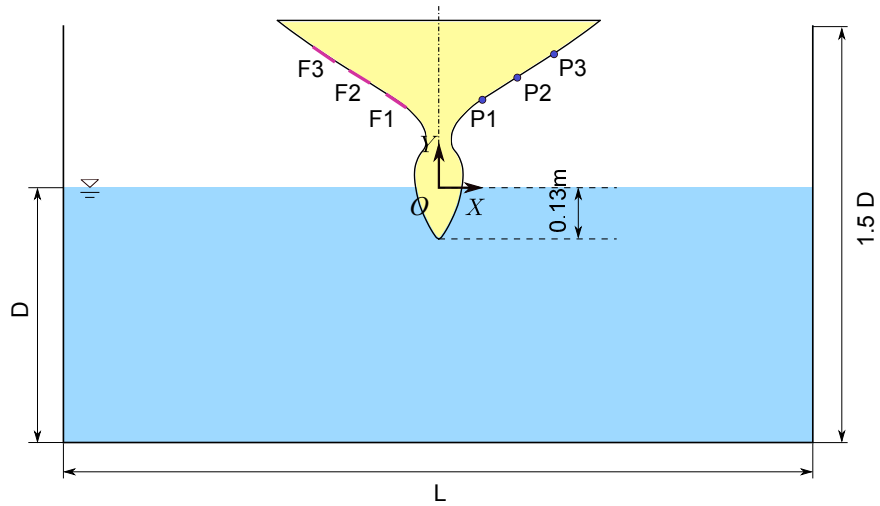
Figure 5.19: Sensors on the ship sections

5.2.1 2-D Ship Section (Model A)

For studies on domain size, the particle spacing was kept the same as $l_0 = 3.75 \times 10^{-3}$ m and the corresponding time step was set as $\Delta t = 1.5 \times 10^{-4}$ s. The predicted



(a) Model A



(b) Model B

Figure 5.20: Computational domains for the water entry of the ship sections

pressures at P1, P2, P3 and the predicted forces at F1, F2, F3 for Model A are shown in Fig. 5.22 and Fig. 5.23, respectively. It can be seen that numerical solutions converged as the domain size was increased. In the following studies, the domain

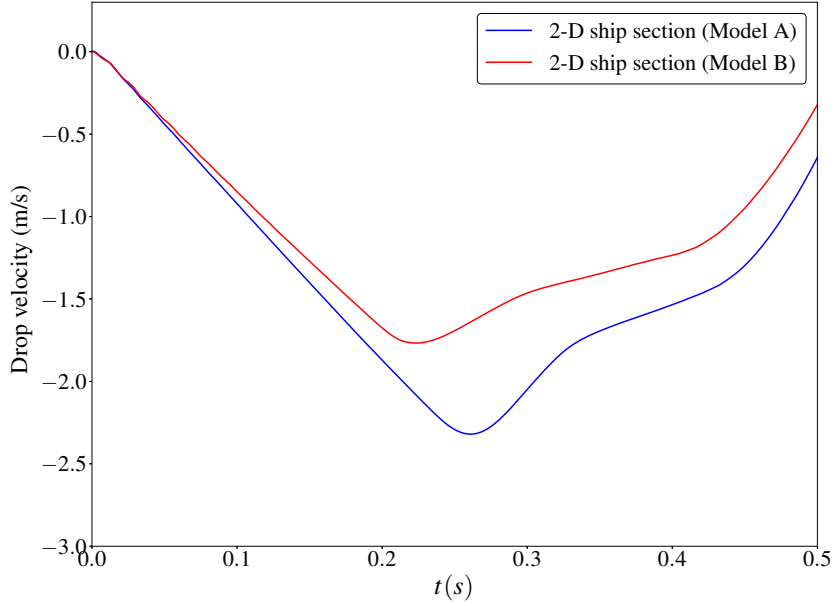


Figure 5.21: Drop velocities for the water entry of the ship sections

width and depth were chosen as $L = 3.0$ m and $D = 1.0$ m, respectively.

The sensitivities of numerical solutions to the particle spacing was then examined. Table 5.8 lists four sets of particle spacing with the same time step $\Delta t = 1.5 \times 10^{-4}$ s. Time histories of pressures at P1, P2 and P3 and forces at F1, F2 and F3 for Model A are given in Fig. 5.10. Numerical solutions converged with a decreased particle spacing. Uncertainties due to particle spacing were given in Table 5.9. The largest numerical uncertainty of the results was within 3.0%, and the particle spacing of $l_0 = 2.50 \times 10^{-3}$ m was employed in the following studies.

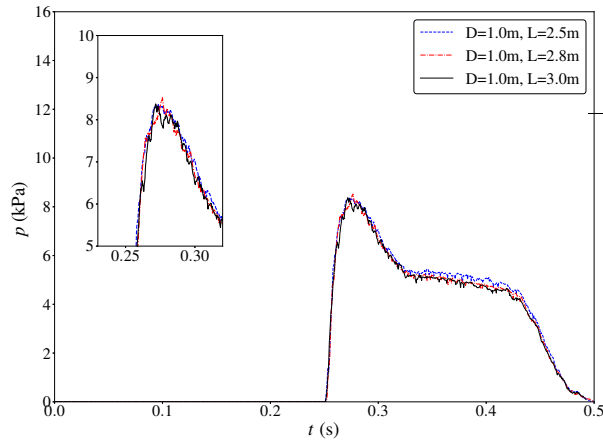
For the sensitivity study on time step, time histories of pressures and forces for Model A are presented in Fig. 5.25 with various time steps shown in Table 5.8. A smaller time step led to converged solution with less oscillations in the time series. The time step, $\Delta t = 1.5 \times 10^{-4}$ s, was chosen for the following simulations.

Table 5.8: Case matrix of convergence studies for the ship sections

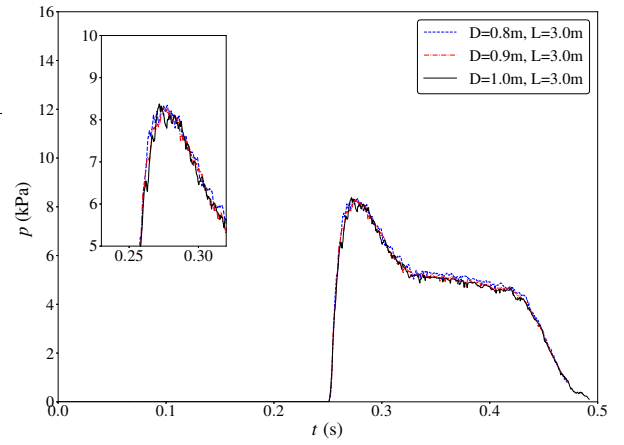
Geometry	Domain size		Total number	Particle spacing	Time step
	L (m)	D (m)	of particles	l_0 (m)	Δt (s)
Ship section (Model A)	2.5	1.0	185,164	3.75×10^{-3}	1.5×10^{-4}
	2.8	1.0	206,844	3.75×10^{-3}	1.5×10^{-4}
	3.0	0.8	178,438	3.75×10^{-3}	1.5×10^{-4}
	3.0	0.9	200,366	3.75×10^{-3}	1.5×10^{-4}
	3.0	1.0	222,286	3.75×10^{-3}	1.5×10^{-4}
	3.0	1.0	57,534	7.48×10^{-3}	1.5×10^{-4}
	3.0	1.0	113,122	5.29×10^{-3}	1.5×10^{-4}
	3.0	1.0	222,286	3.75×10^{-3}	2.1×10^{-4}
	3.0	1.0	222,286	3.75×10^{-3}	3.0×10^{-4}
	3.0	1.0	493,030	2.50×10^{-3}	1.5×10^{-4}
Ship section (Model B)	3.0	1.0	57,440	7.48×10^{-3}	1.5×10^{-4}
	3.0	1.0	112,888	5.29×10^{-3}	1.5×10^{-4}
	3.0	1.0	221,762	3.75×10^{-3}	1.5×10^{-4}
	3.0	1.0	221,762	3.75×10^{-3}	2.1×10^{-4}
	3.0	1.0	221,762	3.75×10^{-3}	3.0×10^{-4}
	3.0	1.0	437,894	2.65×10^{-3}	1.5×10^{-4}

Based on a particle spacing of 2.50×10^{-3} m and a time step of $\Delta t = 1.5 \times 10^{-4}$ s, time histories of the numerical solutions are presented in Fig. 5.26. In comparison

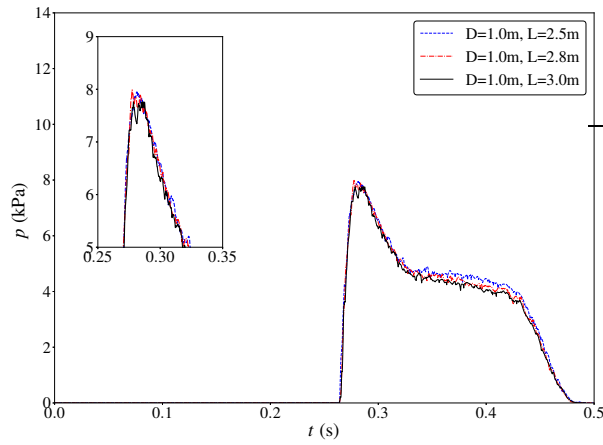
with other numerical methods, oscillations in pressures and forces were suppressed by the present higher-order method in symmetrical form. Furthermore, their peak values were summarized in Table 5.10 and Table 5.11 along with their relative errors. The predicted pressures and forces by the present method are in good agreement with the experimental data. The over-predictions of pressures/forces after the peak are potentially caused by the air entrapment and bubbles. Note that the present model does not account for air. The pressure fields at $t = 0.28$ s are compared in Fig. 5.27, which shows the improvement by the present higher-order method.



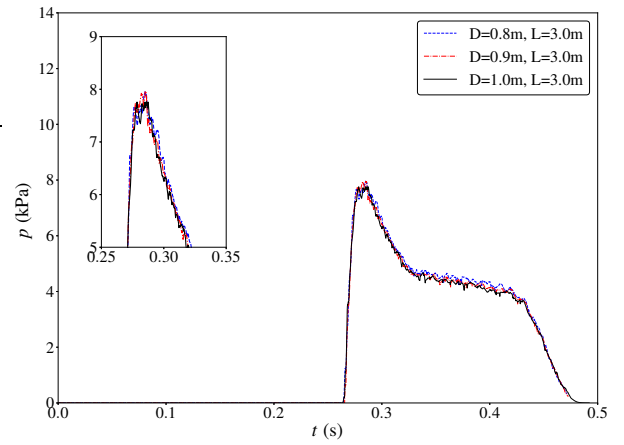
(a) Pressures at P1 with different domain widths



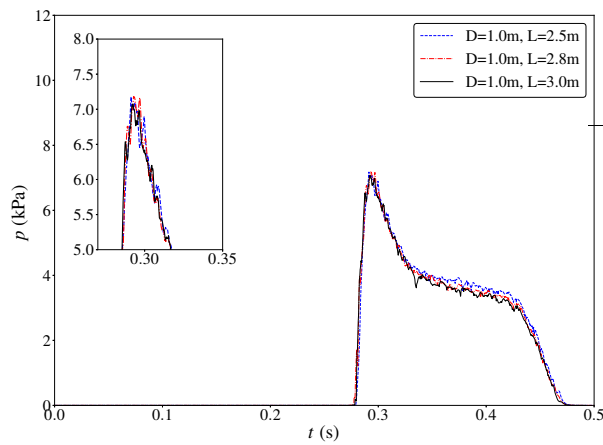
(b) Pressures at P1 with different domain depths



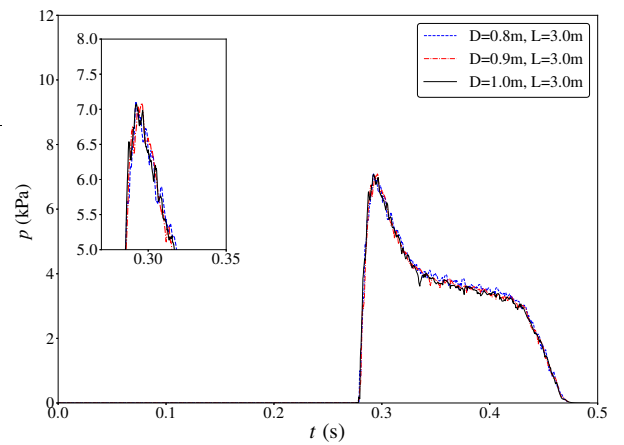
(c) Pressures at P2 with different domain widths



(d) Pressures at P2 with different domain depths

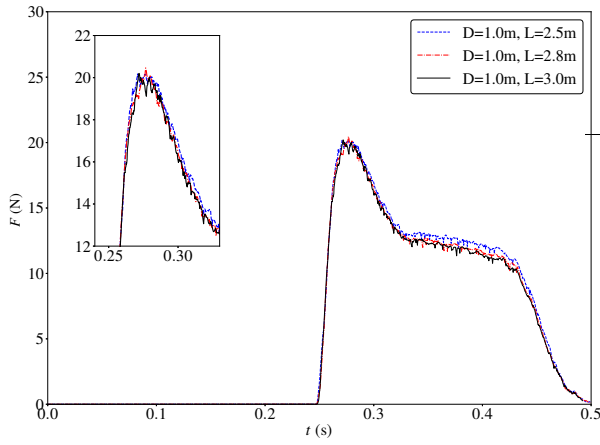


(e) Pressures at P3 with different domain widths

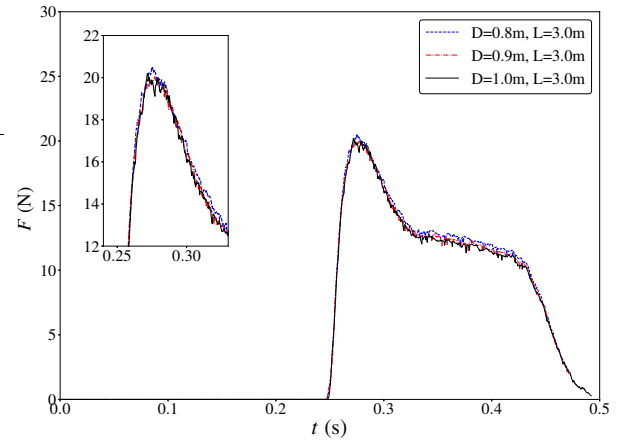


(f) Pressures at P3 with different domain depths

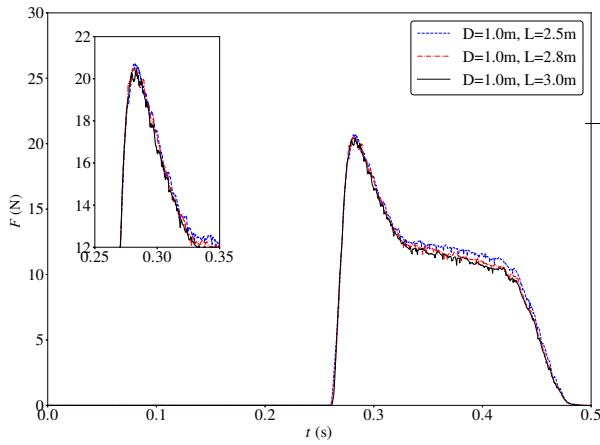
Figure 5.22: Sensitivities of pressures to domain size for the ship section (Model A)



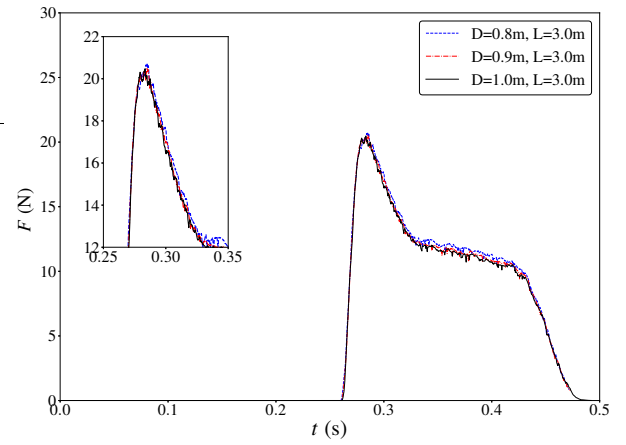
(a) Forces at F1 with different domain widths



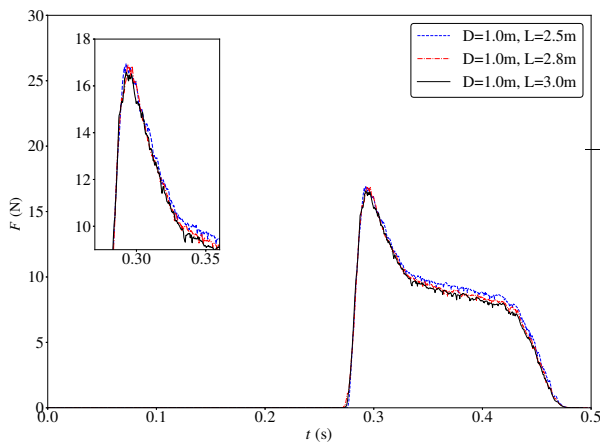
(b) Forces at F1 with different domain depths



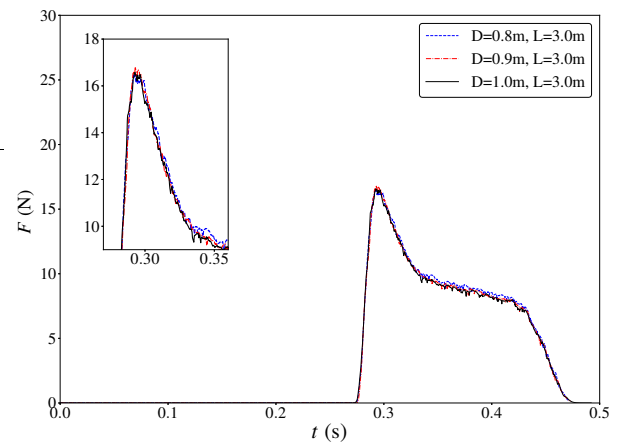
(c) Forces at F2 with different domain widths



(d) Forces at F2 with different domain depths

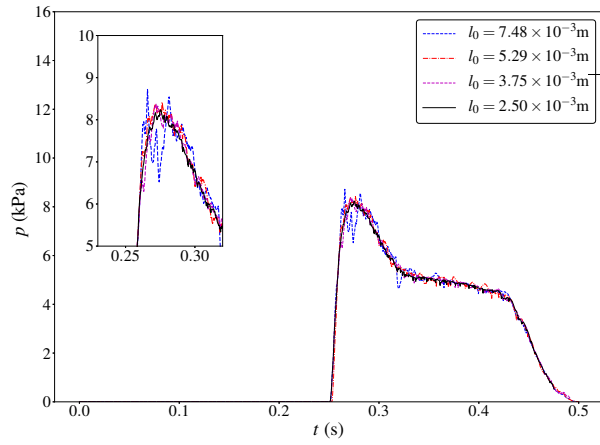


(e) Forces at F3 with different domain widths

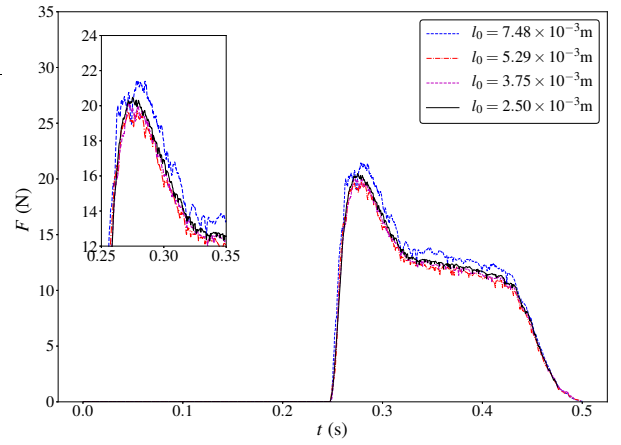


(f) Forces at F3 with different domain depths

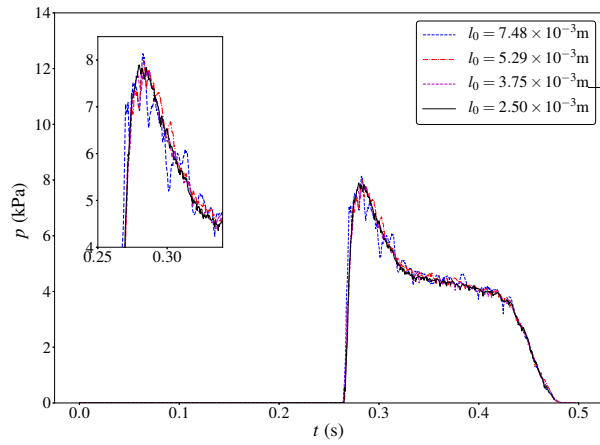
Figure 5.23: Sensitivities of forces to domain size for the ship section (Model A)



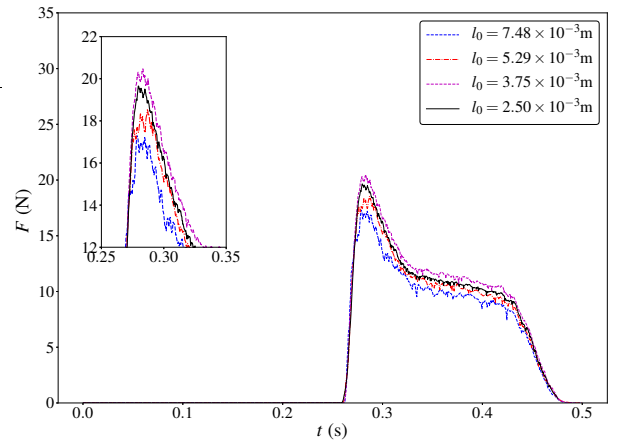
(a) Spatial convergence of pressure at P1



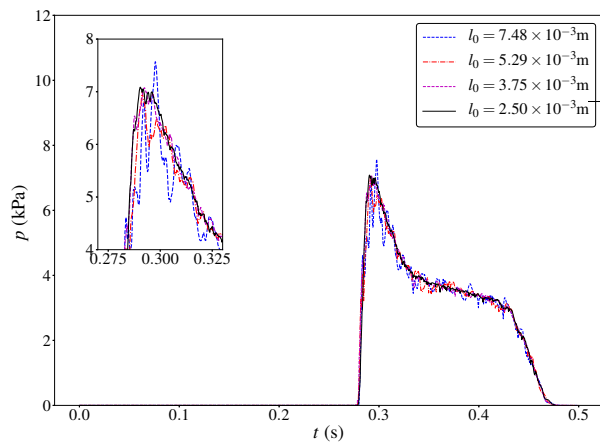
(b) Spatial convergence of forces at F1



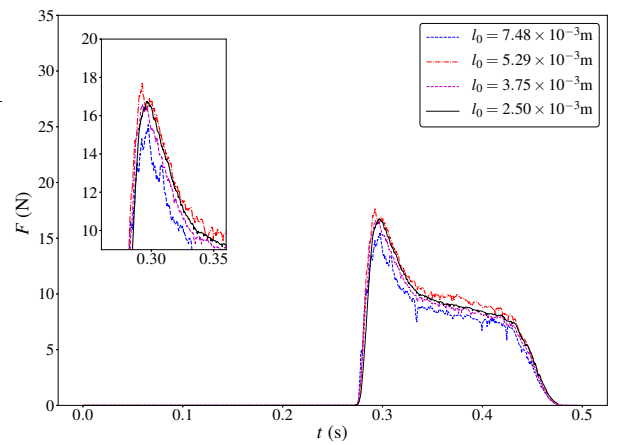
(c) Spatial convergence of pressure at P2



(d) Spatial convergence of forces at F2



(e) Spatial convergence of pressure at P3

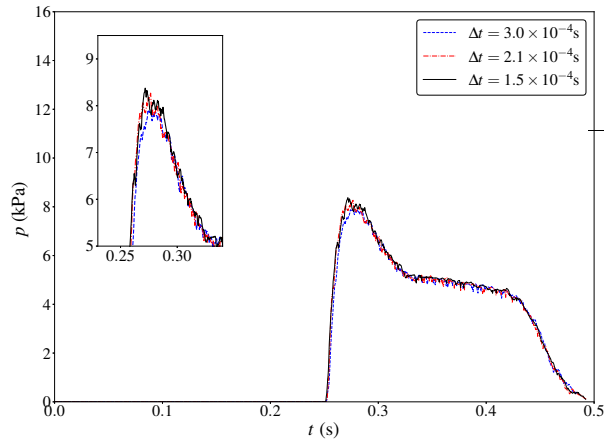


(f) Spatial convergence of forces at F3

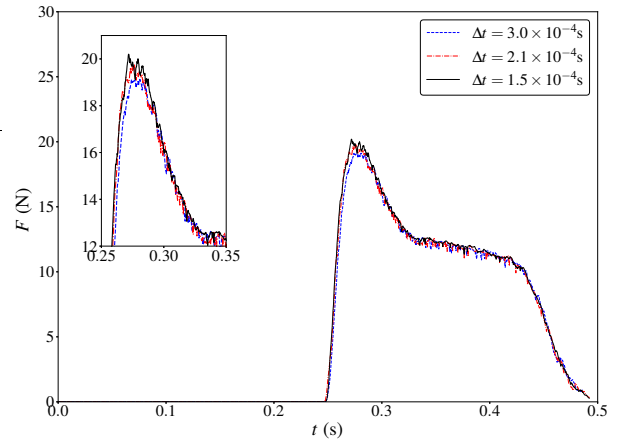
Figure 5.24: Spatial convergence of pressures and forces for the ship section (Model

Table 5.9: Uncertainties in predicted peak pressures and forces for the ship section (Model A)

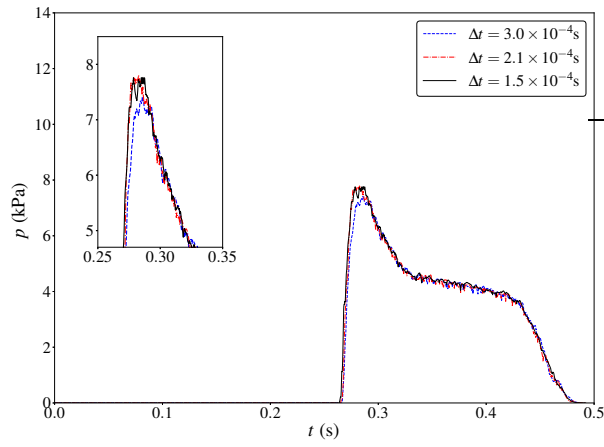
	Peak pressures			Peak forces		
	P1	P2	P3	F1	F2	F3
h_1	2.50×10^{-3}					
h_2	3.75×10^{-3}					
h_3	7.48×10^{-3}					
ϕ_1	8.23	7.89	7.09	20.48	19.66	16.74
ϕ_2	8.37	7.76	7.08	20.20	20.47	16.58
ϕ_3	8.72	8.14	7.57	21.45	17.29	15.54
p	1.45	2.14	7.23	2.97	2.73	3.40
ϕ_{ext}^{21}	8.06	7.99	7.09	20.60	19.25	16.80
e_a^{21}	1.71%	1.64%	0.16%	1.36%	4.14%	0.98%
e_{ext}^{21}	2.19%	1.18%	0.01%	0.58%	2.09%	0.33%
$\text{PCI}_{\text{fine}}^{21}$	2.68%	1.49%	0.01%	0.73%	2.56%	0.41%



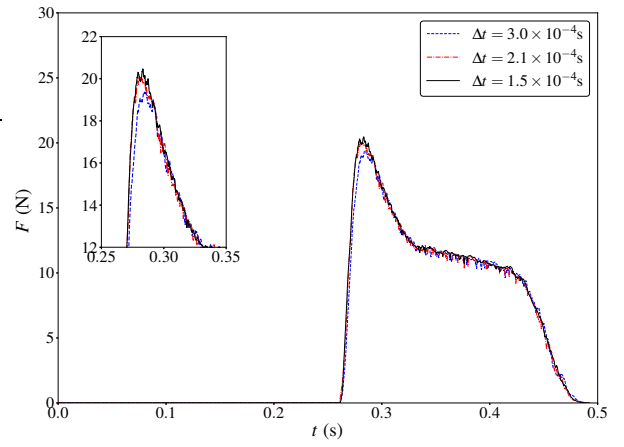
(a) Temporal convergence of pressure at P1



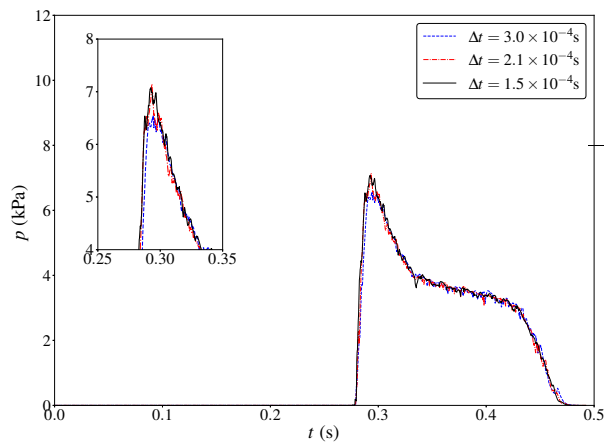
(b) Temporal convergence of force at F1



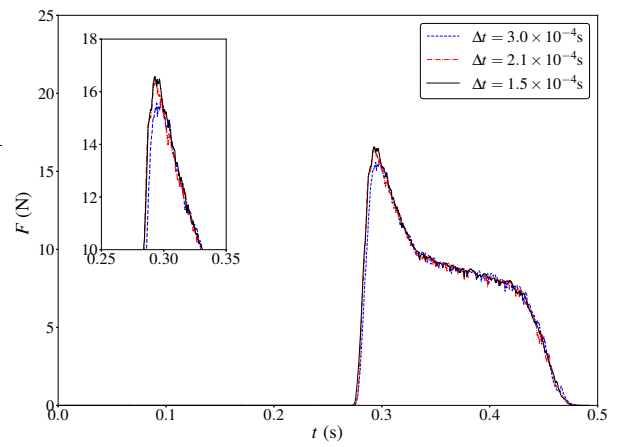
(c) Temporal convergence of pressure at P2



(d) Temporal convergence of force at F2

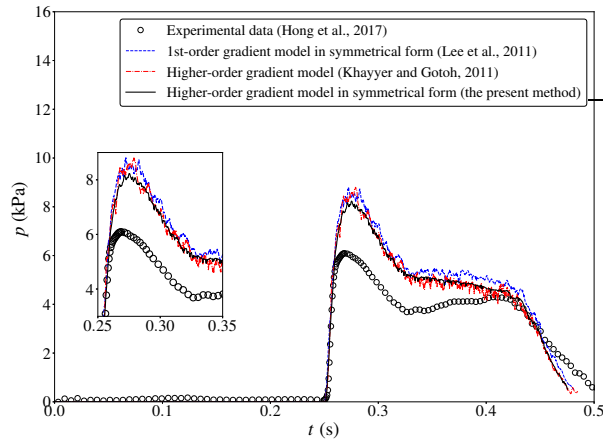


(e) Temporal convergence of pressure at P3

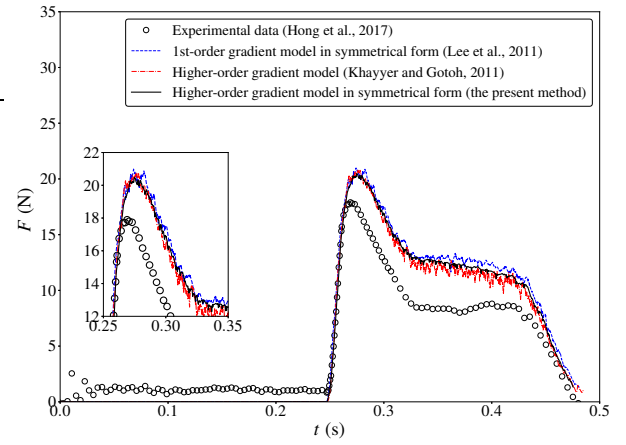


(f) Temporal convergence of force at F3

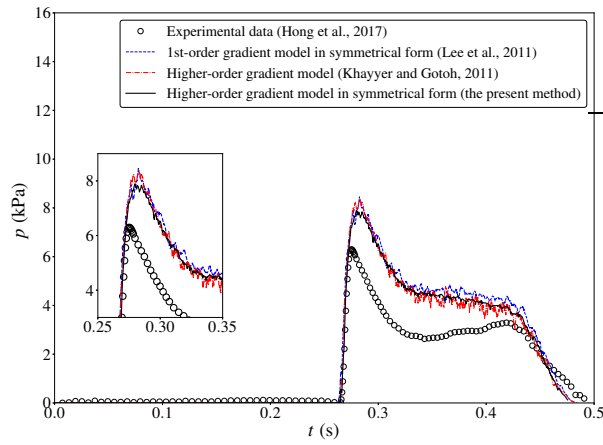
Figure 5.25: Temporal convergence of pressures and forces for the ship section (Model



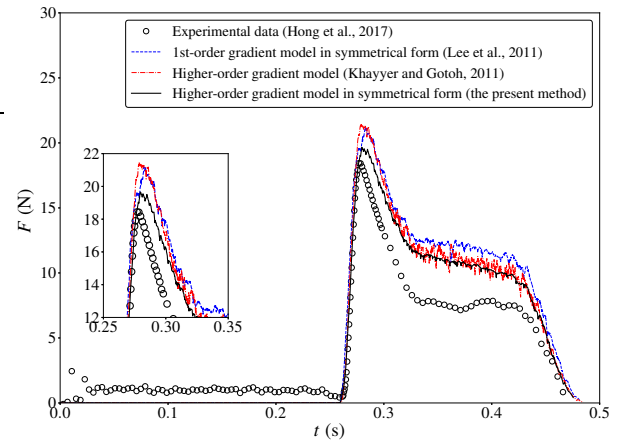
(a) Comparison of pressure at P1



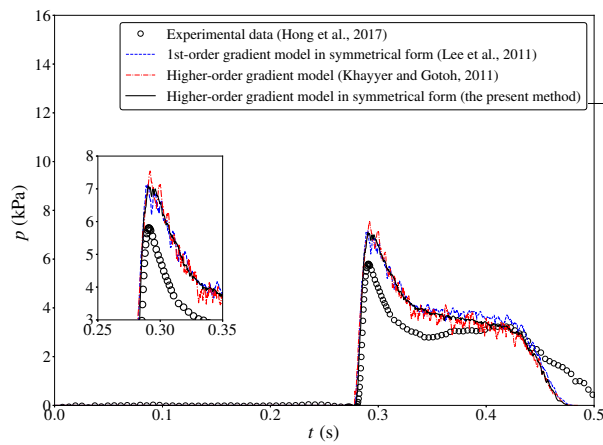
(b) Comparison of force at F1



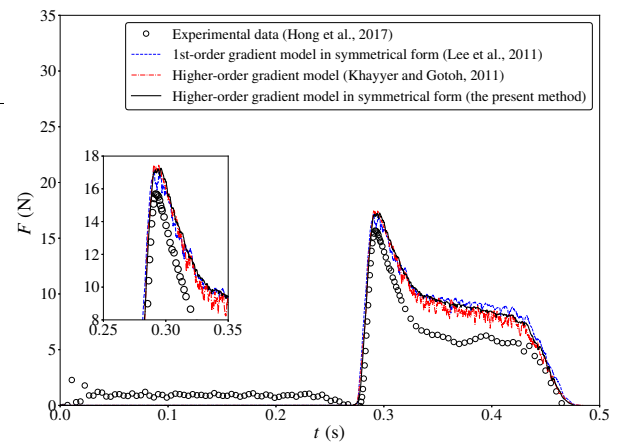
(c) Comparison of pressure at P2



(d) Comparison of force at F2



(e) Comparison of pressure at P3



(f) Comparison of force at F3

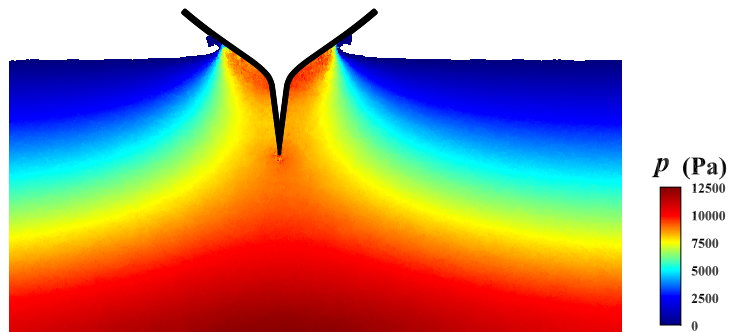
Figure 5.26: Comparison of pressures and forces for the ship section (Model A)

Table 5.10: The predicted pressures for the ship section (Model A)

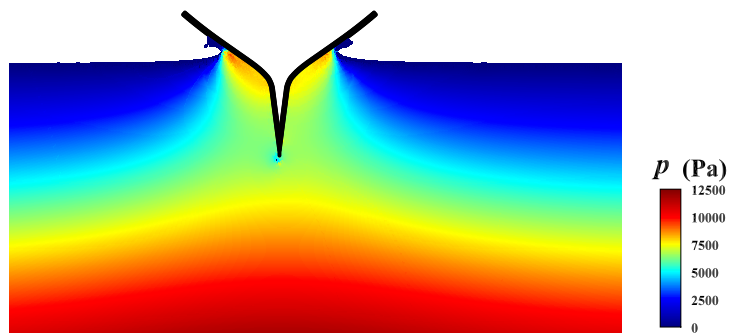
Methods	Peak pressure		Peak pressure		Peak pressure	
	P1 (kPa)	Error	P2 (kPa)	Error	P3 (kPa)	Error
Experimental data [26]	6.10	-	6.30	-	5.81	-
First-order gradient model [89]	8.81	44.50%	8.46	34.23%	7.16	23.27%
Higher-order gradient model [77]	8.80	44.39%	8.38	33.02%	7.55	29.91%
The present method	8.23	35.07%	7.89	25.31%	7.09	22.03%

Table 5.11: The predicted forces for the ship section (Model A)

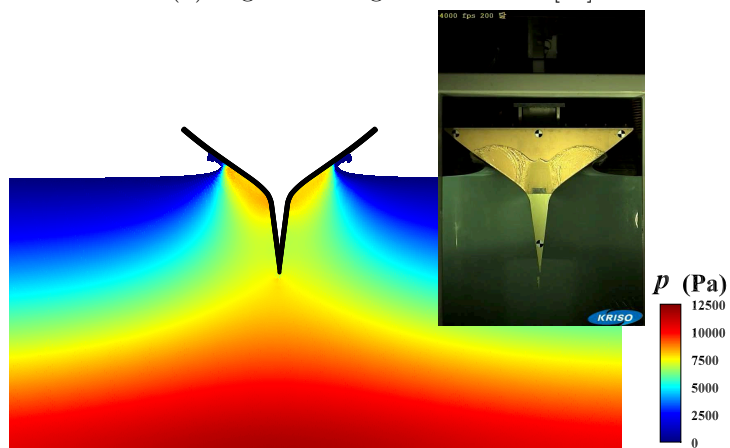
Methods	Peak force		Peak force		Peak force	
	F1 (N)	Error	F2 (N)	Error	F3 (N)	Error
Experimental data [26]	17.94	-	18.49	-	15.68	-
First-order gradient model [89]	20.99	16.98%	21.20	14.68%	17.22	9.81%
Higher-order gradient model [77]	20.78	15.80%	21.47	16.11%	17.46	11.33%
The present method	20.48	14.15%	19.66	6.32%	16.74	6.76%



(a) First-order gradient model [89]



(b) Higher-order gradient model [77]



(c) The present method and the comparison with experimental snapshot [26]

Figure 5.27: Comparison of pressure fields for the ship section (Model A)

5.2.2 2-D Ship Section (Model B)

Validation studies were extended to a 2-D ship section (Model B) (Hong et al. (2017) [26]). The drop height was $h = 0.17$ m. According to the previous studies of the 2-D ship section (Model A), the domain depth and width were set as 1.0 m and 3.0 m, respectively, which were sufficiently large to eliminate the wall effect. Spatial and temporal convergence studies were also conducted. The results of convergence studies for Model B are shown in Figure 5.28 and Fig. 5.29. It can be concluded that a particle spacing of 2.65×10^{-3} m and a time step of $\Delta t = 1.5 \times 10^{-4}$ s were adopted. The PCI values and the intermediate details for pressures and forces are given in Table 5.12.

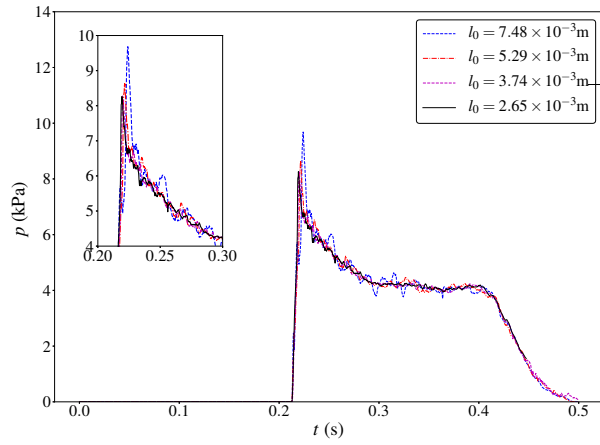
The predicted pressures and forces are presented in Fig. 5.30 and compared with the experimental data (Hong et al. (2017) [26]). The oscillations were generally suppressed and the peak pressures and forces were improved when the higher-order gradient model in symmetrical form was applied. The predicted peak values are summarized in Table 5.13 and Table 5.14 along with their relative errors. The pressures and forces after the peak and up to $t = 0.42$ s were over-predicted due to the fact that air entrapment was not considered in the present method. After $t = 0.42$ s, the predictions were in good agreement with the experimental data. The pressure fields at $t = 0.22$ s are also compared in Fig. 5.31. The pressure field by the present method with higher-order gradient model in symmetrical form is smoother than that by the first-order model and that by the original higher-order model. In summary, the present method with the higher-order gradient model in symmetrical form generally improved the prediction of pressures and forces for the 2-D ship section (Model B).

The following conclusions are made from the 2-D studies on rigid wedges and ship sections:

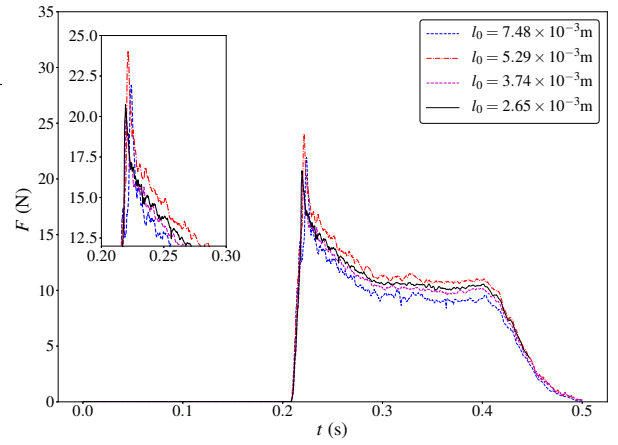
1. A higher-order MPS method with an improved pressure gradient model was developed to solve 2-D water entry problems. The pressure gradient model was modified to guarantee the first-order consistency and the conservation of momentum simultaneously. A particle shifting technique has been employed for further improvement. A particle convergence index (PCI) method was developed to evaluate the uncertainties in solutions by Lagrangian particle-based methods.
2. The present method with the higher-order gradient model in symmetrical form was validated by its applications to the water entries of a 2-D wedge with three tilt angles and two ship sections. The predicted pressures and forces converged as the domain size was increased, and as the particle spacing and the time step were decreased.
3. The PCI's of the predicted pressures and forces are less than 7%. Numerical results by the present method were generally in good agreement with the experimental data. In comparison with the first-order gradient model by Lee et al. (2011) [89], and the higher-order gradient model by Khayyer and Gotoh [77], the present method led to reduced relative errors in the predicted peak pressures and loads. Noises in the time histories of pressure and force and in the pressure fields were also suppressed by the present method. The over-predictions after the impact are likely caused by air entrapment and bubbles, which are not considered in the present method. As a summary, the present method with

the higher-order gradient model in symmetrical form improved the prediction of pressures and forces for wedges and ship sections during water entry.

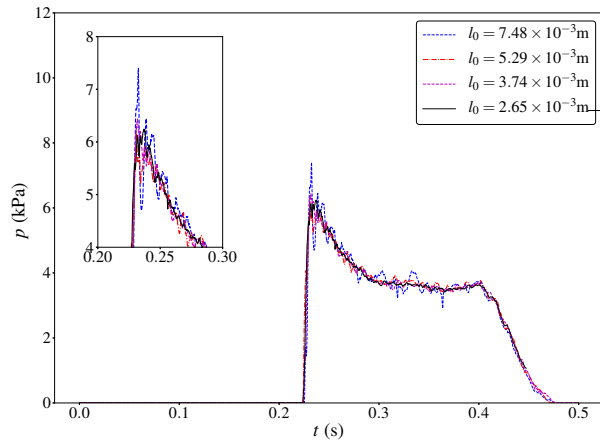
4. Based on the convergence studies, the following parameters are recommended for 2-D simulations of water entry with the present higher-order method. The domain width should be 4-5 times of the width of wedge or ship section. The CFL number should be less than 0.15 for numerical stability, where V , Δt and l_0 are the velocity when the object touches the water surface, the time step, and the particle spacing, respectively. For uniform distribution of particles in the computational domain, the number of particles per meter should be at least 360. In the present studies, the number of particles over the wedge width was 220 and the number of particles over the width of ship section was 270.



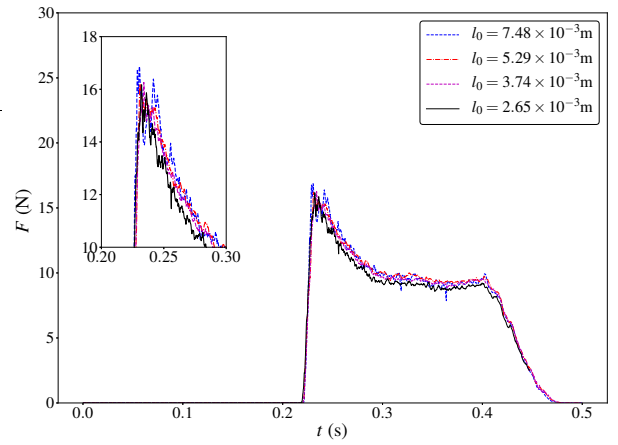
(a) Spatial convergence of pressure at P1



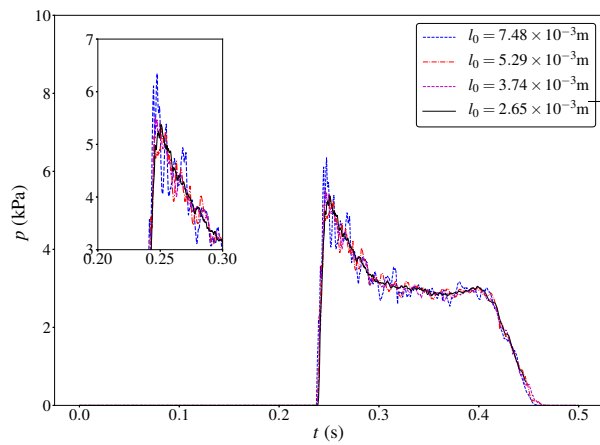
(b) Spatial convergence of force at F1



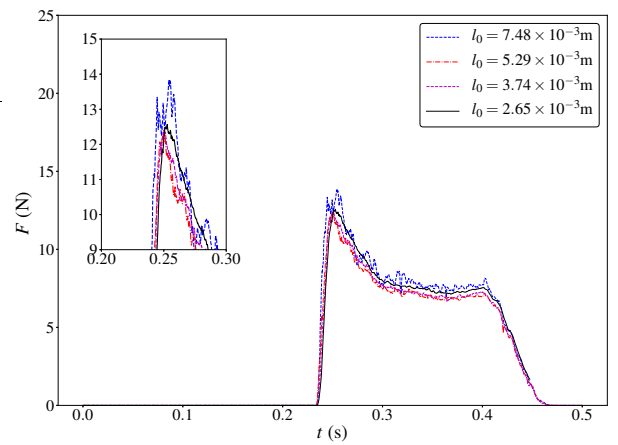
(c) Spatial convergence of pressure at P2



(d) Spatial convergence of force at F2



(e) Spatial convergence of pressure at P3

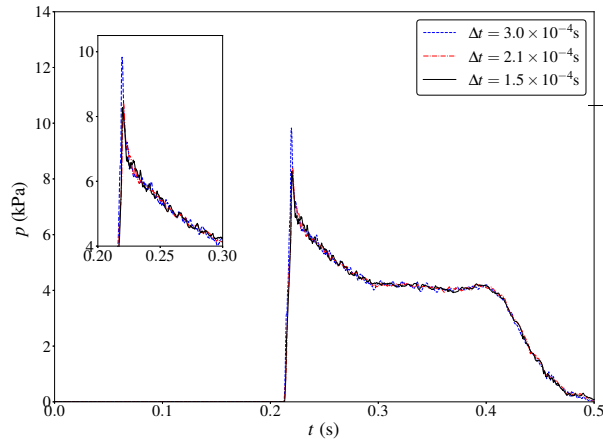


(f) Spatial convergence of force at F3

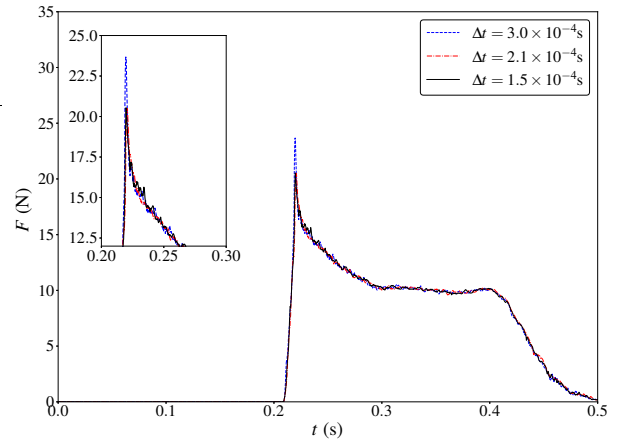
Figure 5.28: Spatial convergence of pressures and forces for the ship section (Model

Table 5.12: Uncertainties in predicted peak pressures and forces for the ship section (Model B)

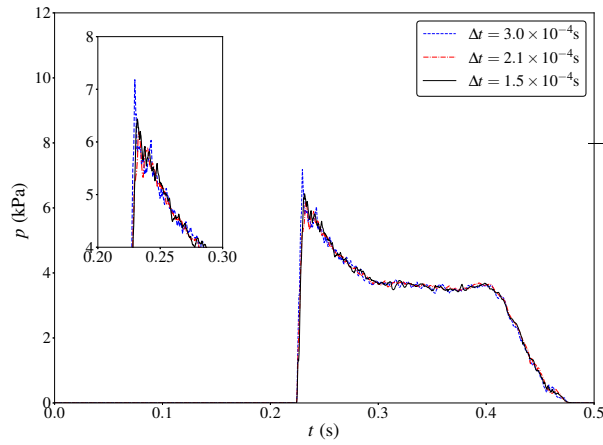
	Peak pressures			Peak forces		
	P1	P2	P3	F1	F2	F3
h_1	2.65×10^{-3}					
h_2	3.75×10^{-3}					
h_3	7.48×10^{-3}					
ϕ_1	8.26	6.24	5.37	20.74	16.17	12.57
ϕ_2	8.28	6.44	5.52	20.54	16.26	12.40
ϕ_3	9.68	7.40	6.35	21.93	16.87	13.85
p	9.66	3.24	3.57	4.35	3.95	4.746
ϕ_{ext}^{21}	8.26	6.15	5.32	20.79	16.14	12.61
e_a^{21}	0.19%	3.09%	2.67%	0.93%	0.55%	1.32%
e_{ext}^{21}	0.01%	1.51%	1.10%	0.26%	0.19%	0.31%
$\text{PCI}_{\text{fine}}^{21}$	0.008%	1.86%	1.36%	0.33%	0.23%	0.39%



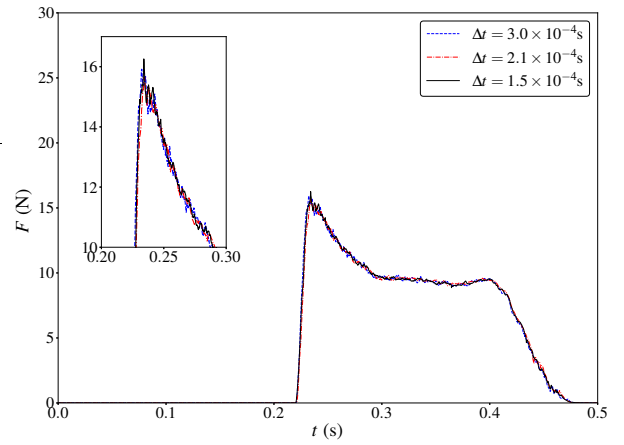
(a) Temporal convergence of pressure at P1



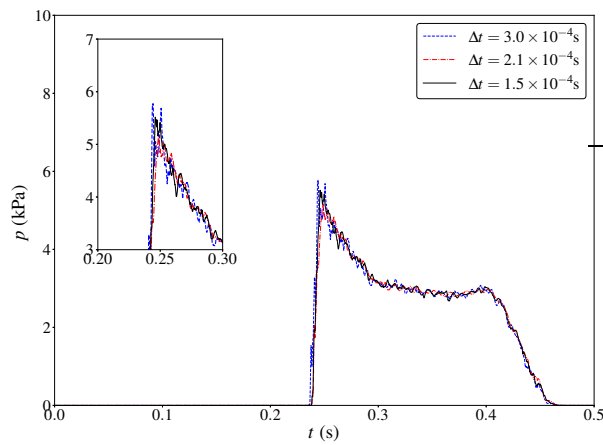
(b) Temporal convergence of force at F1



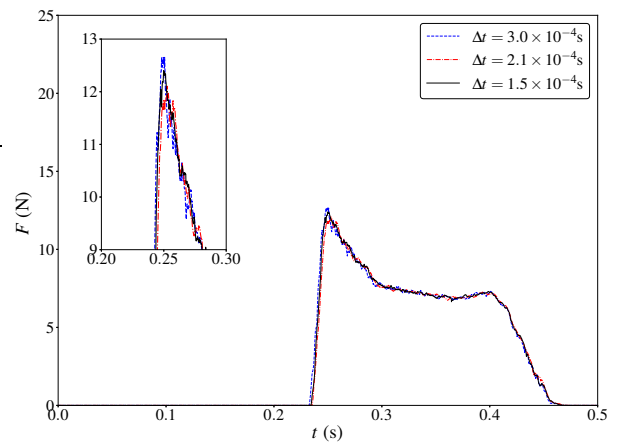
(c) Temporal convergence of pressure at P2



(d) Temporal convergence of force at F2

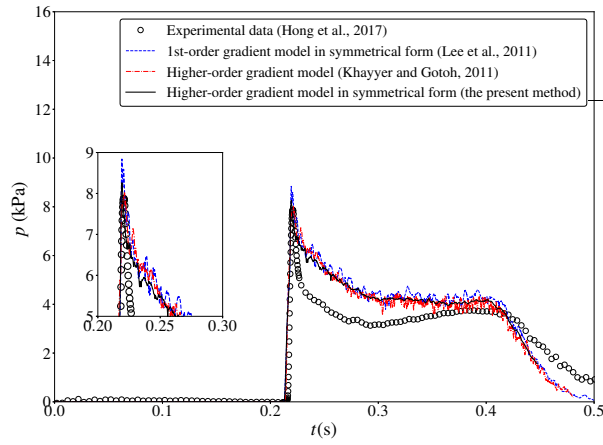


(e) Temporal convergence of pressure at P3

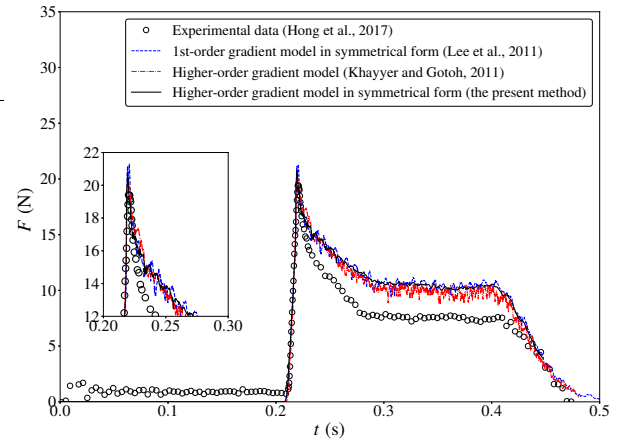


(f) Temporal convergence of force at F3

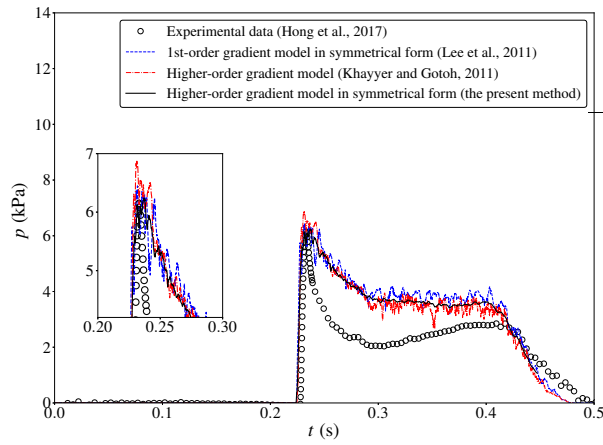
Figure 5.29: Temporal convergence of pressures and forces for the ship section (Model



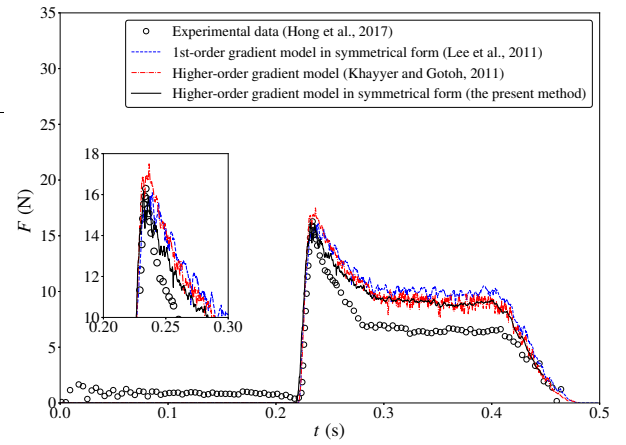
(a) Comparison of pressure at P1



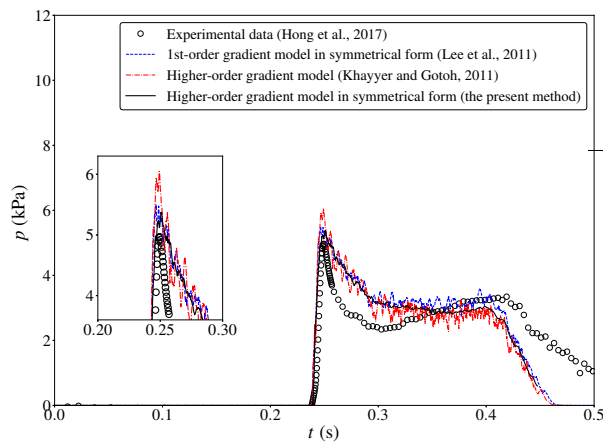
(b) Comparison of force at F1



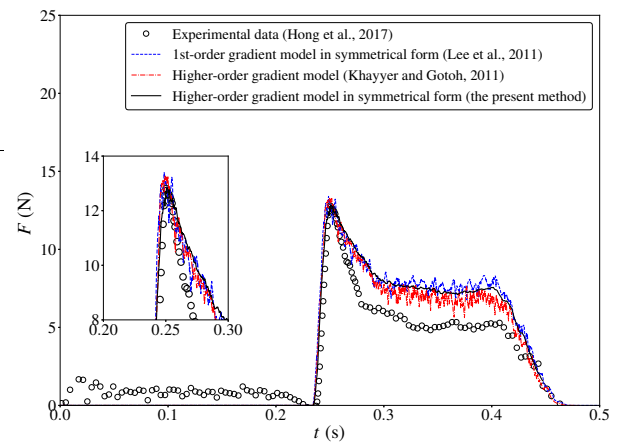
(c) Comparison of pressure at P2



(d) Comparison of force at F2



(e) Comparison of pressure at P3



(f) Comparison of force at F3

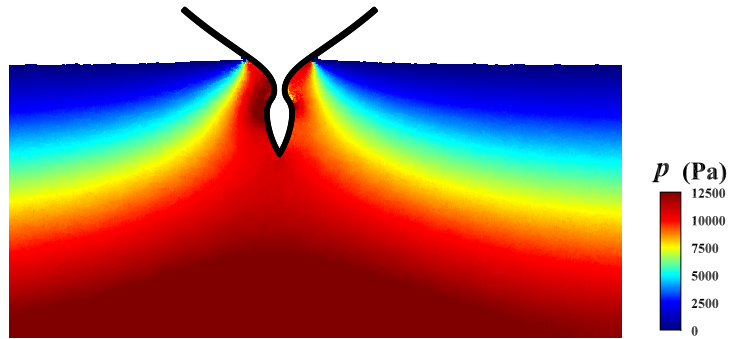
Figure 5.30: Comparison of pressures and forces for the ship section (Model B)

Table 5.13: The predicted pressures for the ship section (Model B)

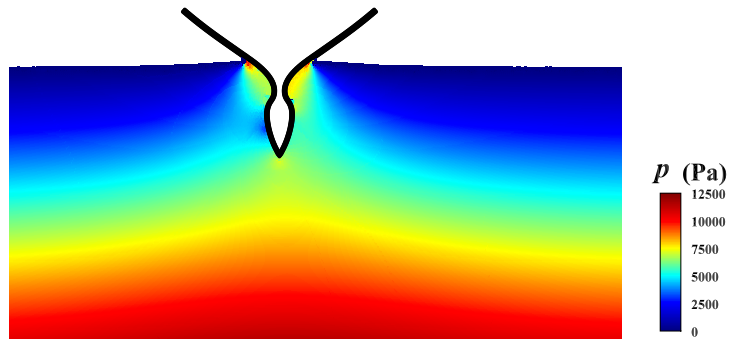
Methods	Peak pressure		Peak pressure		Peak pressure	
	P1 (kPa)	Error	P2 (kPa)	Error	P3 (kPa)	Error
Experimental data [26]	7.88	-	6.16	-	4.97	-
First-order gradient model [89]	8.84	12.20%	6.45	4.74%	5.50	10.74%
Higher-order gradient model [77]	8.02	1.74%	6.87	11.60%	6.05	21.69%
The present method	8.26	4.85%	6.24	1.39%	5.37	8.12%

Table 5.14: The predicted forces for the ship section (Model B)

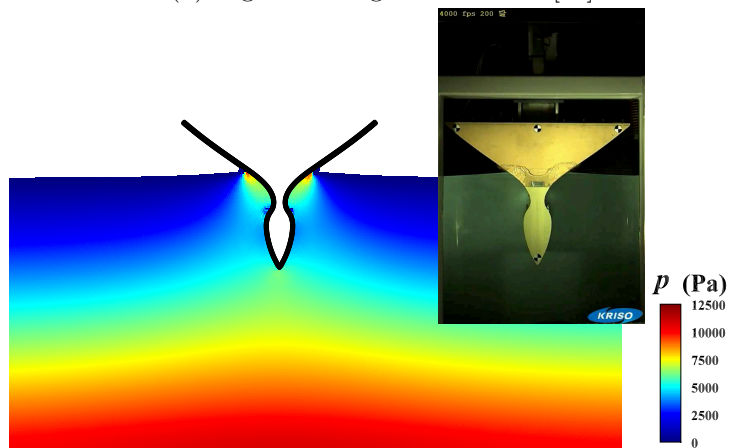
Methods	Peak force		Peak force		Peak force	
	F1 (N)	Error	F2 (N)	Error	F3 (N)	Error
Experimental data [26]	19.41	-	16.30	-	12.89	-
First-order gradient model [89]	21.30	9.78%	16.09	1.30%	13.40	3.95%
Higher-order gradient model [77]	20.25	4.35%	17.50	7.33%	13.27	2.96%
The present method	20.74	6.85%	16.17	0.82%	12.57	2.48%



(a) First-order gradient model [89]



(b) Higher-order gradient model [77]



(c) The present method and the comparison with experimental snapshot [26]

Figure 5.31: Comparison of pressure fields for the ship section (Model B)

Chapter 6

Solving 2-D Slamming of a Deformable Wedge with FSI

To further validate the present method, numerical simulations were conducted for water entry of the elastic wedge tested by Panciroli et al. (2012) [30]. The wedge was made of two composite panels (300 mm long, 250 mm wide and 2 mm thick) with connection only at the reinforced tip, which was considered as rigid in the numerical simulations. The composite panels were made by fibreglass. The density of structure was $\rho_s = 2,015 \text{ kg/m}^3$, Young's modulus was $E = 30.3 \text{ GPa}$, and the Poisson ratio was $\nu_s = 0.28$.

As shown in Fig. 6.1, the deadrise angle of the wedge was denoted as α and a strain gauge was located at 120 mm from the reinforced tip. The length of the computational domain was set as $L = 1.2 \text{ m}$ and the water depth was $D = 0.6 \text{ m}$ according to experimental set-ups. The numerical simulation started from the time instant of impact with an initial entry velocity, V , relative to the calm water, which

is corresponding to the drop height, H . As summarized in Table 6.1, two deadrise angles, $\alpha = 30^\circ$ and $\alpha = 20^\circ$, were investigated. For $\alpha = 30^\circ$, two initial entry velocities/drop heights for the free-fall motion were examined.

Note that since the elastic panel is ultra thin (2 mm), a much smaller particle spacing for the structure than that for the fluid was used.

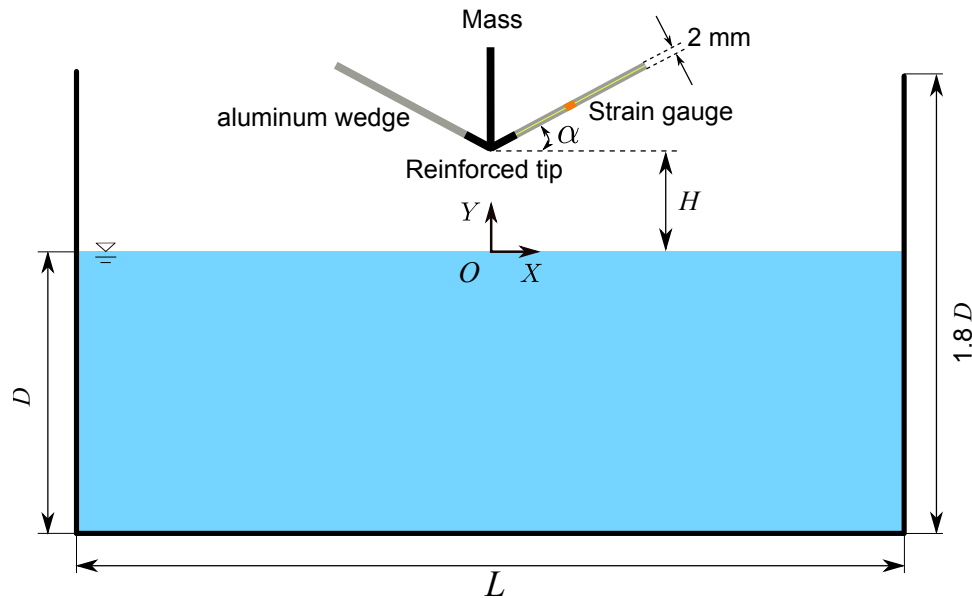


Figure 6.1: Computational domain for the hydroelastic impact

6.1 2-D Deformable Wedge with Deadrise Angle of $\alpha = 30^\circ$

Convergence studies on particle spacing and time step for the deadrise angle $\alpha = 30^\circ$ and the drop height $H = 0.39$ m were listed in Table 6.2. The spatial convergence

Table 6.1: Summary of cases for the hydroelastic impact

Deadrise angle, α ($^\circ$)	Drop height, H (m)	Entry velocity, V (m/s)
30	0.39	2.770
30	0.50	3.132
20	0.50	3.132

Table 6.2: Convergence studies on particle spacing and time step for the fluid ($\alpha = 30^\circ$ and $H = 0.39$ m)

No.	Fluid particle spacing, l_{f0} (m)	Structural particle spacing, l_{s0} (m)	Time step for fluid, Δt_f (s)	Time step for structure, Δt_s (s)
1	4.00×10^{-3}	0.50×10^{-3}	1.00×10^{-4}	0.33×10^{-7}
2	2.00×10^{-3}	0.50×10^{-3}	0.50×10^{-4}	0.33×10^{-7}
3	1.00×10^{-3}	0.50×10^{-3}	0.25×10^{-4}	0.33×10^{-7}
4	1.00×10^{-3}	0.50×10^{-3}	0.50×10^{-4}	0.33×10^{-7}
5	1.00×10^{-3}	0.50×10^{-3}	0.75×10^{-4}	0.33×10^{-7}

study for the fluid involved three sets of particles. The fluid particle spacings were $l_{f0} = 4.0 \times 10^{-3}$ m, 2.0×10^{-3} m and 1.0×10^{-3} m, respectively, and the structural particle spacing was set as $l_{s0} = 0.5 \times 10^{-3}$ m for all cases. In all the three cases, the CFL number was set as 0.14 for the fluid and 0.18×10^{-3} for the structure. Figure

Table 6.3: Convergence studies on the number of particle layers across the thickness of the plate ($\alpha = 30^\circ$ and $H = 0.39$ m)

No.	Fluid particle spacing, l_{f0} (m)	Structural particle spacing, l_{s0} (m)	Ratio of spacing, l_{f0}/l_{s0}	Number of particle layers
1	1.00×10^{-3}	1.00×10^{-3}	1.00	2
2	1.00×10^{-3}	0.50×10^{-3}	2.00	4
3	1.00×10^{-3}	0.33×10^{-3}	3.00	6
4	1.00×10^{-3}	0.25×10^{-3}	4.00	8

6.2 presents the time histories of the predicted strain at the strain gauge. It can be seen that the numerical solutions converged and the fluctuations were suppressed as the particle spacing was reduced. The numerical oscillations in structural strain were due to the oscillations of the pressure on the fluid-structure interface. In Fig. 6.2, the numerical oscillations were caused by a coarse spatial discretization. Note that the number of particles needs to be adequate. If not, the flow field and the interfaces cannot be described accurately, and numerical errors will therefore be relatively large. As concluded from the spatial convergence study, the numerical oscillations can be suppressed by using a smaller particle spacing.

Furthermore, three cases with different time steps for the fluid were employed to investigate the temporal convergence, i.e., $\Delta t_f = 7.5 \times 10^{-5}$ s, 5.0×10^{-5} s and 2.5×10^{-5} s. The time step for the structure was fixed as $\Delta t_s = 3.3 \times 10^{-8}$ s. The predicted local strains are presented in Fig. 6.3. The fluctuations were suppressed and

the solutions converged as the time step was reduced. In Fig. 6.3, the oscillations were resulted from large time steps. For time marching with a large time step, particles move inaccurately and non-physical collisions between particles and boundaries might occur. Therefore, a decrease in the time step helps suppress the numerical oscillations and improves the numerical stability.

As presented in Table 6.3, convergence studies on the number of particle layers across the thickness of the plate were also carried out. Four sets of particle layers were set as 2, 4, 6 and 8. The structural particle spacings were $l_{s0} = 1.0 \times 10^{-3}$ m, 0.5×10^{-3} m, 0.33×10^{-3} m and 0.25×10^{-3} m, respectively. The fluid particle spacing was $l_{f0} = 1.0 \times 10^{-3}$ m for all cases. The predicted local strains are presented in Fig. 6.4, which converged as the number of particle layers was increased.

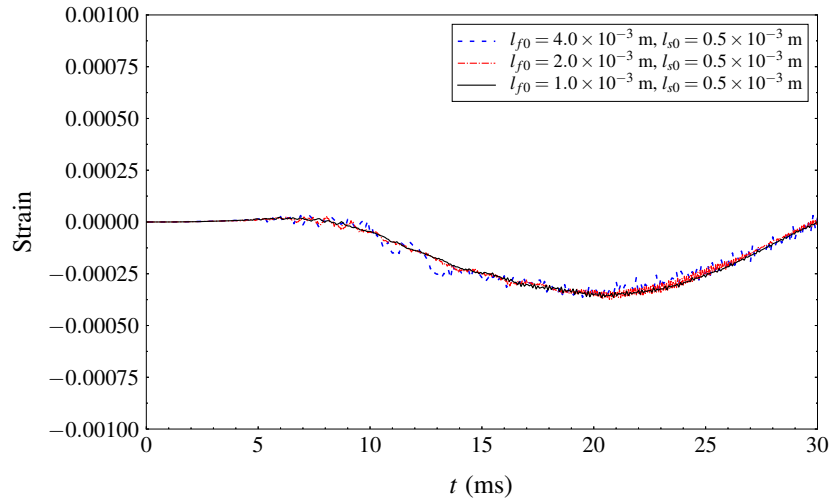


Figure 6.2: Convergence of local strains to particle spacing ($\alpha = 30^\circ$ and $H = 0.39$ m)

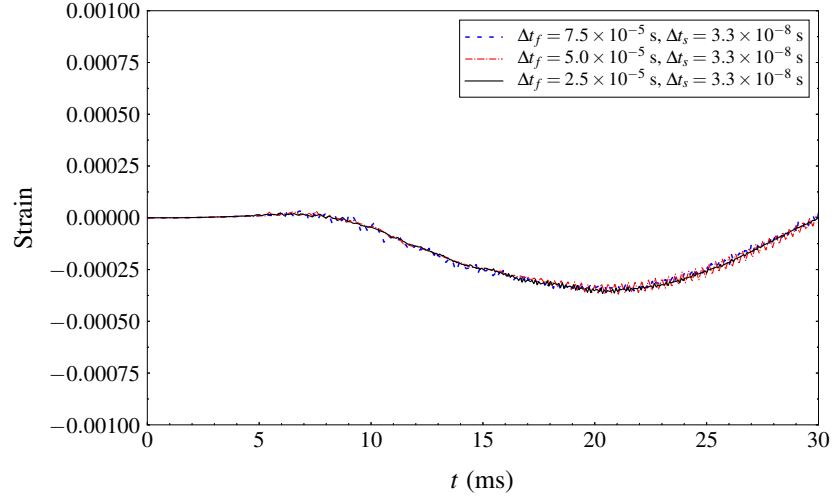


Figure 6.3: Convergence of local strains to time step ($\alpha = 30^\circ$ and $H = 0.39$ m)

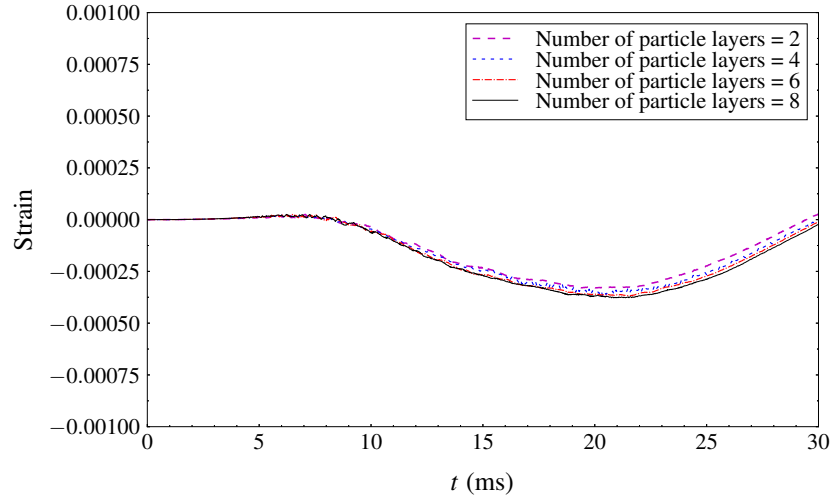


Figure 6.4: Convergence of local strains to the number of particle layers across the thickness of the plate ($\alpha = 30^\circ$ and $H = 0.39$ m)

Uncertainties in the maximum strain magnitude, $|\boldsymbol{\varepsilon}|_{\max}$, due to the spatial resolutions of fluid and structure were evaluated. The corresponding PCI's and the

intermediate details are presented in Table 6.4. It can be seen that uncertainties in solutions due to spatial resolution are small. Therefore, the particle spacings of $l_{f0} = 1.0 \times 10^{-3}$ m and $l_{s0} = 0.33 \times 10^{-3}$ m were employed in the following studies.

Table 6.4: Uncertainties in maximum strain magnitude due to spatial resolution in terms of l_{f0} and l_{s0} for the elastic wedge ($\alpha = 30^\circ$ and $H = 0.39$ m)

Item	Uncertainties due to l_{f0}	Uncertainties due to l_{s0}
h_1	1.0×10^{-3}	0.3×10^{-3}
h_2	2.0×10^{-3}	0.5×10^{-3}
h_3	4.0×10^{-3}	1.0×10^{-3}
ϕ_1	3.66×10^{-4}	3.69×10^{-4}
ϕ_2	3.74×10^{-4}	3.66×10^{-4}
ϕ_3	3.64×10^{-4}	3.30×10^{-4}
p	0.39	3.31
ϕ_{ext}^{21}	3.42×10^{-4}	3.70×10^{-4}
e_a^{21}	2.05%	0.82%
e_{ext}^{21}	7.01%	0.29%
PCI _{fine} ²¹	8.19%	0.36%

Numerical results based on the particle spacings of $l_{f0} = 1.0 \times 10^{-3}$ m, $l_{s0} = 0.33 \times 10^{-3}$ m are presented below. The corresponding number of fluid particles is 737,124 and the number of structural particles is 10,806. The CFL number was

fixed as 0.14 for the fluid and 0.18×10^{-3} for the structure. As shown in Fig. 6.7, the predicted strains for the deadrise angle of $\alpha = 30^\circ$ are in a good agreement with the experimental data [31]. They are also compared with the numerical results obtained using the original higher-order gradient model proposed by Khayyer and Gotoh (2011) [77]. The errors were reduced and the oscillations were suppressed by the present method with the higher-order gradient model in symmetrical form. The contours of fluid pressure and strain of the elastic panel are shown in Fig. 6.5 and Fig. 6.6. For the far field region, the pressure contours obtained by the present method are generally the same as the results by the original higher-order gradient model. For the near field region, i.e., close to the wedge surface, the pressure distributions by the original higher-order gradient model are not symmetrical about the tip in Fig. 6.5, while it was improved for the results obtained by the improved higher-order model as shown in Fig. 6.6. The numerical noises in the results by the original higher-order gradient model [77] were reduced with the present model.

Another drop height, $H = 0.5$ m, was also investigated. The numerical results were obtained using the same particle spacings and the CFL numbers as those for the cases with $H = 0.39$ m. As shown in Fig. 6.8, the predicted strains generally agree with the experimental data [31]. A larger structural deformation was observed because of the higher impact velocity. The frequencies of vibration were similar for the two drop heights for the wedge with the deadrise angle of $\alpha = 30^\circ$. The discrepancy for the maximum strain between 10 to 20 seconds is relatively large. The discrepancy between numerical results and experimental data is likely caused by air entrapment and bubbles. In experiments, air could be entrapped in waters. In present work, air phase was not considered. The impact pressures measured in experiment are therefore

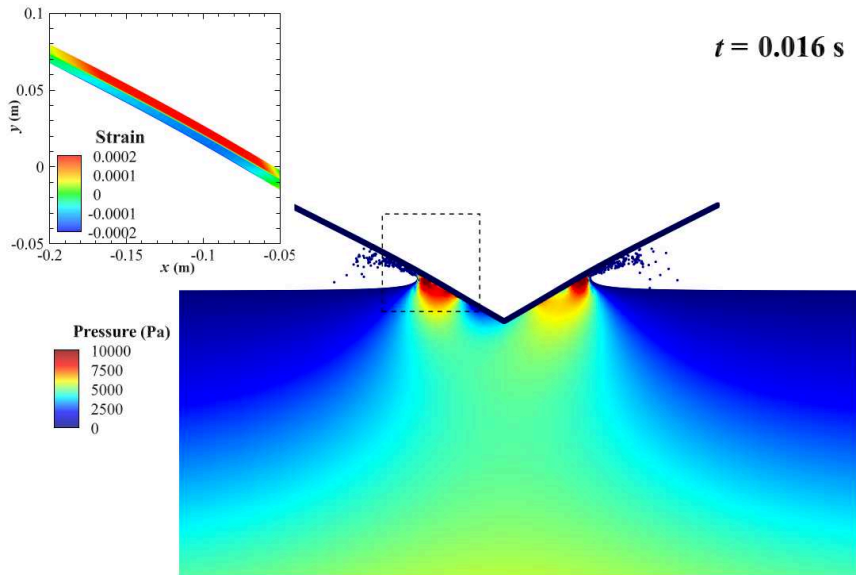


Figure 6.5: Contours by the original higher-order gradient model ($\alpha = 30^\circ$ and $H = 0.39 \text{ m}$)

a little smaller than the numerical solutions. Consequently, the maximum structural strain measured in experiment is smaller than the numerical one. The structural deformation was reaching the maximum in the period between 10 to 20 seconds. The drop height and the impact velocity were higher in Fig. 6.8 in comparison with Fig. 6.7. There could be more air entrapment and bubbles. Numerical results could be improved by using the multi-phase solver to consider the effect of air phase to the fluid-structural interaction.

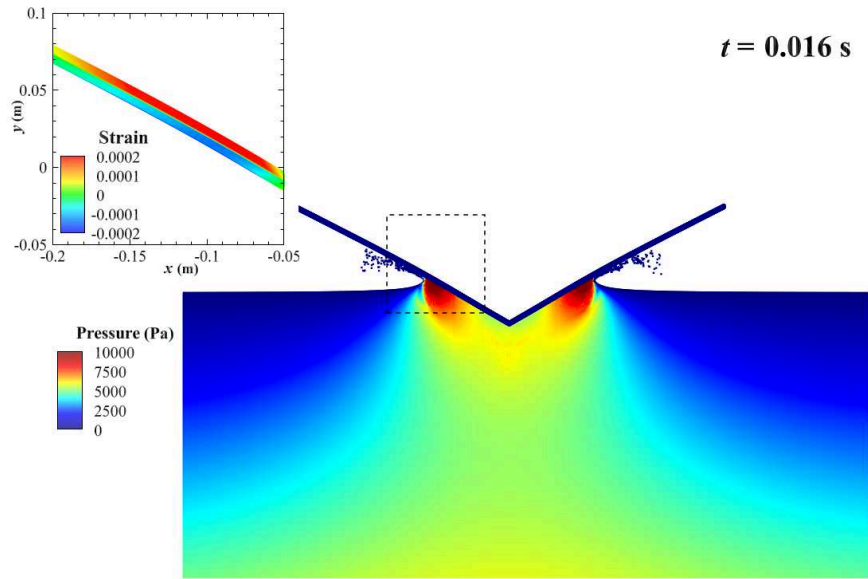


Figure 6.6: Contours by the present higher-order gradient model in symmetrical form ($\alpha = 30^\circ$ and $H = 0.39 \text{ m}$)

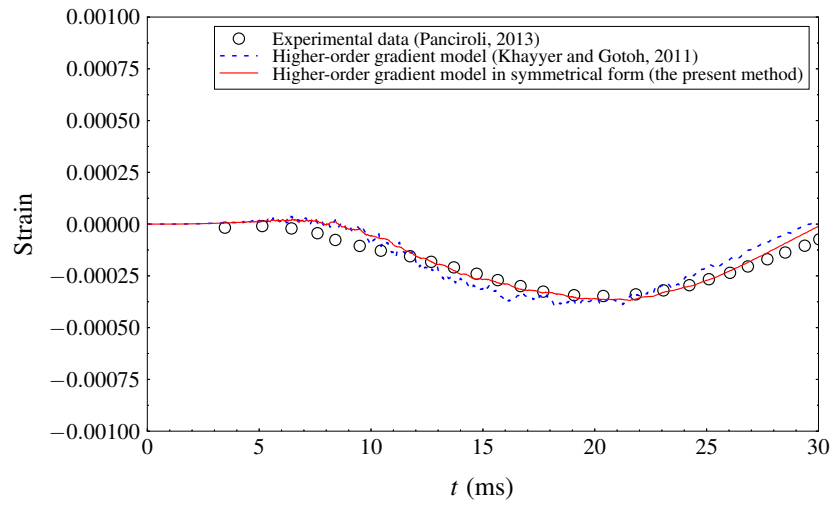


Figure 6.7: Comparison of local strains ($\alpha = 30^\circ$ and $H = 0.39 \text{ m}$)

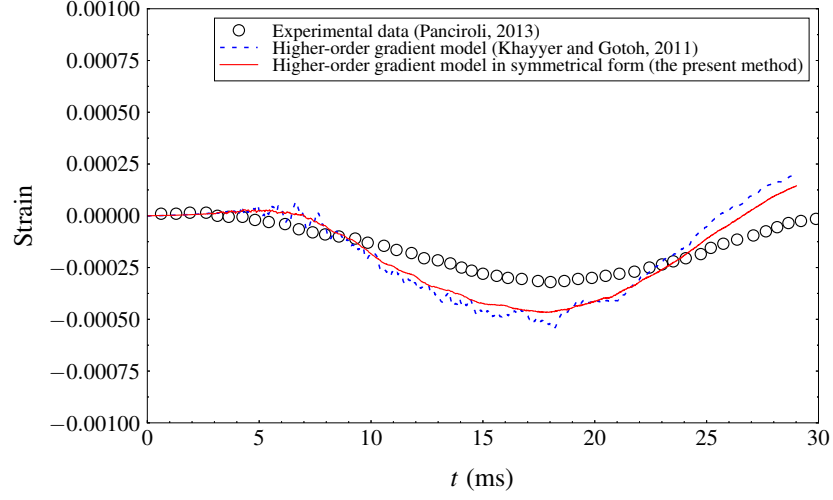


Figure 6.8: Comparison of local strains ($\alpha = 30^\circ$ and $H = 0.5$ m)

Table 6.5: Convergence studies on particle spacing and time step for the fluid ($\alpha = 20^\circ$ and $H = 0.5$ m)

No.	Fluid particle spacing, l_{f0} (m)	Structural particle spacing, l_{s0} (m)	Time step for fluid, Δt_f (s)	Time step for structure, Δt_s (s)
1	4.00×10^{-3}	0.50×10^{-3}	1.00×10^{-4}	0.33×10^{-7}
2	2.00×10^{-3}	0.50×10^{-3}	0.50×10^{-4}	0.33×10^{-7}
3	1.00×10^{-3}	0.50×10^{-3}	0.25×10^{-4}	0.33×10^{-7}
4	1.00×10^{-3}	0.50×10^{-3}	0.50×10^{-4}	0.33×10^{-7}
5	1.00×10^{-3}	0.50×10^{-3}	0.75×10^{-4}	0.33×10^{-7}

Table 6.6: Convergence studies on the number of particle layers across the thickness of the plate ($\alpha = 20^\circ$ and $H = 0.5$ m)

No.	Fluid particle spacing, l_{f0} (m)	Structural particle spacing, l_{s0} (m)	Ratio of spacing, l_{f0}/l_{s0}	Number of particle layers
1	1.00×10^{-3}	1.00×10^{-3}	1.00	2
2	1.00×10^{-3}	0.50×10^{-3}	2.00	4
3	1.00×10^{-3}	0.33×10^{-3}	3.00	6
4	1.00×10^{-3}	0.25×10^{-3}	4.00	8

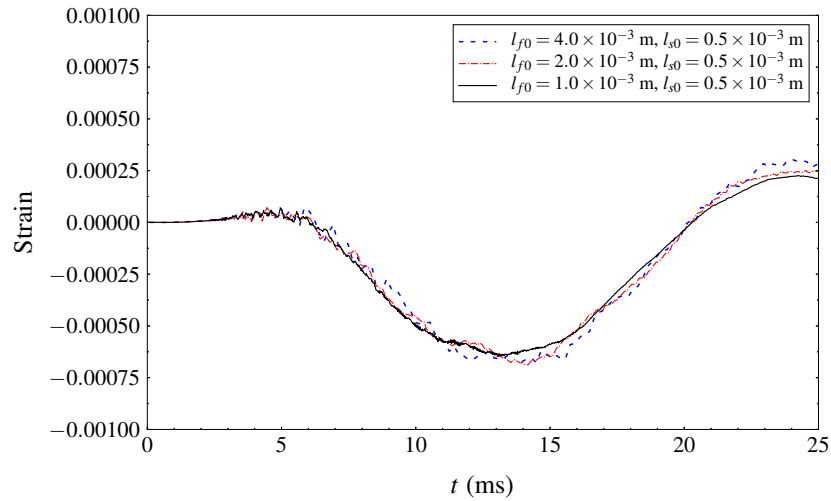


Figure 6.9: Convergence of local strains to particle spacing ($\alpha = 20^\circ$ and $H = 0.5$ m)

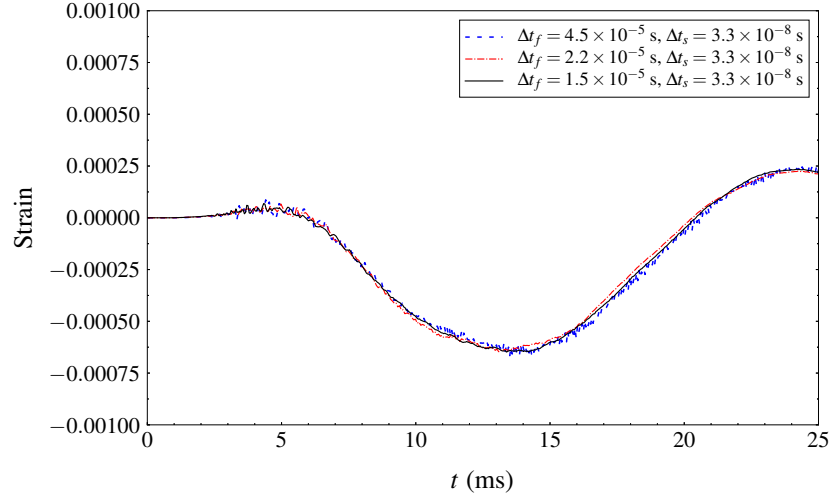


Figure 6.10: Convergence of local strains to time step ($\alpha = 20^\circ$ and $H = 0.5$ m)

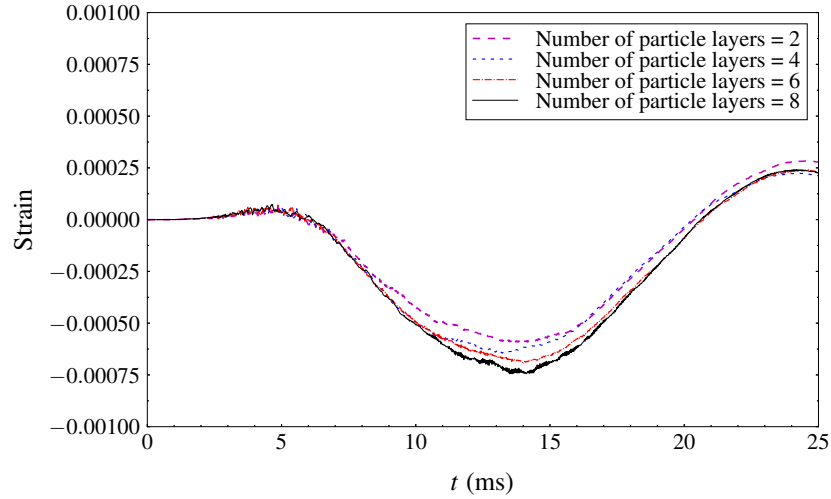


Figure 6.11: Convergence of local strains to the number of particle layers across the thickness of the plate ($\alpha = 20^\circ$ and $H = 0.5$ m)

6.2 2-D Deformable Wedge with Deadrise Angle

of $\alpha = 20^\circ$

For a smaller deadrise angle of the wedge ($\alpha = 20^\circ$), convergence cases with respect to particle spacing and time step for the drop height of $H = 0.5$ m are presented in

Table 6.5. In the spatial convergence study, three sets of fluid particle spacings were $l_{f0} = 4.0 \times 10^{-3}$ m, 2.0×10^{-3} m and 1.0×10^{-3} m. The structural particle spacing was $l_{s0} = 0.5 \times 10^{-3}$ m for all cases. The CFL number was 0.14 for the fluid and 0.18×10^{-3} for the structure. Figure 6.9 presents the time histories of the predicted strain at the strain gauge. It can be seen that the numerical solutions converged and the fluctuations were suppressed as the particle spacing was reduced.

Furthermore, three cases with different time steps for the fluid were used to investigate the temporal convergence, including $\Delta t_f = 7.5 \times 10^{-5}$ s, 5.0×10^{-5} s and 2.5×10^{-5} s. The time step for the structure was kept as $\Delta t_s = 3.3 \times 10^{-8}$ s. The predicted local strains are presented in Fig. 6.10, which converged as the time step was reduced. It can be observed that the fluctuations were also suppressed with the decreased time step.

As presented in Table 6.6, four numbers of particle layers across the thickness of the plate were used, i.e., 2, 4, 6 and 8. The corresponding structural particle spacings are $l_{s0} = 1.0 \times 10^{-3}$ m, 0.5×10^{-3} m, 0.33×10^{-3} m and 0.25×10^{-3} m, respectively. The particle spacing for the fluid was kept as $l_{f0} = 1.0 \times 10^{-3}$ m for all cases. The predicted local strains are presented in Fig. 6.11, which converged as the number of particle layers was increased.

Uncertainties in the maximum strain magnitude, $|\varepsilon|_{\max}$, due to spatial resolutions of fluid and structure are presented in Table 6.7. It can be seen that uncertainties due to spatial resolution are small. Therefore, the particle spacings of $l_{f0} = 1.0 \times 10^{-3}$ m and $l_{s0} = 0.33 \times 10^{-3}$ m were employed for the following simulations.

Furthermore, larger deformations occurred for the deadrise angle $\alpha = 20^\circ$ of the wedge with the same drop height, as presented in Fig. 6.12. Compared with the results

Table 6.7: Uncertainties in the maximum strain magnitude due to spatial resolution in terms of l_{f0} and l_{s0} for the elastic wedge ($\alpha = 20^\circ$ and $H = 0.5$ m)

Item	Uncertainties due to l_{f0}	Uncertainties due to l_{s0}
h_1	1.0×10^{-3}	0.25×10^{-3}
h_2	2.0×10^{-3}	0.33×10^{-3}
h_3	4.0×10^{-3}	0.50×10^{-3}
ϕ_1	6.47×10^{-4}	7.45×10^{-4}
ϕ_2	6.89×10^{-4}	6.92×10^{-4}
ϕ_3	6.77×10^{-4}	6.47×10^{-4}
p	1.83	2.26
ϕ_{ext}^{21}	6.31×10^{-4}	8.03×10^{-4}
e_a^{21}	6.44%	7.11%
e_{ext}^{21}	2.59%	7.19%
PCI _{fine} ²¹	3.16%	9.69%

using the original higher-order model (MPS-HS-HL-ECS-GC) proposed by Khayyer and Gotoh (2011) [77], the errors were reduced and oscillations were suppressed by the present method with the higher-order gradient model in symmetrical form. The predicted results by the present method are in good agreement with the experimental data.

To analyze the mechanism of the structural deformation and cavitation due to

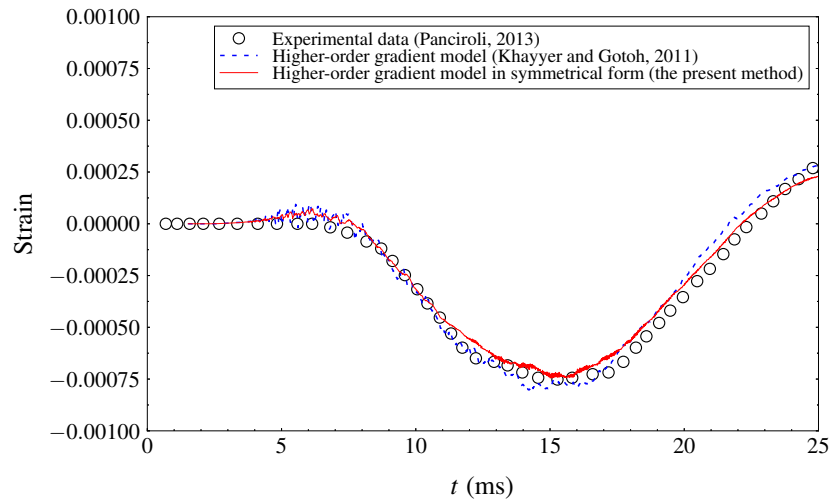


Figure 6.12: Comparison of local strains ($\alpha = 20^\circ$ and $H = 0.5$ m)

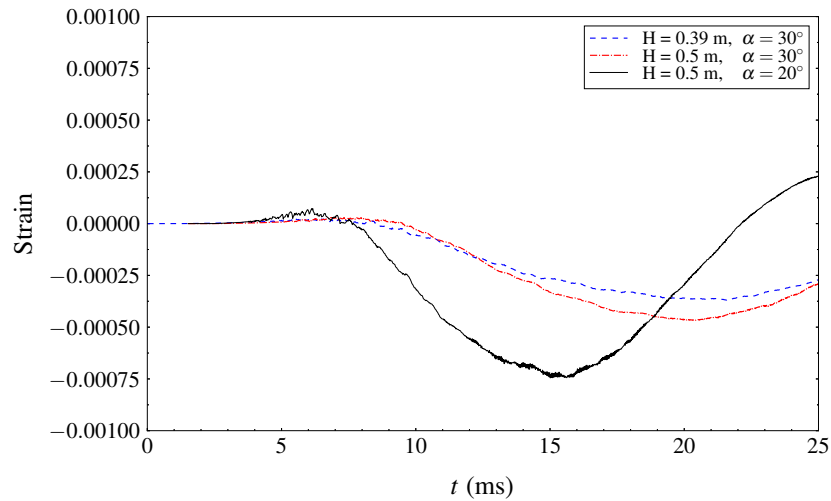


Figure 6.13: Numerical results of local strains for different deadrise angles and drop heights

slamming, numerical results for the two drop heights and the two deadrise angles are compared in Fig. 6.13. The pressure and strain contours are shown in Figs. 6.14 to

6.22. The high impact pressure occurs around the wedge tip when the object touches the water surface. Afterwards, the location of local high pressure moves along the jets over time. Large structural deformations occur near the position of the local high pressure, which further affect the fluid pressure field. The structural deformation led to a low pressure around the wedge tip. If the local pressure is lower than the vapor pressure of water, cavitation will occur. For a smaller deadrise angle, a larger structural deformation during the water entry can be seen in Fig. 6.21.

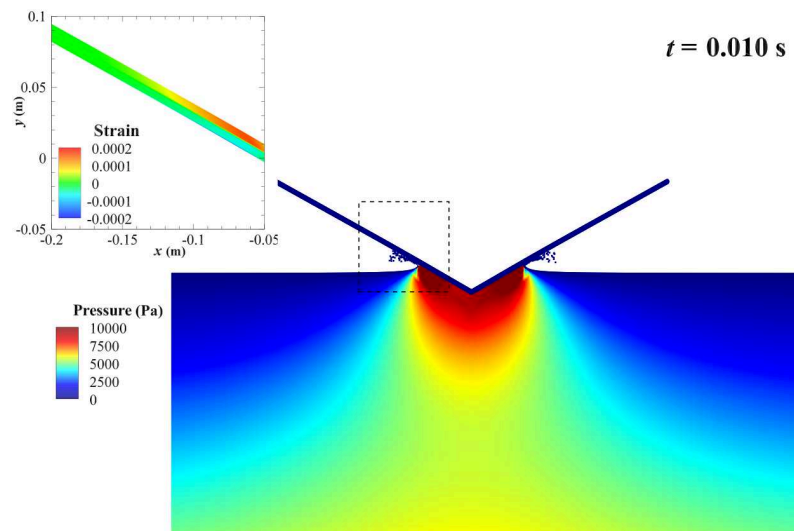


Figure 6.14: Contours of fluid pressure and strain of the elastic panel at $t = 0.1$ s ($\alpha = 30^\circ$ and $H = 0.39$ m)

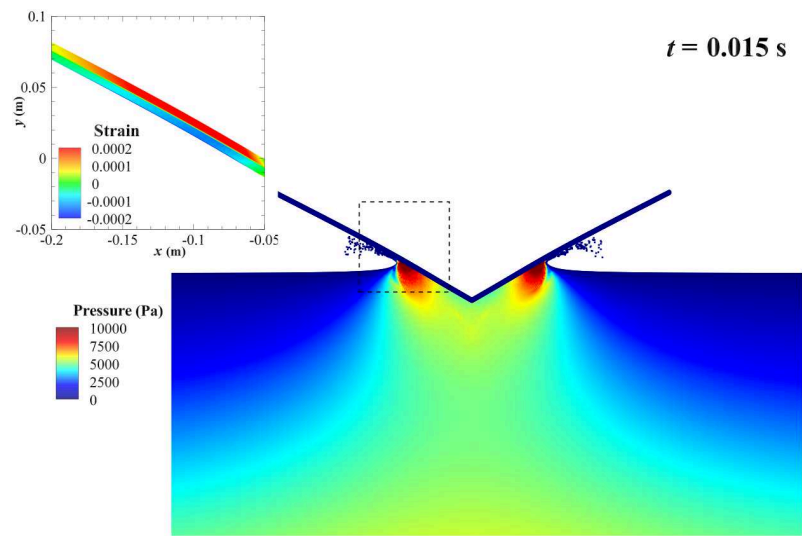


Figure 6.15: Contours of fluid pressure and strain of the elastic panel at $t = 0.15 \text{ s}$ ($\alpha = 30^\circ$ and $H = 0.39 \text{ m}$)

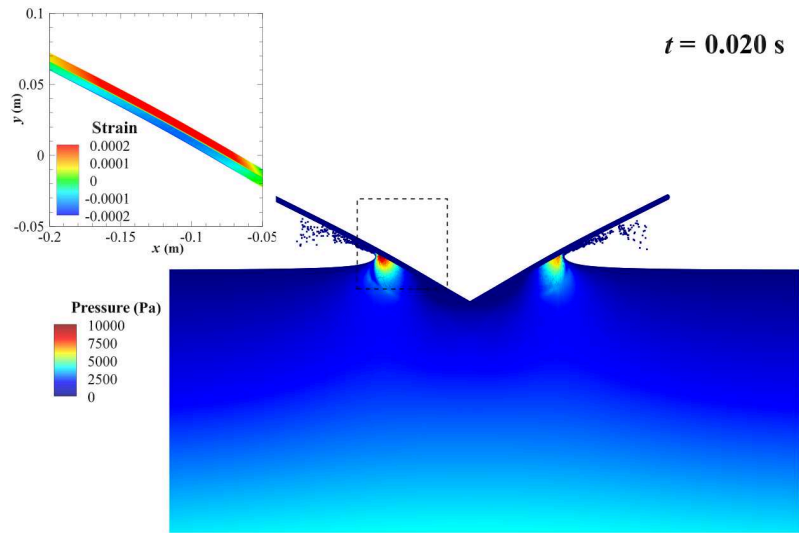


Figure 6.16: Contours of fluid pressure and strain of the elastic panel at $t = 0.2$ s ($\alpha = 30^\circ$ and $H = 0.39$ m)

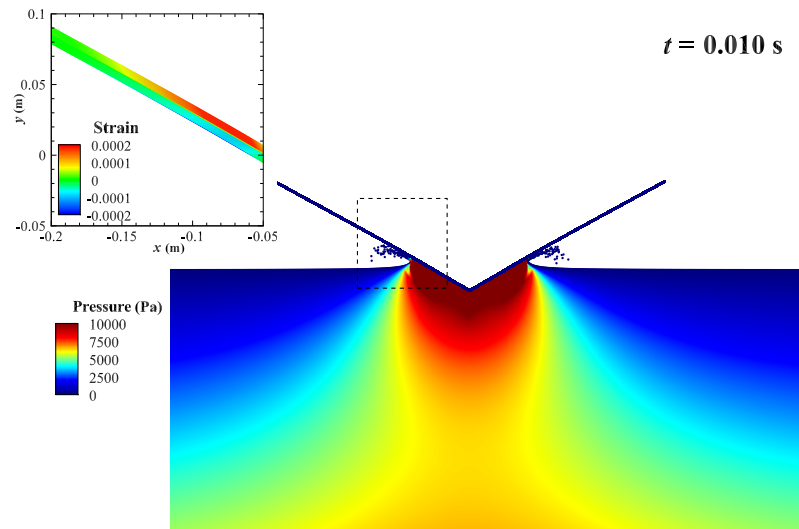


Figure 6.17: Contours of fluid pressure and strain of the elastic panel at $t = 0.1$ s ($\alpha = 30^\circ$ and $H = 0.5$ m)

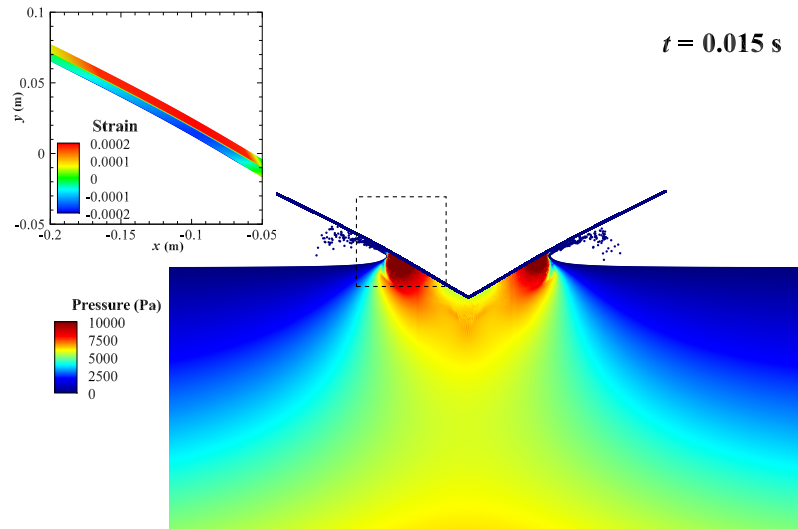


Figure 6.18: Contours of fluid pressure and strain of the elastic panel at $t = 0.15 \text{ s}$ ($\alpha = 30^\circ$ and $H = 0.5 \text{ m}$)

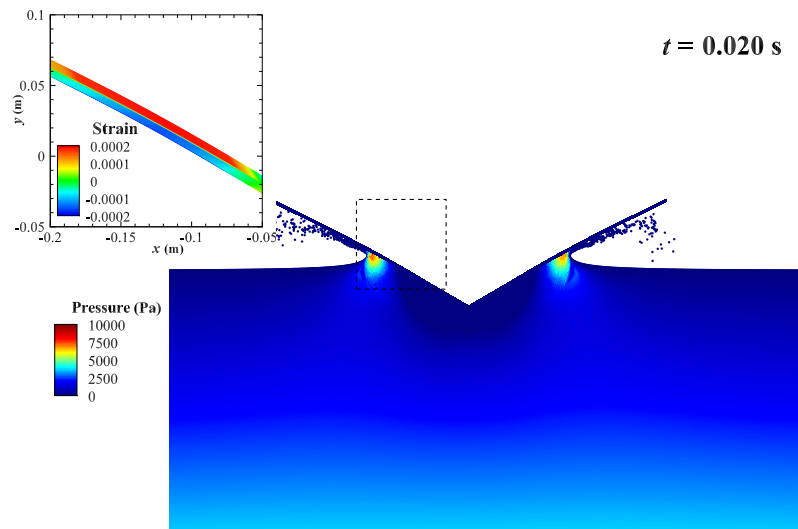


Figure 6.19: Contours of fluid pressure and strain of the elastic panel at $t = 0.2 \text{ s}$ ($\alpha = 30^\circ$ and $H = 0.5 \text{ m}$)

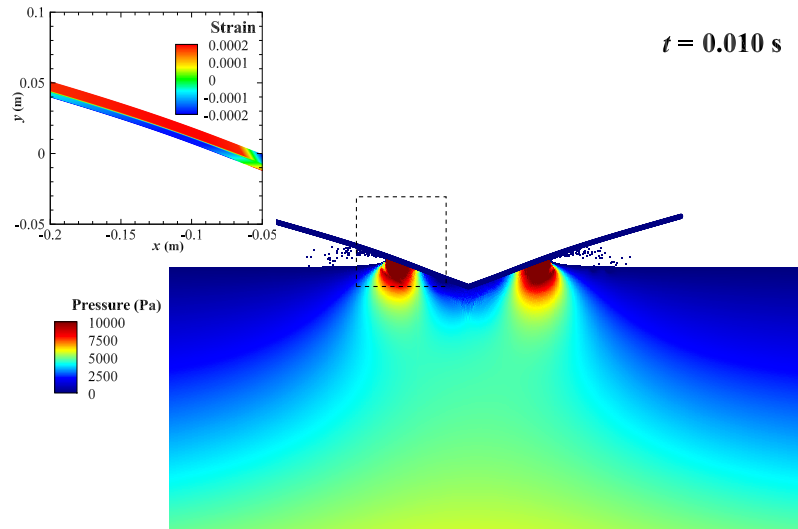


Figure 6.20: Contours of fluid pressure and strain of the elastic panel at $t = 0.1 \text{ s}$ ($\alpha = 20^\circ$ and $H = 0.5 \text{ m}$)

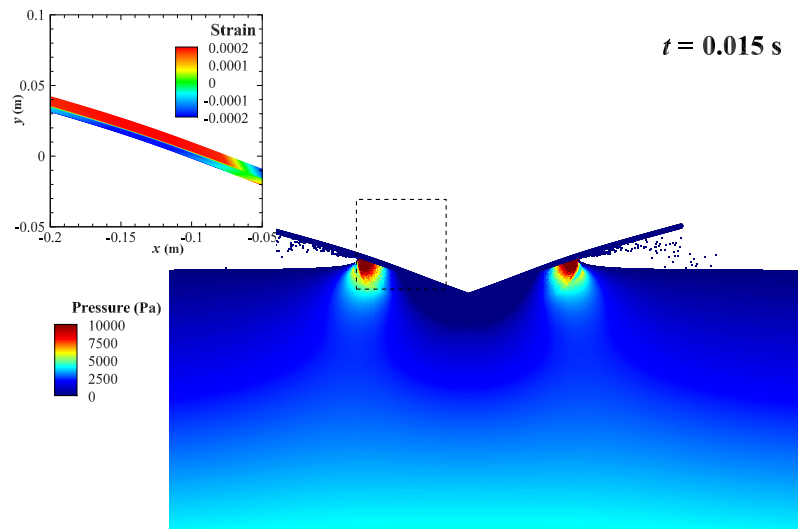


Figure 6.21: Contours of fluid pressure and strain of the elastic panel at $t = 0.15 \text{ s}$ ($\alpha = 20^\circ$ and $H = 0.5 \text{ m}$)

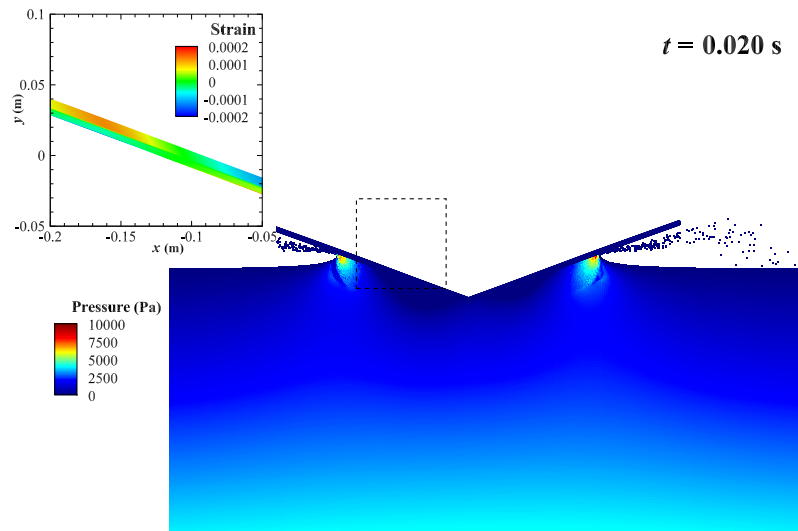


Figure 6.22: Contours of fluid pressure and strain of the elastic panel at $t = 0.2$ s ($\alpha = 20^\circ$ and $H = 0.5$ m)

Chapter 7

Conclusions and Future Work

7.1 Conclusions

This thesis presents an improved higher-order MPS method to solve 2-D water entry problems with fluid-structure interaction. The model of pressure gradient was modified to guarantee the first-order consistency and the conservation of momentum simultaneously. A particle shifting technique has been employed for further improvement. A particle convergence index (PCI) method was developed to evaluate the uncertainties in solutions by Lagrangian particle-based methods. Different particle spacings were applied for the hydrodynamic and structural analysis.

The present MPS method was first validated by solving 2-D dam breaking and 2-D vibration of a thin plate. Verification and validation studies were also carried out for rigid wedges and ship sections as well as elastic wedges entering the calm water. Convergence studies on particle spacing, time step and the number of particle layers across the thickness of the plate indicate that the numerical results converged

well. The PCI's of the predicted strain of the elastic wedge were less than 10%. Good agreement was achieved between the numerical predictions and the experimental data.

Based on the convergence studies, the following best-practice parameters are recommended for 2-D simulations of hydroelastic slamming with the present higher-order method. To keep numerical stability, the CFL number should be less than 0.14 for the fluid and 0.18×10^{-3} for the structure. For the uniform distribution of particles in the computational domain, the number of particles per meter should be at least 1,000 for the fluid and 4,000 for the structure. In the present studies, the number of particles over the wedge panel was 300 and the number of particles across the thickness of the plate was 8.

For the same deadrise angle of the wedge, the drop height has limited influence on the frequency of vibration, in spite of the magnitude was increased for a large drop height. For the same drop height, a greater hydroelastic effect was observed for the small deadrise angle of the wedge. A larger structural deformation and a higher frequency of vibration of the elastic panel occurred during the slamming due to greater impact velocity and smaller deadrise angle. The local low pressure due to structural deformation was analyzed, which could result in cavitation. Consequently, it is important to study the hydroelastic deformation of the wedge with a small deadrise angle and high impact velocity during the water entry. More validation studies will be carried out in the future on cavitation.

The limitations of the presented method are also discussed. Firstly, the computing efficiency is limited by the large memories consumed for the parallel computation. Another limitation is the present method did not consider the air phase in the fluid-structure interaction. Air bubbles / cushions could have certain effects on the

slamming loads for the cases with complex geometries and deformable structures.

7.2 Recommendations for Future Work

The present 2-D method can be extended for 3-D simulations. The interaction region of particles will be changed from a circle to a sphere. Note that a smaller CFL number should be applied in 3-D simulations rather than that in 2-D cases since the particles could move through a wall boundary. The improved higher-order MPS method has advantages in solving wave impact problems due to its good capacity to deal with the highly deformed / breaking free surface in 3-D simulations. Due to the 3-D effects, the deformation of the fluid-structure interface could be very complicated, leading to bad qualities of 3-D grids in grid-based methods. Numerical errors caused by grid failures can be avoided in the Lagrangian particle methods. Therefore, the improved higher-order MPS method has great potential to solve the 3-D FSI problems with large deformations.

However, there are several potential challenges as follows that need to be addressed:

Free surface. It could be difficult to identify the free-surface particles with the present combined density and non-symmetry criteria in 3-D simulations. The identification of particles on free surfaces in 3-D simulations needs to be addressed.

Computing resources. 3-D simulations will require large computer memory. For example, the radius of the particle interaction region typically equals to 2.1 times the particle spacing. There are 12 neighbouring particles within the interaction region for 2-D simulations. For 3-D simulations, the number of neighbouring particles will

be at least 32. In addition, boundaries will require much more memory since more dummy particles are needed in 3-D simulations.

Computing efficiency. The computing efficiency in 3-D MPS methods remains a challenge. With the increase of the neighbouring particles in 3-D simulations, the bandwidth of the matrix in the linear equations for pressure is therefore increased. Searching neighbouring particles and solving the Poisson equations are much more time-consuming in 3-D simulations. In terms of the parallel computing, computing speed-up based on MPI/OpenMP schemes is limited. Recently, GPUs have been used to improve the computing efficiency in 3-D simulations.

Note that progress has been made to overcome these difficulties in 3-D simulations using improved MPS methods [101, 102, 103]. It is promising to extend the present 2-D method to 3-D in future work.

Bibliography

- [1] O. M. Faltinsen, “Hydroelastic slamming,” *Journal of Marine Science and Technology*, vol. 5, no. 2, pp. 49–65, 2000.
- [2] O. M. Faltinsen, M. Landrini, and M. Greco, “Slamming in marine applications,” *Journal of Engineering Mathematics*, vol. 48, no. 3, pp. 187–217, 2004.
- [3] S.-L. Chuang, “Experiments on flat-bottom slamming,” *Journal of Ship Research*, vol. 10, no. 01, pp. 10–17, 1966.
- [4] O. Belik, R. Bishop, and W. Price, “Influence of bottom and flare slamming on structural responses,” *Royal Institution of Naval Architects Transactions*, vol. 130, 1988.
- [5] A. Troesch and M. Wang, “An experimental study for slamming flow and green water on deck final report,” tech. rep., University of Michigan, 1994.
- [6] B. Shabani, J. Lavroff, D. S. Holloway, M. R. Davis, and G. A. Thomas, “Wet-deck slamming loads and pressures acting on wave piercing catamarans,” *International Shipbuilding Progress*, vol. 66, no. 3, pp. 201–231, 2019.

- [7] R. Zhao, O. Økland, J. Hoff, and J. Aarsnes, “Bowflare and stern slamming induced whipping of large ships,” in *Hydrodynamics VI: Theory and Applications: Proceedings of the 6th International Conference on Hydrodynamics, Perth, Western Australia, 24-26 November 2004*, p. 167, CRC Press, 2004.
- [8] W. Boef, “Launch and impact of free-fall lifeboats. Part I. Impact theory,” *Ocean Engineering*, vol. 19, no. 2, pp. 119–138, 1992.
- [9] J. Jose and S.-J. Choi, “Estimation of slamming coefficients on local members of offshore wind turbine foundation (jacket type) under plunging breaker,” *International Journal of Naval Architecture and Ocean Engineering*, vol. 9, no. 6, pp. 624–640, 2017.
- [10] K. Attfield, “Gas platforms-how designers underestimated North Sea,” *Offshore Technology*, 1975.
- [11] A. Bereznitski, “Slamming: the role of hydroelasticity,” *International Shipbuilding Progress*, vol. 48, no. 4, pp. 333–351, 2001.
- [12] J. Verhagen, “The impact of a flat plate on a water surface,” *Journal of Ship Research*, vol. 11, no. 04, pp. 211–223, 1967.
- [13] M.-C. Lin and L.-D. Shieh, “Simultaneous measurements of water impact on a two-dimensional body,” *Fluid Dynamics Research*, vol. 19, no. 3, p. 125, 1997.
- [14] S. Okada and Y. Sumi, “On the water impact and elastic response of a flat plate at small impact angles,” *Journal of Marine Science and Technology*, vol. 5, no. 1, pp. 31–39, 2000.

- [15] M. Battley, I. Stenius, J. Breder, and S. Edinger, “Dynamic characterisation of marine sandwich structures,” in *Sandwich Structures 7: Advancing with Sandwich Structures and Materials*, pp. 537–546, Springer, 2005.
- [16] F. Huera-Huarte, D. Jeon, and M. Gharib, “Experimental investigation of water slamming loads on panels,” *Ocean Engineering*, vol. 38, no. 11-12, pp. 1347–1355, 2011.
- [17] R. L. Bisplinghoff and C. S. Doherty, “Some studies of the impact of vee wedges on a water surface,” *Journal of the Franklin Institute*, vol. 253, no. 6, pp. 547–561, 1952.
- [18] M. Greenhow and W.-M. Lin, “Nonlinear-free surface effects: experiments and theory,” tech. rep., Massachusetts Institute of Technology, 1983.
- [19] A. Troesch and C. Kang, “Hydrodynamic impact loads on three-dimensional bodies,” in *Proceedings of 16th Symposium on Naval Hydrodynamics*, 1986.
- [20] T. Tveitnes, A. Fairlie-Clarke, and K. Varyani, “An experimental investigation into the constant velocity water entry of wedge-shaped sections,” *Ocean Engineering*, vol. 35, no. 14-15, pp. 1463–1478, 2008.
- [21] C. Judge, A. Troesch, and M. Perlin, “Initial water impact of a wedge at vertical and oblique angles,” *Journal of Engineering Mathematics*, vol. 48, no. 3, pp. 279–303, 2004.

- [22] M. Barjasteh, H. Zeraatgar, and M. J. Javaherian, “An experimental study on water entry of asymmetric wedges,” *Applied Ocean Research*, vol. 58, pp. 292–304, 2016.
- [23] R. Zhao, O. Faltinsen, and J. Aarsnes, “Water entry of arbitrary two-dimensional sections with and without flow separation,” in *Proceedings of the 21st Symposium on Naval Hydrodynamics*, pp. 408–423, Trondheim, Norway, National Academy Press, Washington, DC, USA, 1996.
- [24] O. A. Hermundstad and T. Moan, “Numerical and experimental analysis of bow flare slamming on a Ro–Ro vessel in regular oblique waves,” *Journal of Marine Science and Technology*, vol. 10, no. 3, pp. 105–122, 2005.
- [25] L. Yang, H. Yang, S. Yan, Q. Ma, and M. Bihnam, “Comparative study on water impact problem,” in *Proceedings of 26th International Ocean and Polar Engineering Conference*, International Society of Offshore and Polar Engineers, 2016.
- [26] S. Y. Hong, K. H. Kim, and S. C. Hwang, “Comparative study of water-impact problem for ship section and wedge drops,” *International Journal of Offshore and Polar Engineering*, vol. 27, no. 02, pp. 123–134, 2017.
- [27] K.-H. Kim, Y.-M. Choi, and S. Y. Hong, “Experimental investigations of the characteristics of pressure sensors for 2D wedge drop,” *International Journal of Offshore and Polar Engineering*, vol. 27, no. 02, pp. 144–151, 2017.
- [28] S. Y. Hong, K.-H. Kim, B. W. Kim, and Y.-S. Kim, “Experimental study on the bow-flare slamming of a 10,000 TEU containership,” in *Proceedings of 24th*

International Ocean and Polar Engineering Conference, International Society of Offshore and Polar Engineers, 2014.

- [29] K.-H. Kim, B. W. Kim, S. Y. Hong, and Y.-S. Kim, “Characteristics of stern slamming loads on an ultra-large containership in regular and irregular waves,” in *Proceedings of 25th International Ocean and Polar Engineering Conference*, International Society of Offshore and Polar Engineers, 2015.
- [30] R. Panciroli, S. Abrate, G. Minak, and A. Zucchelli, “Hydroelasticity in water-entry problems: Comparison between experimental and SPH results,” *Composite Structures*, vol. 94, no. 2, pp. 532–539, 2012.
- [31] R. Panciroli, “Water entry of flexible wedges: Some issues on the FSI phenomena,” *Applied Ocean Research*, vol. 39, pp. 72–74, 2013.
- [32] H. Luo, H. Wang, and C. G. Soares, “Numerical and experimental study of hydrodynamic impact and elastic response of one free-drop wedge with stiffened panels,” *Ocean Engineering*, vol. 40, pp. 1–14, 2012.
- [33] I. Stenius, A. Rosén, M. Battley, and T. Allen, “Experimental hydroelastic characterization of slamming loaded marine panels,” *Ocean Engineering*, vol. 74, pp. 1–15, 2013.
- [34] A. Shams, M. Jalalisendi, and M. Porfiri, “Experiments on the water entry of asymmetric wedges using particle image velocimetry,” *Physics of Fluids*, vol. 27, no. 2, p. 027103, 2015.

- [35] A. Shams, S. Zhao, and M. Porfiri, “Hydroelastic slamming of flexible wedges: Modeling and experiments from water entry to exit,” *Physics of Fluids*, vol. 29, no. 3, p. 037107, 2017.
- [36] S. Russo, M. Jalalisendi, G. Falcucci, and M. Porfiri, “Experimental characterization of oblique and asymmetric water entry,” *Experimental Thermal and Fluid Science*, vol. 92, pp. 141–161, 2018.
- [37] T. von Kármán, “The impact on seaplane floats during landing,” tech. rep., NACA, Washington, 1929.
- [38] H. Wagner, “Über stoß-und gleitvorgänge an der oberfläche von flüssigkeiten,” *ZAMM-Journal of Applied Mathematics and Mechanics/Zeitschrift für Angewandte Mathematik und Mechanik*, vol. 12, no. 4, pp. 193–215, 1932.
- [39] Z. Dobrovolskaya, “On some problems of similarity flow of fluid with a free surface,” *Journal of Fluid Mechanics*, vol. 36, no. 4, pp. 805–829, 1969.
- [40] J. Oliver, “Second-order wagner theory for two-dimensional water-entry problems at small deadrise angles,” *Journal of Fluid Mechanics*, vol. 572, p. 59, 2007.
- [41] S. Howison, J. Ockendon, and S. Wilson, “Incompressible water-entry problems at small deadrise angles,” *Journal of Fluid Mechanics*, vol. 222, pp. 215–230, 1991.
- [42] X. Mei, Y. Liu, and D. K. Yue, “On the water impact of general two-dimensional sections,” *Applied Ocean Research*, vol. 21, no. 1, pp. 1–15, 1999.

- [43] Y. M. Scolan and A. A. Korobkin, “Three-dimensional theory of water impact. Part 1. Inverse Wagner problem,” *Journal of Fluid Mechanics*, vol. 440, pp. 293–326, 2001.
- [44] R. Zhao and O. Faltinsen, “Water entry of two-dimensional bodies,” *Journal of Fluid Mechanics*, vol. 246, pp. 593–612, 1993.
- [45] J. Wang and O. M. Faltinsen, “Improved numerical solution of Dobrovol’skaya’s boundary integral equations on similarity flow for uniform symmetrical entry of wedges,” *Applied Ocean Research*, vol. 66, pp. 23–31, 2017.
- [46] J. M. Chuang, W. Zhu, and W. Qiu, “Numerical solutions of 2-D water entry problem,” in *Proceedings of 16th International Offshore and Polar Engineering Conference*, International Society of Offshore and Polar Engineers, 2006.
- [47] A. Tassin, N. Jacques, A. E. M. Alaoui, A. Nême, and B. Leblé, “Hydrodynamic loads during water impact of three-dimensional solids: modelling and experiments,” *Journal of Fluids and Structures*, vol. 28, pp. 211–231, 2012.
- [48] M. Sussman, P. Smereka, and S. Osher, “A level set approach for computing solutions to incompressible two-phase flow,” *Journal of Computational Physics*, vol. 114, no. 1, pp. 146–159, 1994.
- [49] C. W. Hirt and B. D. Nichols, “Volume of fluid (VOF) method for the dynamics of free boundaries,” *Journal of Computational Physics*, vol. 39, no. 1, pp. 201–225, 1981.

- [50] H. Takewaki, A. Nishiguchi, and T. Yabe, “Cubic interpolated pseudo-particle method (CIP) for solving hyperbolic-type equations,” *Journal of Computational Physics*, vol. 61, no. 2, pp. 261–268, 1985.
- [51] K. Kleefsman, G. Fekken, A. Veldman, B. Iwanowski, and B. Buchner, “A volume-of-fluid based simulation method for wave impact problems,” *Journal of Computational Physics*, vol. 206, no. 1, pp. 363–393, 2005.
- [52] T. E. Schellin and O. El Moctar, “Numerical prediction of impact-related wave loads on ships,” *Journal of Offshore Mechanics and Arctic Engineering*, vol. 129, no. 1, pp. 39–47, 2007.
- [53] Q. Yang and W. Qiu, “Numerical simulation of water impact for 2D and 3D bodies,” *Ocean Engineering*, vol. 43, pp. 82–89, 2012.
- [54] P. Wen and W. Qiu, “Solving 2-D water entry problems with a CIP method and a parallel computing algorithm,” *Marine Systems & Ocean Technology*, vol. 11, no. 1-2, pp. 1–9, 2016.
- [55] P. Wen and W. Qiu, “Improved prediction of 3-D water entry with a CIP method and parallel computing,” *Ocean Engineering*, vol. 164, pp. 426–442, 2018.
- [56] P. M. Carrica, F. Ismail, M. Hyman, S. Bhushan, and F. Stern, “Turn and zigzag maneuvers of a surface combatant using a URANS approach with dynamic overset grids,” *Journal of Marine Science and Technology*, vol. 18, no. 2, pp. 166–181, 2013.

- [57] Z. Shen, Y.-F. Hsieh, Z. Ge, R. Korpus, and J. Huan, “Slamming load prediction using overset CFD methods,” in *Offshore Technology Conference*, Offshore Technology Conference, 2016.
- [58] D. J. Piro and K. J. Maki, “Hydroelastic analysis of bodies that enter and exit water,” *Journal of Fluids and Structures*, vol. 37, pp. 134–150, 2013.
- [59] J. J. Monaghan, “An introduction to SPH,” *Computer Physics Communications*, vol. 48, no. 1, pp. 89–96, 1988.
- [60] S. Koshizuka and Y. Oka, “Moving-particle semi-implicit method for fragmentation of incompressible fluid,” *Nuclear Science and Engineering*, vol. 123, no. 3, pp. 421–434, 1996.
- [61] M. Farsi and P. Ghadimi, “Simulation of 2D symmetry and asymmetry wedge water entry by smoothed particle hydrodynamics method,” *Journal of the Brazilian Society of Mechanical Sciences and Engineering*, vol. 37, no. 3, pp. 821–835, 2015.
- [62] E.-S. Lee, C. Moulinec, R. Xu, D. Violeau, D. Laurence, and P. Stansby, “Comparisons of weakly compressible and truly incompressible algorithms for the SPH mesh free particle method,” *Journal of Computational Physics*, vol. 227, no. 18, pp. 8417–8436, 2008.
- [63] M. Yokoyama, Y. Kubota, K. Kikuchi, G. Yagawa, and O. Mochizuki, “Some remarks on surface conditions of solid body plunging into water with particle method,” *Advanced Modeling and Simulation in Engineering Sciences*, vol. 1, no. 1, p. 9, 2014.

- [64] S. Lind, P. Stansby, B. Rogers, and P. Lloyd, “Numerical predictions of water–air wave slam using incompressible–compressible smoothed particle hydrodynamics,” *Applied Ocean Research*, vol. 49, pp. 57–71, 2015.
- [65] Z. Sun, K. Djidjeli, J. T. Xing, and F. Cheng, “Coupled MPS-modal superposition method for 2D nonlinear fluid-structure interaction problems with free surface,” *Journal of Fluids and Structures*, vol. 61, pp. 295–323, 2016.
- [66] P. Nair and G. Tomar, “A study of energy transfer during water entry of solids using incompressible SPH simulations,” *Sādhanā*, vol. 42, no. 4, pp. 517–531, 2017.
- [67] C.-p. Rao and D.-c. Wan, “Numerical study of the wave-induced slamming force on the elastic plate based on MPS-FEM coupled method,” *Journal of Hydrodynamics*, vol. 30, no. 1, pp. 70–78, 2018.
- [68] H. Akimoto, “Numerical simulation of the flow around a planing body by MPS method,” *Ocean Engineering*, vol. 64, pp. 72–79, 2013.
- [69] Y. Zhang, Z. Tang, and D. Wan, “Simulation of water entry of a free-falling wedge by improved MPS method,” in *Proceedings of 26th International Ocean and Polar Engineering Conference*, International Society of Offshore and Polar Engineers, 2016.
- [70] A. Kundu, A. K. Soti, H. Garg, R. Bhardwaj, and M. C. Thompson, “Computational modeling and analysis of flow-induced vibration of an elastic splitter plate using a sharp-interface immersed boundary method,” *SN Applied Sciences*, vol. 2, pp. 1–23, 2020.

- [71] S. A. Manjunathan and R. Bhardwaj, “Thrust generation by pitching and heaving of an elastic plate at low Reynolds number,” *Physics of Fluids*, vol. 32, no. 7, p. 073601, 2020.
- [72] J.-P. Minier, S. Chibbaro, and S. B. Pope, “Guidelines for the formulation of Lagrangian stochastic models for particle simulations of single-phase and dispersed two-phase turbulent flows,” *Physics of Fluids*, vol. 26, no. 11, p. 113303, 2014.
- [73] M. F. Barone and J. L. Payne, “Methods for simulation-based analysis of fluid-structure interaction,” tech. rep., Sandia National Laboratories, 2005.
- [74] R. Toukhtarian, S. G. Hatzikiriakos, H. Atsbha, and B. Boulet, “Modeling polymer extrusion with varying die gap using Arbitrary Lagrangian Eulerian (ALE) method,” *Physics of Fluids*, vol. 30, no. 9, p. 093103, 2018.
- [75] M. H. Saadat and I. V. Karlin, “Arbitrary Lagrangian–Eulerian formulation of lattice Boltzmann model for compressible flows on unstructured moving meshes,” *Physics of Fluids*, vol. 32, no. 4, p. 046105, 2020.
- [76] M. Song, S. Koshizuka, and Y. Oka, “Dynamic analysis of elastic solids by MPS method,” *Nippon Kikai Gakkai Ronbunshu A Hen (Transactions of the Japan Society of Mechanical Engineers Part A) (Japan)*, vol. 17, no. 1, pp. 16–22, 2005.
- [77] A. Khayyer and H. Gotoh, “Enhancement of stability and accuracy of the moving particle semi-implicit method,” *Journal of Computational Physics*, vol. 230, no. 8, pp. 3093–3118, 2011.

- [78] H. Gotoh and A. Khayyer, “Current achievements and future perspectives for projection-based particle methods with applications in ocean engineering,” *Journal of Ocean Engineering and Marine Energy*, vol. 2, no. 3, pp. 251–278, 2016.
- [79] R. Zha, H. Peng, and W. Qiu, “Solving 2-D slamming problems by the higher-order MPS method with an improved pressure gradient model,” in *Proceedings of 38th International Conference on Ocean, Offshore and Arctic Engineering*, p. V009T12A00, Glasgow, UK, June, 2019.
- [80] R. Zha, H. Peng, and W. Qiu, “Solving 2-D slamming problems by an improved higher-order moving particle semi-implicit method,” *Journal of Ship Research*, pp. 1–29, 2020.
- [81] R. Zha, H. Peng, and W. Qiu, “An improved higher-order moving particle semi-implicit method for simulations of two-dimensional hydroelastic slamming,” *Physics of Fluids*, vol. 33, no. 3, p. 037104, 2021.
- [82] R. Zha, W. Qiu, and H. Peng, “Solving 2D fluid-structure interaction problem by a coupled particle method,” in *Proceedings of 36th International Conference on Ocean, Offshore and Arctic Engineering*, p. V07AT06A046, Trondheim, Norway, June, 2017.
- [83] Y. Zhang, X. Wang, Z. Tang, and D. Wan, “Numerical simulation of green water incidents based on parallel MPS method,” in *Proceedings of 23rd International Offshore and Polar Engineering Conference*, International Society of Offshore and Polar Engineers, 2013.

- [84] S. Lind, R. Xu, P. Stansby, and B. D. Rogers, “Incompressible smoothed particle hydrodynamics for free-surface flows: A generalised diffusion-based algorithm for stability and validations for impulsive flows and propagating waves,” *Journal of Computational Physics*, vol. 231, no. 4, pp. 1499–1523, 2012.
- [85] I. B. Celik, U. Ghia, P. J. Roache, and Christopher, “Procedure for estimation and reporting of uncertainty due to discretization in CFD applications,” *Journal of Fluids Engineering - Transactions of the ASME*, vol. 130, July 2008.
- [86] Z. Sun, G. Xi, and X. Chen, “Mechanism study of deformation and mass transfer for binary droplet collisions with particle method,” *Physics of Fluids*, vol. 21, no. 3, p. 032106, 2009.
- [87] F. Macia Lang, A. Souto Iglesias, M. Antuono, and A. Colagrossi, “Benefits of using a Wendland kernel for free-surface flows,” in *6th ERCOFTAC SPHERIC workshop on SPH applications*, p. 3037, Hamburg University of Technology, 2011.
- [88] H. Wendland, “Piecewise polynomial, positive definite and compactly supported radial functions of minimal degree,” *Advances in Computational Mathematics*, vol. 4, no. 1, pp. 389–396, 1995.
- [89] B. H. Lee, J. C. Park, M. H. Kim, and S. C. Hwang, “Step-by-step improvement of MPS method in simulating violent free-surface motions and impact loads,” *Computer Methods in Applied Mechanics and Engineering*, vol. 200, no. 9, pp. 1113–1125, 2011.

- [90] X. Zheng, Q. Ma, S. Shao, and A. Khayyer, “Modelling of violent water wave propagation and impact by incompressible SPH with first-order consistent kernel interpolation scheme,” *Water*, vol. 9, no. 6, p. 400, 2017.
- [91] G. Oger, M. Doring, B. Alessandrini, and P. Ferrant, “An improved SPH method: Towards higher order convergence,” *Journal of Computational Physics*, vol. 225, no. 2, pp. 1472–1492, 2007.
- [92] A. Khayyer and H. Gotoh, “A higher order Laplacian model for enhancement and stabilization of pressure calculation by the MPS method,” *Applied Ocean Research*, vol. 32, no. 1, pp. 124–131, 2010.
- [93] X. Cui and W. Qiu, “Solving 2-D highly nonlinear free-surface problems with an improved smoothed particle hydrodynamics method,” *Marine Systems & Ocean Technology*, vol. 13, no. 2-4, pp. 74–86, 2018.
- [94] A. Khayyer, H. Gotoh, and Y. Shimizu, “Comparative study on accuracy and conservation properties of two particle regularization schemes and proposal of an optimized particle shifting scheme in ISPH context,” *Journal of Computational Physics*, vol. 332, pp. 236–256, 2017.
- [95] M. Kondo, M. Tanaka, T. Harada, and S. Koshizuka, “Elastic objects for computer graphic field using MPS method,” in *ACM SIGGRAPH 2007 posters*, p. 53, ACM, 2007.
- [96] S. C. Hwang, A. Khayyer, H. Gotoh, and J. C. Park, “Development of a fully Lagrangian MPS-based coupled method for simulation of fluid-structure interaction problems,” *Journal of Fluids and Structures*, vol. 50, pp. 497–511, 2014.

- [97] A. Khayyer, H. Gotoh, and S. Shao, “Enhanced predictions of wave impact pressure by improved incompressible SPH methods,” *Applied Ocean Research*, vol. 31, no. 2, pp. 111–131, 2009.
- [98] L. Lobovsky, E. Botia-Vera, F. Castellana, J. Mas-Soler, and A. Souto-Iglesias, “Experimental investigation of dynamic pressure loads during dam break,” *Journal of Fluids and Structures*, vol. 48, pp. 407–434, 2014.
- [99] J. P. Gray, J. J. Monaghan, and R. Swift, “SPH elastic dynamics,” *Computer Methods in Applied Mechanics and Engineering*, vol. 190, no. 49-50, pp. 6641–6662, 2001.
- [100] H. Sabahi and A. Nikseresht, “Comparison of ISPH and WCSPH methods to solve fluid-structure interaction problems,” *Scientia Iranica*, vol. 23, no. 6, pp. 2595–2605, 2016.
- [101] K. Shibata, S. Koshizuka, and K. Tanizawa, “Three-dimensional numerical analysis of shipping water onto a moving ship using a particle method,” *Journal of Marine Science and Technology*, vol. 14, no. 2, pp. 214–227, 2009.
- [102] Y. Zhang and D. Wan, “MPS-FEM coupled method for fluid–structure interaction in 3D dam-break flows,” *International Journal of Computational Methods*, vol. 16, no. 02, p. 1846009, 2019.
- [103] A. Khayyer, H. Gotoh, Y. Shimizu, Y. Nishijima, and A. Nakano, “3D MPS-MPS coupled FSI solver for simulation of hydroelastic fluid-structure interactions in coastal engineering,” *Journal of Japan Society of Civil Engineers, Ser. B2 (Coastal Engineering)*, vol. 76, no. 2, pp. I37–I42, 2020.